

Measurement of the positron polarization at
an helical undulator based positron source for
the International Linear Collider ILC.

The E-166 experiment at SLAC

DISSERTATION

zur Erlangung des akademischen Grades
doctor rerum naturalium
(Dr. rer. nat.)
im Fach Physik

eingereicht an der
Mathematisch-Naturwissenschaftlichen
Fakultät I
Humboldt-Universität zu Berlin

von

Herr Dipl.-Phys. Laihem Karim
geboren am 17.03.1972 in Algier

Präsident der Humboldt-Universität zu Berlin:
Prof. Dr. Jürgen Mlynek

Dekan der Mathematisch-Naturwissenschaftlichen
Fakultät I:
Prof. Dr. Thomas Buckhout

Gutachter:

1. Prof. Dr. Hermann Kolanoski
2. Prof. Dr. Achim Stahl
3. Prof. Dr. Thomas Lohse

eingereicht am: 8. Januar 2008
Tag der mündlichen Prüfung: 5. Juni 2008

Abstract

A helical undulator based polarized positron source is foreseen at a future International Linear Collider (ILC). The E-166 experiment has tested this scheme using a one meter long, short-period, pulsed helical undulator installed in the Final Focus Test Beam (FFTB) at SLAC. A low-emittance 46.6 GeV electron beam passing through this undulator generated circularly polarized photons with energies up to about 8 MeV. The generated photons of several MeV with circular polarization are then converted in a relatively thin target to generate longitudinally polarized positrons. Measurements of the positron polarization have been performed at 5 different energies of the positrons. In addition electron polarization has been determined for one energy point. For a comparison of the measured asymmetries with the expectations detailed simulations were necessary. This required upgrading GEANT4 to include the dominant polarization dependent interactions of electrons, positrons and photons in matter. The measured polarization of the positrons agrees with the expectations and is for the energy point with the highest polarization at 6 MeV about 80%.

Keywords:

Polarized positron, Helical undulator, Linear Collider, Geant4

Zusammenfassung

Als Basis der Positronenquelle zur Erzeugung polarisierter Positronen bei einem zukünftigen internationalen Linearkollider ist ein helikaler Undulator vorgesehen. Das E-166 Experiment testete diese Methode unter Benutzung eines ein Meter langen, kurzperiodischen, gepulsten helikalen Undulators im Final Focus Test Beam (FFTB) am SLAC. Ein 46.6 GeV Elektronenstrahl mit geringer Emittanz wurde durch diesen Undulator geführt und erzeugte zirkular polarisierte Photonen mit einer Energie bis zu ungefähr 8 MeV. Diese wiederum konvertierten in einem relativ dünnen Target zu longitudinal polarisierten Positronen. Die Polarisation der Positronen wurde bei 5 verschiedenen Positronenergien gemessen. Zusätzlich ist die Polarisation von Elektronen für einen Energiepunkt gemessen worden. Um die gemessenen Asymmetrien mit den Erwartungen vergleichen zu können, waren detaillierte Simulationen nötig. Dies erforderte die Erweiterung von von GEANT4 um die wichtigsten polarisationsabhängigen Wechselwirkungen von Elektronen, Positronen und Photonen mit Materie. Die gemessene Positronpolarisation stimmt mit den Erwartungen überein und beträgt für den Energiepunkt mit der höchsten Polarisation von 6 MeV mehr als 80%.

Schlagwörter:

Polarisierter Positronen, Helikaler Undulator, Linearkollider, Geant4

Contents

1	Polarized Electrons and Positrons at the International Linear Collider	1
1.1	Introduction	1
1.2	Polarized Electron and Positron Beams at the ILC	2
1.2.1	Polarized electron source	3
1.2.2	Polarized positron source	4
1.3	Polarization Preservation	8
1.4	Polarimetry at the ILC	10
1.4.1	Laser Compton polarimeter	10
1.5	Physics Benefits from Positron Polarization at the ILC	11
1.5.1	Longitudinal beam polarization	11
1.5.2	Effective polarization	12
1.5.3	Left-right asymmetry	13
1.5.4	Standard Model Higgs physics	14
1.5.5	Suppression of W pairs	15
1.5.6	Supersymmetry	16
1.5.7	Summary of the physics case	17
2	The E-166 Experiment	21
2.1	Introduction	21
2.2	Principle of the E-166 Experiment.	21
2.2.1	Production of Circularly Polarized gamma Rays	23
2.2.2	Production of polarized positrons	25
2.2.3	Polarimetry in the E-166 experiment	27
2.3	Positron Diagnostic	30
2.3.1	The positron transport system	30
2.3.2	PosSi counter	35
2.4	The CsI(Tl) calorimeter	36
2.4.1	CsI(Tl) energy calibration at SLAC	39
2.5	Photon Diagnostics	42
2.5.1	Ag1SiC, Ag2SiC flux counters	42

2.5.2	GCAL : silicon-tungsten calorimeter	43
2.5.3	Aero-gel flux counter	43
2.6	Background Detectors	44
2.7	Tuning, operations and performance of the experiment	45
3	Implementation of polarization in Geant4	53
3.1	Polarization	54
3.2	Parameterization of Polarization	55
3.2.1	The Jones vector	55
3.2.2	Stokes parameters from Jones Vector	56
3.2.3	Transfer matrix	57
3.3	Polarization in GEANT4.	58
3.3.1	GEANT4	58
3.3.2	Polarized processes in GEANT4	60
3.4	Gamma Conversion and Bremsstrahlung	62
3.5	Polarized Bremsstrahlung for Electron and Positron	63
3.5.1	Polarization transfer from the lepton e^- (e^+) to a photon	63
3.5.2	Lepton depolarization	65
3.5.3	Simulation	66
3.6	Polarized Gamma Conversion	67
3.6.1	Polarization transfer from the photon to the two leptons	67
3.6.2	Simulation	68
3.7	Polarized Photoelectric Effect	68
3.7.1	Polarization transfer	69
3.8	Ionization	71
3.8.1	Method	71
3.8.2	Cross section	71
3.8.3	Simulation	73
3.9	Positron - Electron Annihilation	74
3.9.1	Method	74
3.9.2	Simulation	76
3.10	Compton scattering	77
3.10.1	Method	77
3.10.2	Total cross section	77
3.10.3	Differential Compton cross section	78
3.10.4	Simulation	78
4	Simulation of the positron generation and polarimetry	81
4.1	Introduction	81
4.2	The Helical Undulator Radiation	82
4.3	Polarized Positron (Electron) Production	84

4.3.1	Positron and Electron Yield	85
4.3.2	Positron and Electron Polarization	88
4.4	The $e^+(e^-)$ Transport System	90
4.4.1	Overview of the setup	90
4.4.2	Solenoid Magnetic Field	91
4.4.3	Spectrometer Magnetic Field	93
4.5	Simulation Of The e^+e^- Transport	100
4.5.1	Setting Points and Transmission through the Spectrom- eter	100
4.5.2	Momentum-Current relation of the spectrometer	101
4.5.3	Positron spatial distribution	102
4.6	The Positron Polarimeter	106
4.6.1	Setup of the E166 positron Polarimeter	106
4.6.2	The analyzing power	106
4.6.3	The expected asymmetries	118
5	Analysis, Results and Discussion.	121
5.1	Data structures	121
5.2	Analysis Procedure	123
5.2.1	Analysis strategy	123
5.2.2	Data selection	124
5.2.3	Background subtraction	126
5.2.4	Asymmetries	133
5.3	Systematic Uncertainties	133
5.3.1	Flux asymmetries and corrections	133
5.3.2	Extrinsic Background	134
5.3.3	Intrinsic Background	136
5.3.4	Knowledge of the iron polarization	137
5.4	Results	137
5.4.1	Asymmetries	137
5.4.2	Positron and electron polarization	137
5.5	The Photon Asymmetry and Polarization	140
	Bibliography	147
	List of Figures	153
	List of Tables	157

Introduction

Experimental particle physics investigates the properties and interactions of elementary particles by studying the reactions initiated in the collision of particles at high energies. Accelerators are necessary to accelerate the particles to these high energies. Particle detectors record the final state of the reactions in detail. The initial state is given by the accelerator, by the type of particle accelerated and the energy to which they are accelerated. In many situations the effectiveness of the experiment can be largely increased if particle beams are spin-polarized. This is the goal of the project described in this thesis.

Polarizing a particle beam means to align the spins of the beam particle into a given direction. Experimentally only positrons and electrons can be polarized in circular accelerators through the Sokolov-Ternov effect [A. A.Sokolov(1964), I. M. Ternov(1982)]. In linear accelerators they must be produced already polarized at the particle source (gun). The topic of this thesis is an attempt to develop a polarized particle source for a positron beam based on a helical undulator. The idea has been described by V.E. Balakin and A.A. Mikhailichenko in [Balakin and Mikhailichenko(1979)].

Four years ago, physicists from 15 institutions formed a collaboration to test this idea in an experiment called E-166 at the Stanford Linear Accelerator Center (SLAC) in Stanford (U.S). The work described here is part of this collaborative effort. The experiment is carried out in view of the International Linear Collider (ILC), a future large-scale particle physics project for which a polarized positron source is forseen.

This thesis summarize the E-166 experiment with a highlight on our contribution to the setup (The CsI(Tl) calorimeter), to simulation studies and to the data analysis. In the first chapter, we describe the undulator based polarized positron source for the International Linear Collider and the physics benefit when both electron and positron beams are polarized. In the second chapter, the most relevant part of the experiment and operations are described. The third and fourth chapter, focus on the implementation of polarized electromagnetic processes in Geant4 and the simulation of the polarized positron generation and polarimetry. Finally, the fifth chapter describes the data analysis methods and the polarization measurements.

Chapter 1

Polarized Electrons and Positrons at the International Linear Collider

1.1 Introduction

The International Linear Collider is a proposed new electron-positron collider with a linear acceleration of the two beams in opposite directions. The ILC is a project complementary to the Large Hadron Collider (LHC) at CERN in many respects. Together they allow to explore the TeV energy region beyond the reach of today's accelerators. The LHC-ILC complementarity is seen mainly in testing the Standard Model and in discovering and determining the origin of new physics. Mutual benefits for the physics program at both machines can occur both at the level of a combined interpretation of Hadron Collider and Linear Collider data and at the level of combined analyses of the data, where results obtained at one machine can directly influence the way analyses are carried out at the other machine. At these energies, significant discoveries are anticipated that will lead to a new understanding of elementary particles and the physics that governs the micro-cosmos and the universe. The collisions of electrons and positrons at this high energy, will give us a deeper insight into the interactions of elementary particles. New particles can be produced, like the "Higgs" and "SUSY" particles. Due to its intrinsic precision the ILC will have the capability to complement the answers to important questions that discoveries at the LHC will raise, from the identity of dark matter to the existence of extra dimensions.

In the ILC design [collaboration(2006a)], two facing linear accelerators (Fig. 1.1), each 20 kilometers long, accelerate beams of electrons and positrons

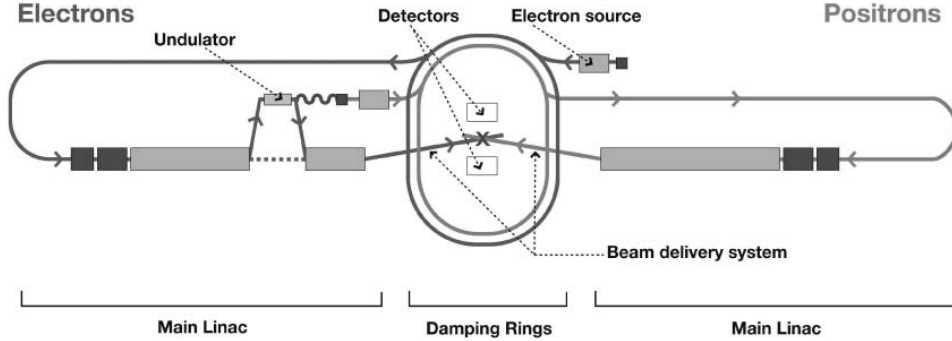


Figure 1.1: Schematic of the International Linear Collider (ILC) machine

toward each other. Each beam contains $2 \cdot 10^{10}$ electrons or positrons compressed to a tiny bunch with transverse dimensions of $655 \text{ nm} \times 5.7 \text{ nm}$. The ILC uses a new acceleration technology: superconducting RF cavities fabricated from niobium sheets. The ILC design goal is to reach a luminosity of $2 \cdot 10^{34} \text{ cm}^{-2}\text{s}^{-1}$ after 4 years of running. The most relevant beam parameters are summarized in Table 1.1 [collaboration(2006b)]. The ILC is a truly international efforts with hundreds of accelerator scientists and particle physicists in North America, Europe and Asia contributing.

The ILC is considered to be a 'precision machine' because of the well defined initial state. For the completeness of the quantum numbers of the initial states, the knowledge of the spin state of the beam may have a considerable impact on the physics where the interaction cross sections are spin dependant. Hence, this advantage is realized only if the initial state is uniquely defined in a quantum-mechanical including the particle initial spin state. While the beam momentum is well-defined in any electron/positron accelerator, a special effort is necessary to align the particle spins by polarizing the beams. Polarized electrons have been achieved before in a linear accelerator, the SLC [R. Alley(1995)]. The development of polarized positron source is the topic of this thesis.

1.2 Polarized Electron and Positron Beams at the ILC

The full physics potential of the ILC can only be realized with polarized e^- and e^+ beams [Moortgat-Pick and Steiner(2001)]. In the baseline design it is foreseen to polarize the electron beam to $P_{e^-} = 80\%$ to 90% .

Parameter at the IP	Units	ILC Nominal	ILC Upgrade
E_{cms}	GeV	500	1000
Rate f_r	Hz	5	5
N_{bunch}		2820	2820
Δ_{tb}	ns	307.7	307.7
N (e^- or e^+)		$2.00 \cdot 10^{10}$	$2.00 \cdot 10^{10}$
I_{ave}	A	0.0104	0.0104
Luminosity	$\text{cm}^{-2}\text{s}^{-1}$	$2.00 \cdot 10^{34}$	$2.00 \cdot 10^{34}$
$\gamma\epsilon_x$	m·rad	$1.00 \cdot 10^{-5}$	$1.00 \cdot 10^{-5}$
$\gamma\epsilon_y$	m·rad	$4.00 \cdot 10^{-8}$	$4.00 \cdot 10^{-8}$
β_x	m	$2.00 \cdot 10^{-2}$	$3.00 \cdot 10^{-2}$
β_y	m	$4.00 \cdot 10^{-4}$	$3.00 \cdot 10^{-4}$
σ_x	m	$6.55 \cdot 10^{-7}$	$5.54 \cdot 10^{-7}$
σ_y	m	$5.70 \cdot 10^{-9}$	$3.50 \cdot 10^{-9}$
σ_z	m	$3.00 \cdot 10^{-4}$	$3.00 \cdot 10^{-4}$

Table 1.1: ILC beam parameters at the IP for the 500 GeV nominal scheme and for the upgrade to 1 TeV [collaboration(2006a)].

For polarized positrons, in the current Baseline Configuration Document (BCD) [collaboration(2006a), G. Moortgat-Pick(2006)] a helical undulator based positron source has been chosen as the most reliable solution for producing the required positron flux and polarization. Circularly polarized radiation from the undulator is used to produce positrons via an electromagnetic shower in a thin target.

1.2.1 Polarized electron source

Polarized electron sources have been pioneered at SLAC, since the mid-1970s [R. Alley(1995)]. The SLC electron beam was polarized to around 80%. The sources are based on a strained semiconductor photocathode, which absorbs circularly polarized laser photons and emits electrons (photoelectric effect). This principle shown in Fig. 1.2 was developed and successfully used at the SLC. The SLC system can be adopted directly for the ILC using a laser system with the appropriate time structure. Improved versions of the SLC Polarized Electron Source (PES) can meet the expected requirements of the international linear collider for polarization, charge and lifetime [collaboration(2006a)].

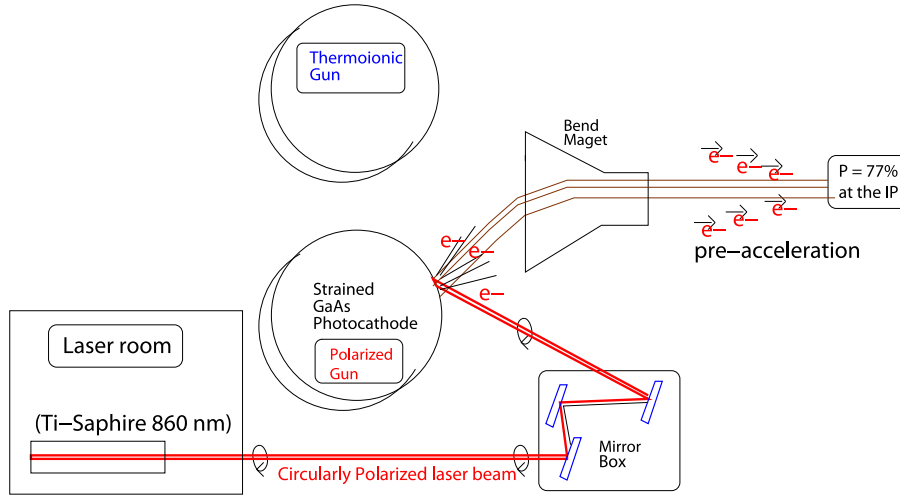


Figure 1.2: Schematic of the polarized electron source at the SLC.

1.2.2 Polarized positron source

Positrons (e^+) –the anti-particles of electrons– used in accelerators can be generated by different processes. As an example one of the processes is the β^+ -decay of specific radioisotopes like $^{22}\text{Na} \rightarrow ^{22}\text{Ne} + \beta^+ + \nu_e + \gamma$. In β^+ -decay positrons are generated with longitudinal polarization due to the parity violation of the interaction. But, in beta decay positrons have a large energy spread, a wide angular distribution, and low intensity. This method is unpractical for a positron beam for the ILC. The second relevant process is e^+e^- pair creation by high-energy photons, known also as photon driven, beam based positron sources. The second approach is based on circularly polarized photon beams which create e^+e^- pairs in a dens target.

To minimize the emittance of the produced positrons, thin targets (fraction of a radiation length) with high-Z, high-density materials, such as tungsten or titanium alloys are required.

All the schemes for obtaining longitudinally polarized positrons (except that using β^+ decay) discussed in this section are based on the reaction $\gamma + \gamma \rightarrow e^+ + e^-$, where at least one of two photons should be circularly polarized. When the gamma conversion occurs in a target, the role of the second photon in the reaction is played by an unpolarized Coulomb photon providing the momentum exchange between the created particles and a nucleus. The incident photon should be circularly polarized and should have an energy above the threshold value of $2m_e c^2$ (m_e is the electron rest mass and c the speed of light). The helicity transfer at high energy was described in [Olsen and Maximon(1959)] for two basic QED-processes: bremsstrahlung

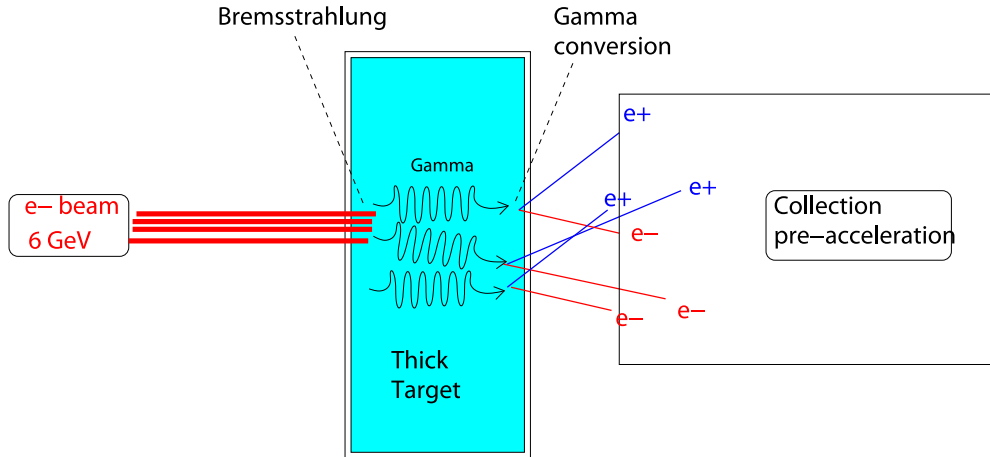


Figure 1.3: Schematic of the conventional positron source

from electrons and e^+e^- pair production by photons. For both processes the helicity transfer is most effective in the hard part of the spectra. The pair production cross section near the threshold rises with the photon energy. The higher the photon energy the larger is the positron yield. However, another important argument for a proper choice of the photon energy is to keep off the main nuclear resonances, thereby diminishing a harmful hadronic background [A. Ushakov(2006)]. Providing an intense positron beam with $2 \cdot 10^{10} e^+$ per bunch is one of the challenging aspects of an ILC positron source. To achieve this high current for positrons an intense photon source is required. The photon source will use the ILC electron beam directly with an undulator to generate an intense photon beam capable to produce the required number of positron per bunch. In the following, the basics concepts of positron sources are described.

Conventional positron source

A conventional positron source produces an unpolarized positron beam along the scheme suggested in [Sheppard(2003), Flöttmann(2005)]. In this scheme, an electron beam of 6.2 GeV energy bombards a high Z material target (W23Re) of several radiation length ($4.5 X_0$) to generate electron and positron pairs. The electron beam generates first bremsstrahlung photons which in turn produce e^+e^- pairs in the same target (see Fig. 1.3). The positrons produced are captured by an Adiabatic Matching Device (AMD) and a pre-acceleration stage.

Laser Compton backscattering.

A design of a polarized positron source for the ILC using a circularly polarized laser wave is proposed in [T. Omori(2003)]. Compton backscattering sources utilize backscattered circularly polarized laser light for the production of circularly polarized high energy photons which create e^+e^- pairs in a thin target (Fig. 1.4). Different solutions have been proposed, all requiring complex electron beam manipulations and high power lasers [T. Omori(2006)]. Here the challenges are mainly the laser, the laser-beam interaction point and the alignment. Some optimization for the total laser power is worked out and particular efforts are put on the optics. Presently ten CO₂ lasers are needed. An incident beam energy of 5.8 GeV is chosen, providing a maximum γ energy of 60 MeV [T. Omori(2006)]. One of the advantages of this method is to have the electron and positron main systems independent of each other. The 5.8 GeV electron drive beam is exclusively used for the positron source, while the undulator-based source has to use the main electron beam.

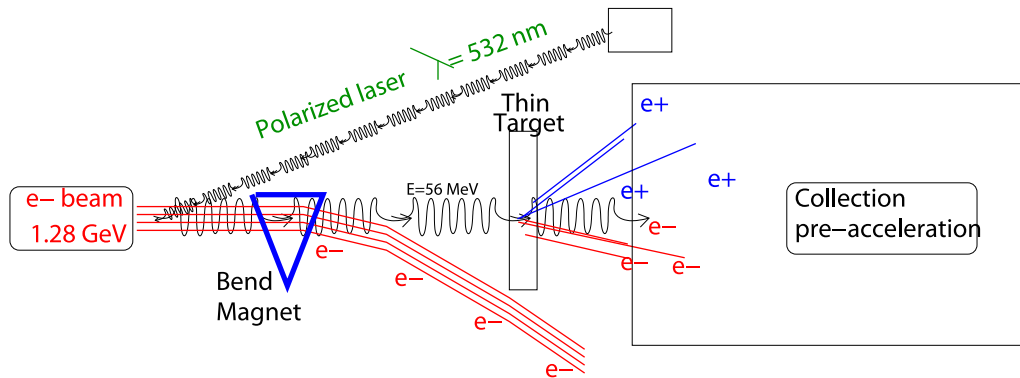


Figure 1.4: Scheme of the polarized positron source based on the Laser Compton backscattering developed at KEK.

Helical undulator-based polarized positron source

The undulator-based positron source uses a helical undulator placed at the 150 GeV point of the ILC electron beam [Flöttmann(2005)]. The electron beam is driven by a proper optics through a 60 m long helical undulator. The electron beam passing through the undulator generates photons. After

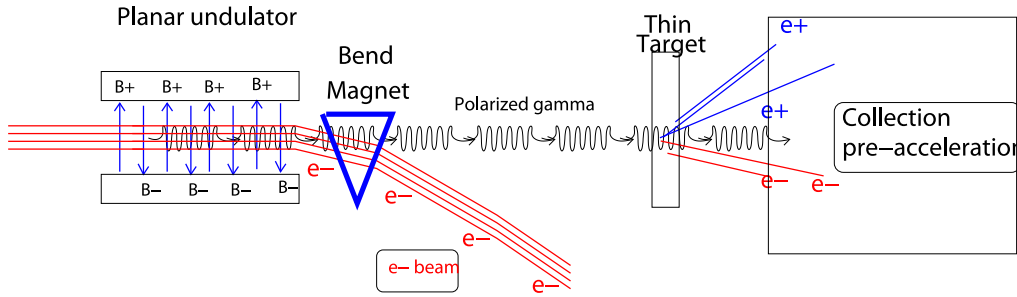


Figure 1.5: Schematic of the undulator (planar/helical) positron source.

the undulator section, the electron beam is guided back to the main linac for further acceleration (up to 250 GeV at the IP) (see Fig. 1.6). The photons pair-produce electrons and positrons in a relatively thin, high strength Ti-alloy target (0.4 radiation lengths X^0). The positrons from this process are collected and accelerated up to the damping ring energy of 5 GeV then injected to the main linac and further accelerated to collide with the electron beam at the IP .

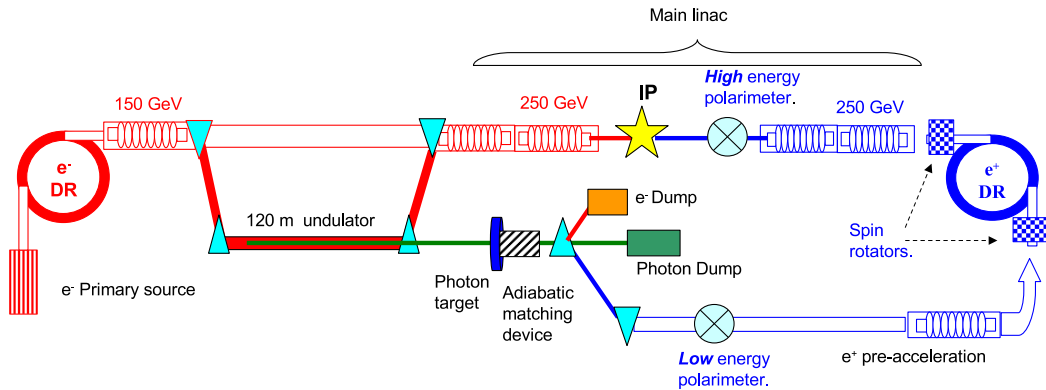


Figure 1.6: Scheme of the helical undulator based polarized positron source at the ILC

With a 186 m long undulator, a proper photon beam collimation, and spin rotators before and after the damping ring, the required positron intensity and polarization can be produced. In this layout, the positron source is designed with a 50% overhead and can deliver up to $3 \cdot 10^{10}$ positrons per electron bunch to the 400 MeV point before the damping ring. In this scheme, the expected positron polarization at the IP is about 60%.

parameter	Units	Values
positron/bunch		$2 \cdot 10^{10}$
bunch/pulse		2820
pulse repetition rate	Hz	5
e^+ energy	GeV	5
e^- beam energy	GeV	150-250
e^- beam energy loss	GeV	2.1
undulator period λ	mm	10
undulator strength K		1
undulator type		Helical
undulator length (unpol)	m	65 (unpol) 186 (pol)
photon energy (1st harmonic)	MeV	11-30
max. Photon beam power (unpol)	kW	95
target material		Ti-6%Al-4%V
max. target length	X_0	0.4
max. target absorption	kW	7
incident spot size on target	mm	0.75
positron polarization	%	60

Table 1.2: Undulator-based positron system parameters

1.3 Polarization Preservation

Low-energy beam capture and acceleration:

The transverse and longitudinal phase space of the positrons coming out of the target is matched to the 6-D acceptance of the downstream system by a longitudinally varying solenoidal field. The positrons are then accelerated up to the damping-ring energy of 5 GeV. Axial solenoid fields are used for the transverse capture optics at the low energies up to about 250 MeV. Thereafter, magnetic quadrupoles are used for focusing. In this low energy capture section, the longitudinal polarization is preserved. Also, in this region, depolarization due to the space charge effects is not expected.

Damping rings:

Only polarization parallel or anti-parallel to the guide fields of the damping ring is preserved. Thus the incoming longitudinal polarization must be rotated into a transverse polarization before the injection into the damping rings. This is done in the transport line leading from the end of the 5 GeV linac to the damping ring, utilizing an appropriate combination of dipole and solenoid fields (spin rotators). The vertical spins can be rotated back to

the longitudinal direction with an analogous system after the damping ring extraction line leading to the main linac.

It is important to avoid depolarizing spin-orbit coupling resonances in the damping ring by operating off the resonant energies. Depolarization effects due to the stochastic nature of photon emission can be estimated by comparing the time that a beam spends in the damping ring to the time constant for depolarization. This ratio is typically very small and hence depolarization in the rings is expected to be negligibly small [D.P. Barber(2002a), D.P. Barber(2002b), R.W. Assmann(2001)].

Main linac:

In the linac, the electric field and the particle velocity are essentially parallel. Then, according to the Thomas-Bargmann-Michel-Telegdi (T-BMT) equation [V. Bargmann(1959)] the electric field will cause negligible spin precession. The effects of the transverse field from the RF couplers and quadrupoles are negligible. There should be no loss of polarization in the main linac [G. Moortgat-Pick(2006)].

Beam delivery system:

After acceleration in the main linacs, the e^+e^- beams are brought to collision by the beam delivery systems. These beam lines contain bending magnets. According to the T-BMT equation, a beam deflection of $\delta\theta_b$ in a transverse magnetic field causes a spin rotation of $a\gamma\delta\theta_b \approx E(\text{GeV})/0.441(\text{GeV})\delta\theta_b$. Depolarization associated with synchrotron radiation in the transport system is expected to be negligible [G. Moortgat-Pick(2006)]. Care is needed to ensure that the polarization is precisely longitudinal (or transverse) whatever is needed at the interaction point.

Beam-beam interactions:

Loss of polarization will occur as the electron and positron bunches collide. The two responsible mechanisms are spin rotation due to the electric and magnetic fields in the incoming bunch and spin flip due to synchrotron radiation. The combined effect of these two mechanisms has been studied analytically [K. Yokoya(1988)] as well as numerically [Thompson(2001)]. At 500 GeV center-of-mass energy for the nominal ILC parameters [ICFA(2006)], the expected overall loss of polarization of either beam is $\Delta P/P \simeq 1\%$. How-

ever, the effective loss up to the point of interaction (luminosity-weighted) is only $\simeq 0.25\%$.

1.4 Polarimetry at the ILC

In addition to the beam polarization measurement obtained from the physics at the interaction point IP (polarization dependent cross sections), independent polarimeters are foreseen at the ILC to check the electron (positron) beam polarization close to the electron (positron) sources before the damping ring and close to the IP. For the optimization of the ILC operation those independent measurements are recommended. At the IP a laser Compton polarimeter is foreseen. The technic of the positron polarimeter is still unclear. The design of an apparatus will be challenging.

1.4.1 Laser Compton polarimeter

A laser Compton polarimeter is the recommended option for a polarimeter at high energy close to the interaction point. Laser photons hit the positron (electron) beam and are backscattered. The angular distribution of the backscattered photons depends on the polarization of the positron (electron) beam. With this approach it is possible to achieve very high precision in the polarization measurement as has been demonstrated at the SLC and HERA [V. Gharibian(2003)].

For a low energy polarimeter the situation is different. The asymmetry in the angular distribution of the backscattered photons is very small for energies around a few GeV or below. The signal rate depends on both the intensity of photon and positron (electron) beams. To achieve sufficient signal rates within an acceptable period either the size of the polarized positron beam has to be decreased substantially or a very high power laser would be needed. Hence, a Compton polarimeter is not considered as a solution for a low energy positron polarimeter at the source. The low energy polarimeter at the ILC is still under discussion and the main topic of Work Package 4 of the European linear collider design study the EUROTeV (WP4 [A. Schällicke(2006)]).

1.5 Physics Benefits from Positron Polarization at the ILC

Systematic studies reported in [G. Moortgat-Pick(2006)] have shown that polarized beams in an e^+e^- linear collider will largely help in the identification of new particles, in the search for new physics and in precision measurements of the coupling parameters. The polarization of the electron beam alone is already very useful in this respect. If the positron beam is also polarized, one can benefit further from:

1. an increase of the effective polarization: for instance, an 80% e^- polarization and a 60% e^+ polarization combine into an effective polarization of 94%;
2. a better precision in the measurements of the effective polarization;
3. a further reduction of background events: for instance, the number of W^-W^+ pairs is reduced by a factor 2 for a proper choice of polarization combination as compared to the case when only the e^- beam is polarized;
4. an increased sensitivity to non-standard couplings.

In addition to these improvements with longitudinal polarization, the transverse polarization of both e^- and e^+ would allow one to investigate CP violating couplings [B. Ananthanarayan and Bartl(2004)].

1.5.1 Longitudinal beam polarization

The e^+e^- annihilation cross sections can be subdivided into contributions of all possible spin configuration as shown in Fig. 1.7. In this figure, the thick arrow represents the direction of motion of the particle and the double arrow its spin direction. The first column indicates the corresponding cross section, the fourth column the fraction of this configuration and the last column the total spin projection onto the e^+e^- direction.

$$\sigma_{P_{e^-}P_{e^+}} = \frac{1}{4} \left\{ (1 + P_{e^-})(1 + P_{e^+})\sigma_{RR} + (1 - P_{e^-})(1 - P_{e^+})\sigma_{LL} + (1 + P_{e^-})(1 - P_{e^+})\sigma_{RL} + (1 - P_{e^-})(1 + P_{e^+})\sigma_{LR} \right\}, \quad (1.1)$$

where the cross section σ_{RL} is for a right handed electron and left handed positron beam. σ_{LR} , σ_{RR} , σ_{LL} are defined respectively.

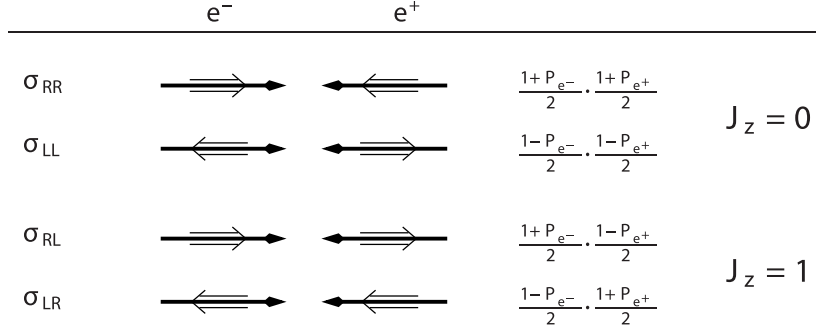


Figure 1.7: Possible different spin configurations in e^+e^- annihilation.

Two different scenarios for the e^+e^- annihilation can be distinguished.

- a) e^+e^- annihilation via the s-channel as illustrated in Fig. 1.8.
- b) e^+e^- scattering via a t-channel exchange as illustrated in Fig. 1.9.

In the s-channel (Fig. 1.8) the helicities of the incoming beams are coupled to each other. The Standard Model (SM) predicts an exchange particle to be a γ or a Z boson with $J = 1$ and leads to the only possible spin configuration in this case to be parallel; either σ_{RL} or σ_{LR} .

In the t-channel (Fig. 1.9), the helicities of the final state particles are directly coupled to the helicities of the incoming beams. In such a scenario, the exchanged particle could be a vector or a scalar and the helicity of the incoming particle is directly coupled to the vertex and is independent of the helicity of the second incoming particle. Therefore all spin configurations are in principle possible.

1.5.2 Effective polarization

In the case of the Standard Model, where only vector currents contribute to e^+e^- annihilation, the cross section can be simplified to

$$\sigma_{P_{e^+}P_{e^-}} = (1 - P_{e^+}P_{e^-}) \sigma_0 [1 - P_{\text{eff}}A_{\text{LR}}]. \quad (1.2)$$

Here A_{LR} is the left-right asymmetry, discussed in the next section and P_{eff} is the so-called effective polarization defined as

$$P_{\text{eff}} = \frac{P_{e^-} - P_{e^+}}{1 - P_{e^-}P_{e^+}}. \quad (1.3)$$

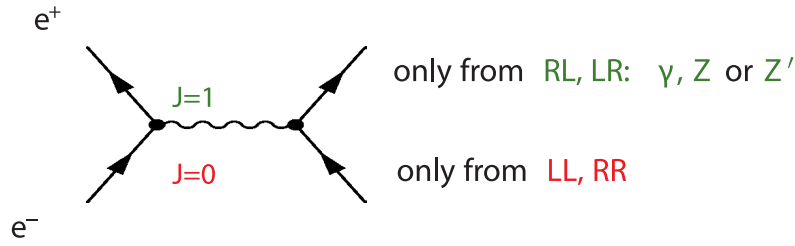


Figure 1.8: Possible configurations in s -channel diagrams: the helicities of the incoming e^+e^- beams are directly coupled. Within the Standard Model only the recombination into a vector particle with $J = 1$ is possible, which is given by the LR and RL configurations. New physics modes might contribute to $J = 1$ and to $J = 0$.

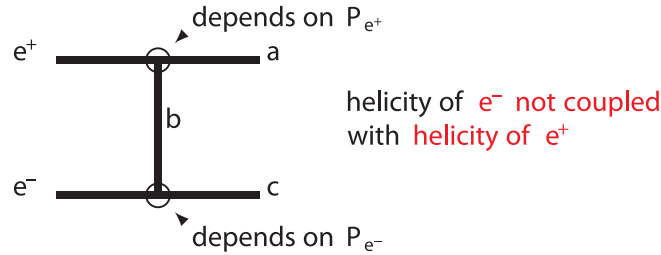


Figure 1.9: Possible configurations in t - and u -channel diagrams: the helicity of the incoming beam is directly coupled to the helicity of the final particle and is completely independent of the helicity of the second incoming particle.

If only one beam is polarized, the effective polarization is identical to this beam’s polarization. But if both beams are polarized it is substantially larger. For example in the case of an 80 % left-handed electron beam and a 60 % right-handed positron beam the effective polarization is already 94%. The effective polarization increases the cross section by up to a factor of two and – more important – it reduces the errors of the polarization measurement. For electron and positron polarimeters with a fixed precision, the effective polarization will be determined with a three times higher precision for the example above (80 %/60 % polarization).

1.5.3 Left-right asymmetry

One of the options of the physics program of the ILC is the resonant production of large numbers ($\approx 10^9$) of Z bosons in a run with a center-of-mass

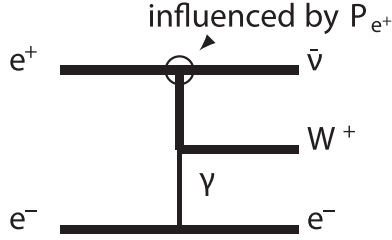


Figure 1.10: Single W^+ production: the vertex $e^+W^+\bar{\nu}$ depends only on P_{e^+} .

energy equivalent to the Z mass (GigaZ). The goal is to tighten the already very restrictive tests of the Standard Model performed at LEP and SLC further. The key will be a measurement of the left-right asymmetry A_{LR} with unprecedented precision. The A_{LR} describes the difference in cross section initiated by left-handed and right-handed couplings of the electrons and positrons to the Z boson:

$$A_{LR} = \frac{\sigma_{LR} - \sigma_{RL}}{\sigma_{RL} + \sigma_{LR}} = \frac{1}{P_{\text{eff}}} \frac{\sigma_{-+} - \sigma_{+-}}{\sigma_{-+} + \sigma_{+-}} \quad (1.4)$$

Here σ_{LR} , σ_{RL} are the cross sections for fully polarized beams, while σ_{-+} , σ_{+-} indicate the measured cross sections with their true beam polarization. The measurement relies on a precise determination of the effective polarization. It directly benefits from the increased precision through positron polarization described in the previous section. A substantial improvement over LEP and SLC is only possible with positron polarization.

1.5.4 Standard Model Higgs physics

One of the major physics goals at the ILC is the precise analysis of all the properties of the Higgs particle. For a light Higgs boson the two major production processes, Higgs-strahlung $e^+e^- \rightarrow HZ$ and WW fusion $e^+e^- \rightarrow H\nu\bar{\nu}$ (Fig. 1.11), will have similar rates at $\sqrt{s} = 500$ GeV. Beam polarization will be important for background suppression and a better separation of the two processes. Furthermore, the determination of the Higgs couplings is improved when both beams are polarized. For example in Table 1.3 the scaling factors, i.e. the ratios of polarized and unpolarized cross sections, are compared for two cases: (1) $(P_{e^-}, P_{e^+}) = (\pm 80\%, 0)$, and (2) $(P_{e^-}, P_{e^+}) = (\pm 80\%, \mp 60\%)$. The table shows that there is a gain of a factor $(1.26/0.08)/(0.87/0.20) \sim 4$ in the ratio $\sigma(HZ)/\sigma(H\nu\bar{\nu})$ when left-handed polarized positrons are used in addition to right-handed polarized electrons.

Configuration (P_{e^-}, P_{e^+})	Scaling factors	
	$e^+e^- \rightarrow H\nu\bar{\nu}$	$e^+e^- \rightarrow HZ$
(+80%, 0)	0.20	0.87
(-80%, 0)	1.80	1.13
(+80%, -60%)	0.08	1.26
(-80%, +60%)	2.88	1.70

Table 1.3: Higgs production scaling factors, in the Standard Model at $\sqrt{s} = 500$ GeV for different polarization configurations with regard to the unpolarized case [Desch(1999), Moortgat-Pick and Steiner(2001)].

The relative contribution of HZ and WW fusion can be extracted with two different polarizations without much model assumptions.

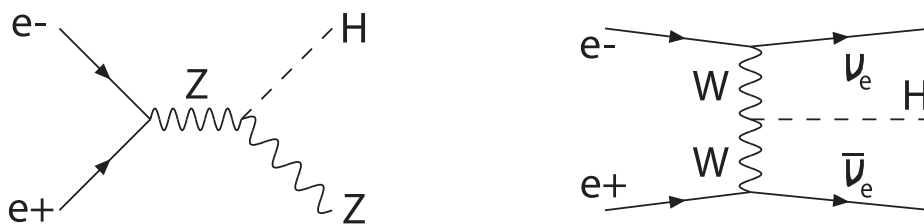
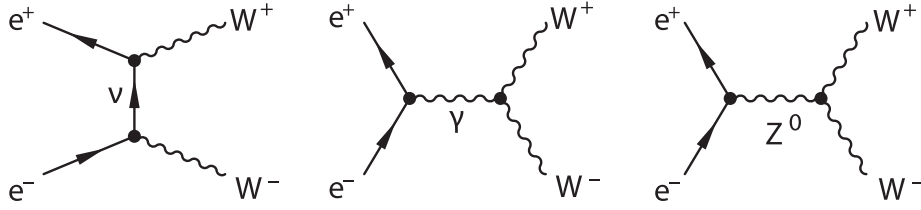
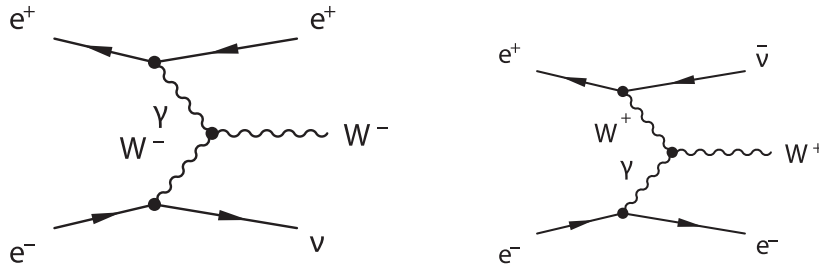


Figure 1.11: Main production mechanism of the standard model Higgs boson at the ILC

1.5.5 Suppression of W pairs

W pair production is an interesting process in many aspects, but for certain rare processes it is a severe background. Right-handed electron polarization very efficiently suppresses this background as well as single Z production via WW fusion, and $e^+e^- \rightarrow Z\nu_e\bar{\nu}_e$. At $\sqrt{s} = 500$ GeV these are important backgrounds for a light Higgs boson. For the WW case (Fig. 1.12) the suppression can be up to an additional factor 2 if left-handed polarized positrons are available compared to the case with only right-handed polarized electrons. Positron beam polarization turns out to be also a powerful tool to suppress the W background from single W production, $e^+e^- \rightarrow W^-e^+\nu_e$ and $e^+e^- \rightarrow W^+e^-\bar{\nu}_e$ (see Fig. 1.13).

Figure 1.12: Production of W pairs in e^-e^+ annihilation.Figure 1.13: Single W production in e^-e^+ annihilation.

1.5.6 Supersymmetry

In supersymmetric extensions of the Standard Model a super-partner is assigned to each particle of the Standard Model. A perfect Supersymmetry would require super-partners with masses identical to the Standard Model particles, which is obviously not the case. The Supersymmetry – if it exists at all – is broken. There are some indications that the masses of the super-partners are in the TeV region and many of them might be discovered with the LHC and ILC. After a discovery it will be important to determine the quantum numbers of the super-partners and their assignment to the Standard Model particles. For example the left and right-handed electrons of the Standard Model each have a super-partner: selectron left (\tilde{e}_L) and right (\tilde{e}_R).

Beam polarization	$e^+e^- \rightarrow W^+W^-$	$e^+e^- \rightarrow ZZ$
(+80%, 0)	0.20	0.76
(-80%, 0)	1.80	1.25
(+80%, -60%)	0.10	1.05
(-80%, +60%)	2.85	1.91

Table 1.4: Scaling factors, of WW and ZZ production at $\sqrt{s} = 500$ GeV with and without positron polarization [Desch(1999), Moortgat-Pick and Steiner(2001)].

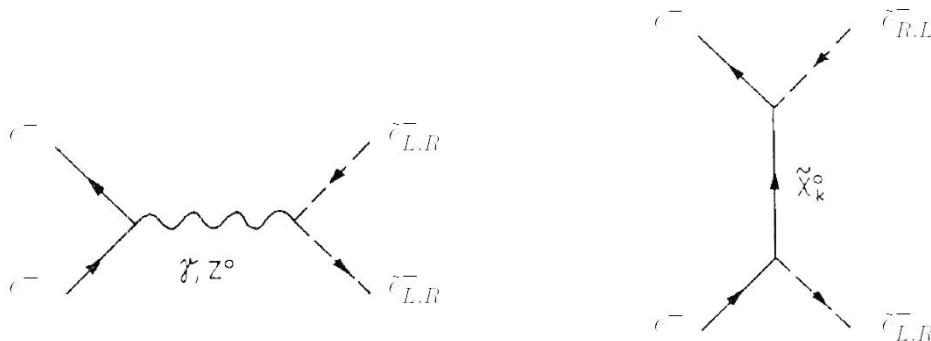


Figure 1.14: Selectron production and the ILC: γ , Z -exchange in the s -channel (left) and neutralino exchange $\tilde{\chi}_1^0, \dots, \tilde{\chi}_4^0$ -exchange in the t -channel (right).

The selectrons are spin 0 bosons and have no handedness themselves. The indices L and R only indicate the assignment to e_L and e_R . Once a selectron is discovered one wants to identify whether it is the partner of the left- or right-handed electron or maybe a mass degenerate combination of both. This identification is only possible, if both beams are polarized.

Figure 1.14 shows the two Feynman diagrams contributing to the production of selectrons at the ILC. In the s -channel process left- and right-handed partners always couple with the same strength. But in the t -channel process the selectrons couple directly to the beam and only the proper super-partners are produced, i.e. a right-handed positron beam will only produce (\tilde{e}_R^+).

1.5.7 Summary of the physics case

Many relevant physics arguments show that positron polarization, combined with the clean experimental environment provided by a linear collider, would allow one to improve dramatically the search potential for new particles and the disentanglement of their dynamics. This would represent a crucial step towards the understanding of the nature of fundamental interactions. Concurrently, the Standard Model and its parameters could be scrutinized and determined with unparalleled precision. The availability of positron polarization would allow significant progress also in this respect.

In **direct searches**, the physics potential of the ILC is strongly improved if one can exploit simultaneously the independent polarizations of both beams, particularly in the following regards:

- The chiral structures of interactions in various processes can be iden-

tified independently and unambiguously. This provides the possibility of determining the quantum numbers of the interacting particles and testing stringently model assumptions. Several of these tests are not possible with polarized electrons alone.

- The larger number of measured observables is crucial for disentangling the new physics parameters in a largely model independent approach.
- Transverse polarization of both beams enables the construction of new CP-odd observables using products of particle momenta, and further enlarges the number of observables available to constrain the new physics parameters.
- The enhanced rates with suitable polarizations of the two beams would allow for better accuracy in determining cross sections and asymmetries. This increase of the signal event rate may even be indispensable, in some cases, for the observation of marginal signals of new physics.
- A more efficient control of background processes can be obtained. The higher signal-to-background ratio may be crucial for finding manifestations of particles related to new physics and determining their properties. Important examples are the searches for signatures of massive gravitons, whose existence is foreseen by models with extra dimensions, and of supersymmetric particles.

In **indirect searches** for new physics, the clear advantages of having both beams polarized simultaneously include the following.

- The enhancement of cross sections, and correspondingly of the rates, by effective use of the polarizations, leads to a reduction in the statistical uncertainties.
- Significant increases in sensitivity to new physics at high energy scales can be achieved, with the possibility to elucidate the associated interactions.
- The increase in the sensitivity to non-standard couplings due to the synergy of high energy, high luminosity and especially of different possible initial polarization configurations will allow one to disentangle different kinds of interactions.
- The left-right asymmetry, which can be crucial for distinguishing different models, is often limited by systematic uncertainties. These can be reduced significantly when both beams are polarized.

- There is an increase in the sensitivity to new interactions which are not of the current-current type, such as those mediated by gravitons or (pseudo)scalar exchanges.

Conclusion

Among various methods of obtaining longitudinally polarized positrons for future linear colliders, the most promising schemes are those using circularly polarized, high-energy photons for positron production. Most effectively such photons are emitted from electrons passing through a helical undulator or colliding with the circularly polarized laser wave. While an electron energy of several GeV is appropriate in the laser case, hundreds of GeV are needed for undulators to produce the required number of positrons for the ILC. The advantage of the laser scheme is the possibility to switch off the photon (and thereby positron) polarization. It seems, however, the development of a laser systems with record parameters (very high power, high repetition rate) and rather sophisticated optics might fail. However in the undulator scheme, the easy operations to meet the ILC requirement in beam (bunch) time structure, polarization and reliability have put the undulator based positron source as a suitable approach for the ILC machine.

The production of polarized positron beam will play an important role in the physics program at the ILC. Many studies have shown that polarized positron in addition to a polarized electron beams will lead to a well defined initial state for particles in collision and a better understanding to the physics after the collision.

Chapter 2

The E-166 Experiment

2.1 Introduction

E-166 is a proof-of-principle experiment with the main goal to test the undulator-based polarized positron source for implementation at the International Linear Collider [G. Alexander(2003)]. The experiment was carried out at SLAC where it benefitted from the high quality electron beam in the Final Focus Test Beam (FFTB) (see Fig. 2.1). The production of polarized positrons is based on the gamma conversion process where the positron inherits the polarization of the primary photon. Thus a highly polarized photon beam is required. While an experiment at KEK utilized Compton back scattering [T. Omori(2003), T. Omori(2006)], E-166 used a 46.6 GeV electron beam passing through a one meter-long helical undulator to provide an intense photon beam with a high degree of circular polarization. Beyond this, the experiment offered the possibility to study under more general aspects the polarization dependent cross sections of fundamental processes with polarization transfer in electromagnetic cascades. In this chapter, the principle of the E-166 experiment and the relevant components of the setup are described with particular focus on the CsI(Tl) calorimeter.

2.2 Principle of the E-166 Experiment.

The setup of the E-166 experiment had three main components: First, the experiment provided a circularly polarized photon source using a helical undulator, then the polarized photons were converted in a thin target to longitudinally polarized positrons and finally both the photon and the positron polarization were measured using the Compton transmission method. The goal of the experiment was to demonstrate that such a technique can provide



Figure 2.1: Top: Aerial view of SLAC with the 3 km linear accelerator and the end-stations. Bottom: The accommodation of the endpoint of the Final Focus Test Beam (FFTB) in the SLAC end-station area.

polarized positron beams of sufficient quality for use at the ILC.

A schematic view of the E-166 undulator-based positron source is shown in Fig. 2.2. A 1 meter-long, short-period, pulsed helical undulator was installed in the final focus test beam. A low-emittance 46.6 GeV electron beam passed through the undulator and generated circularly polarized photons with energies up to 8 MeV. These polarized photons were converted to polarized positrons via pair production in a thin ($0.2 X_0$) tungsten target. The produced positrons were filtered by their energy in a magnetic spectrometer. The experiment measured simultaneously the yield and polarization of the undulator photons and the positrons. For positrons, the longitudinal polarization was measured for five selected e^+ energies to derive the energy dependence of the polarization and to crosscheck with the expectations from the simulation based on theoretical models [Olsen and Maximon(1959)] .

Figure 2.2 shows a wide range of detectors, deployed in the FFTB and arranged in two sets. One set of devices was aligned along the photon line and a separate set along the positron nominal orbit. In the photon line, the photon yield was measured by two counters: an aero-gel Cherenkov counter and a silicon counter. An identical pair of counters located behind the photon analyzing magnet measured the transmitted photon flux. In addition to the photon counters a SiW calorimeter measured the energy of the transmitted photon beam. The positron flux was measured directly by a 4 quadrant single layer silicon detector located at the exit window of the positron spectrometer chamber. Downstream the positron analyzing magnet, the transmitted signal was monitored by a nine element CsI(Tl) calorimeter.

2.2.1 Production of Circularly Polarized gamma Rays

The Helical undulator

The experiment used a one meter-long helical undulator in the 46.6 GeV electron beam line to produce photons with a high degree of circular polarization. The reliable functioning of the undulator was crucial. The positron yield and degree of longitudinal polarization were closely related to the quality of the primary photon beam.

The idea of a polarized positron source based on radiation from a helical undulator was first proposed by V.E. Balakin and A.A. Mikhailichenko [Balakin and Mikhailichenko(1979)]. The undulator is characterized by a helical profile of its magnetic field. The helical profile is obtained by two currents running in opposite directions through conducting wires wound to a double helix around the e^- beam axis. In this configuration, the z component

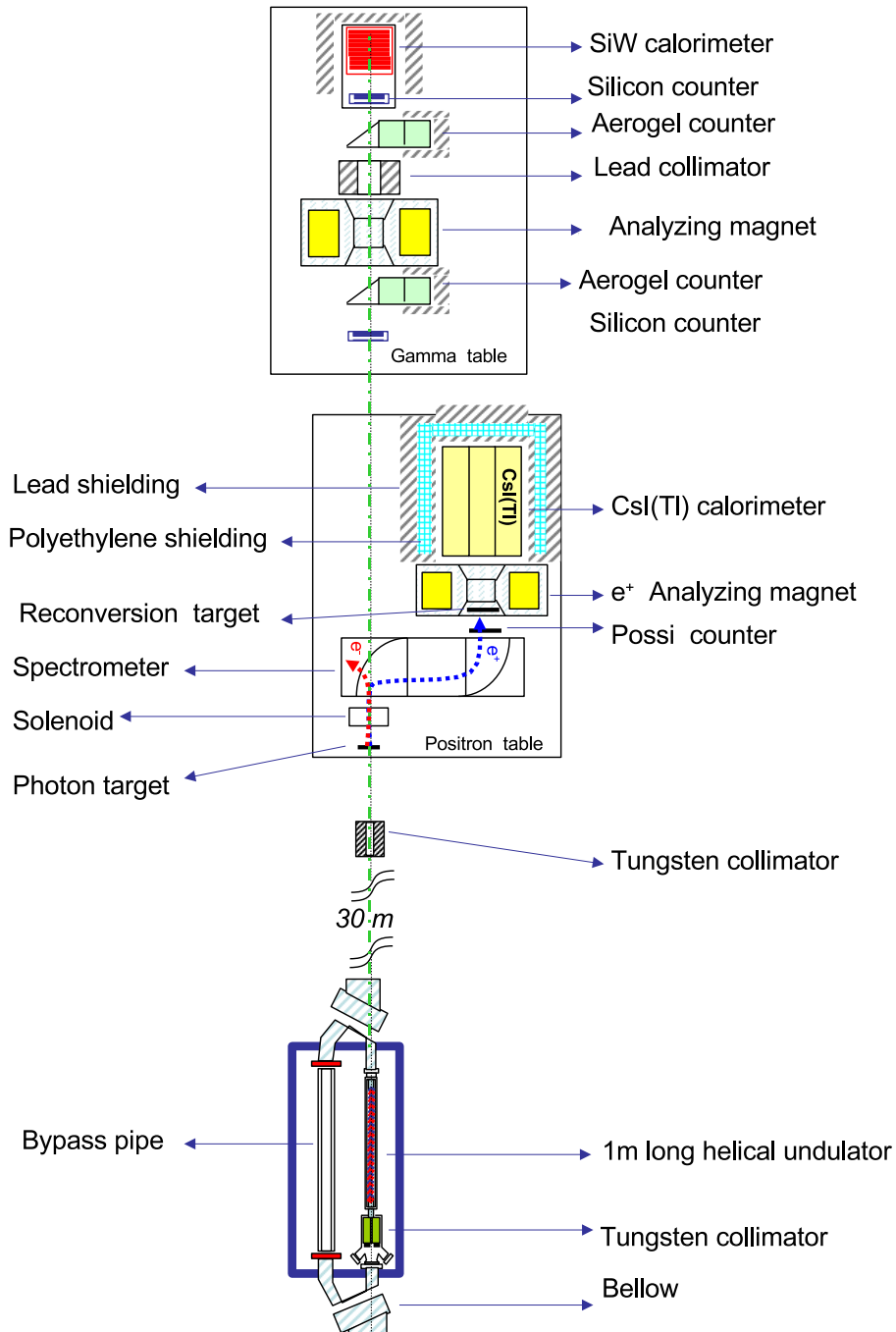


Figure 2.2: Synoptic scheme of the E166 experimental setup at the FFTB (the electron beam is from bottom to top)

of the resulting magnetic field vanishes and the transverse field component rotates along a helix. Basic formulas, radiation and polarization of the undulator are discussed in Section 4.2.

In the setup, the helical undulator was mounted parallel to a bypass pipe on a moving table. The degrees of freedom of the undulator table was controlled by three stepping motors for angular (and up/down) motion (Y1, Y2 and Y3) and two stepping motors for lateral motion (X1 and X2) (Fig. 2.3 and 2.4). The undulator and bypass pipe were both connected to the electron beam pipe via bellows and the entire system was controlled by two hydraulic movers to permit the electron beam to either pass through the undulator or through the bypass. At the entrance side of the undulator, a tungsten collimator was mounted to protect the undulator components. A phosphor screen with a CCD camera monitored the electron beam during the alignment procedure. In addition to the phosphor screen, the electron beam parameters were measured using Beam Position Monitors (BPMs) for orbit X-Y, a wire scanner and Optical transition Radiation (OTR) for beam size and a pickup coil called toroid (for beam current). The parameters of the electron beam are listed in Table 2.1 and the undulator parameters, are discussed in Section 4.2 and listed in Table 4.1. The alignment procedure and operation are described in section 2.7.

E_{e^-} [GeV]	f_{rep} [Hz]	N_{e^-} e ⁻	$\gamma\epsilon_x = \gamma\epsilon_y$ [m-rad]	β_x, β_y [m]	σ_x, σ_y [μ m]	$\frac{\sigma_E}{E}$ [%]
46.6	10	$0.35 \cdot 10^{10}$	$2.0 \cdot 10^{-5}$	7.8, 7.8	40	≤ 0.3

Table 2.1: The electron beam parameter for the E-166 experiment.

2.2.2 Production of polarized positrons

Positrons were produced by gamma conversion of the undulator photons passing through a relatively thin, solid conversion target. In the e^+e^- creation process, the leptons inherit the polarization of the primary photons. The conversion target station designed for the experiment was a multiple-target system containing four targets of two different materials each with two different thicknesses embedded in the primary vacuum system. A simplified scheme of the multiple-target system is shown in Fig. 2.5 and 2.6. Target thicknesses and materials are listed in Table 2.2. The four conversion targets were mounted on an up-down moving arm driven by a stepping motor. In addition to the four conversion targets, an empty hole was included to study the original primary photon flux without attenuation (due to the conversion process).

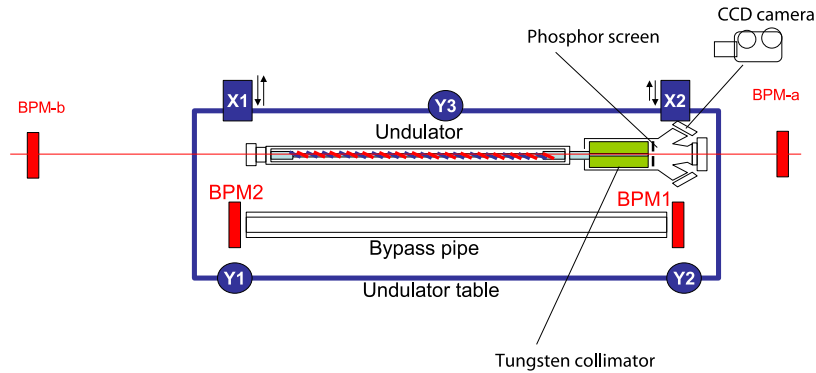


Figure 2.3: Synoptic scheme of the undulator table and the monitoring devices (the electron beam passes the undulator from right to left)

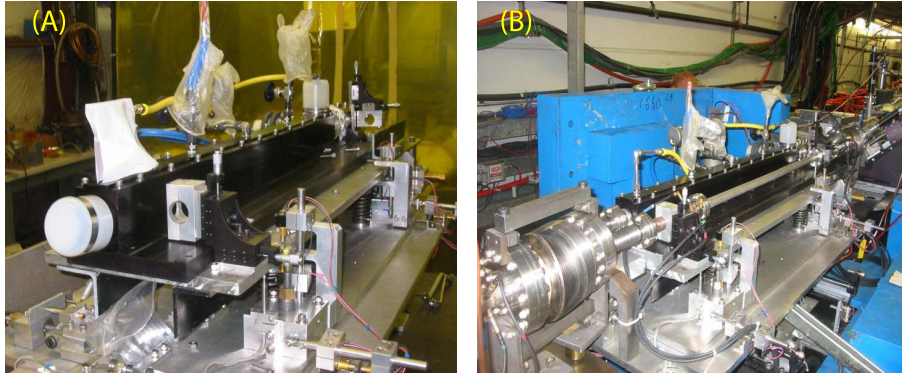


Figure 2.4: (A) The E-166 helical undulator. (B) The undulator table: helical undulator mounted parallel to the bypass pipe.

During the E-166 operations, the position of the up-down moving arm, and thus the choice of the conversion target, was remotely controlled from the Main Control Center (MCC) at SLAC. The original plan was to use all four targets to study the effect of the target thickness and material on the positron yield and polarization. However, due to the tight time schedule for the E-166 running, only the thin tungsten target (0.81 mm , $0.2 X_0$) was used.

The choice of thin conversion targets up to about $0.5 X_0$ with dense material such tungsten and titanium is suitable to achieve high positron yield and to preserve the longitudinal polarization. When an e^+e^- pair is created in the target, low energy positrons are stopped in the bulk while positrons with relatively high energy escape from the target and lose a fraction of their energy. The energy loss by bremsstrahlung is accompanied by a slight

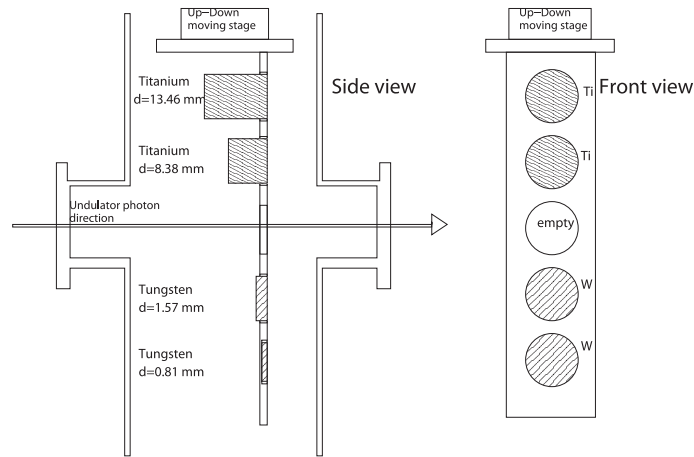


Figure 2.5: Schematic of the multiple-target system: Two tungsten targets, two titanium targets and one empty space. The targets were mounted and aligned to the e^+ exit window.

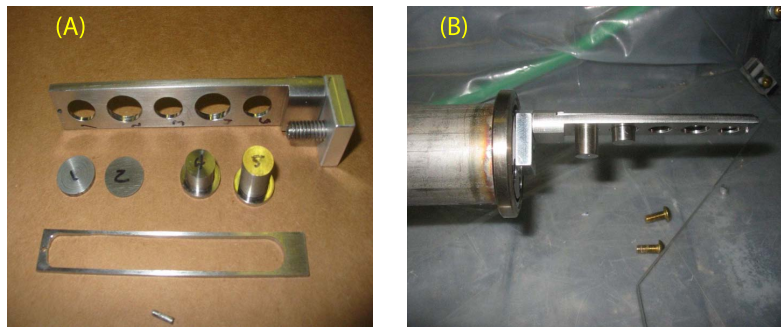


Figure 2.6: (A) Multiple-target system (dismounted). (B) Multiple-target system mounted on the moving arm.

loss of polarization (see Section 3.5.2). However, the energy loss is stronger than the polarization loss. For targets thicker than about $0.5 X_0$ the positron yield and polarization decrease [Flöttmann(1993), G. Alexander(2003)].

2.2.3 Polarimetry in the E-166 experiment

Both the circular polarization of the undulator photons and the longitudinal polarization of positrons were measured simultaneously using the Compton transmission method. The first experiment that was able to measure the circular polarization of gamma rays with the Compton transmission method was done by Gunst and Page [Gunst and Page(1953)] in 1953. In a transmission Compton polarimeter, the polarized photons are analyzed by measuring

Target	Material/Alloy	Composition	Thickness	
			[mm]	[X_0]
01	Titanium (Ti)	Not specified	13.46	~ 0.4
02	Titanium (Ti)	Not specified	8.38	~ 0.25
03	Tungsten (W)	90% W, 4% Ni, 3% Cu, 3% Fe	1.57	~ 0.38
04	Tungsten (W)	90% W, 4% Ni, 3% Cu, 3% Fe	0.81	~ 0.2

Table 2.2: Material and thickness of the multiple-target system used in the E-166 experiment.

the asymmetry in their transmission through magnetized iron exploiting the polarization dependence of Compton scattering. This polarimeter has the advantage that low energy background photons are suppressed in the energy measurement. It can even be used for beams with large angular divergence.

Iron is the best known ferromagnetic material. The maximum electron polarization at saturation is 8.52 %. This value must be temperature corrected, as ferromagnetism becomes weaker with increasing temperature. For iron the magnetization vanishes at $T_{Curie} = 770C^o$. The polarization of the iron core of the positron analyzing magnet is $P_{e^-} = 6.94\% \pm 0.17$. The relation between magnetization and polarization is given by:

$$P_{e^-} = 2 \cdot \frac{g' - 1}{g'} \cdot \frac{M}{n\mu_B} \quad (2.1)$$

Where

M	magnetization
$g' = 1.919 \pm 0.002$	magneto-mechanical factor
ρ_{e^-}	electron density
μ_B	Bohr magneton

Depending on the photon energy and its circular polarization, the transmission through magnetized iron is given by:

$$T = N e^{-nL(\sigma_{pair} + \sigma_{photo} + \sigma_{Compton})} e^{-nL\sigma_{pol}P_{\gamma}P_e} \quad (2.2)$$

L	the thickness of the iron core
n	the electron density
σ_{pair}	pair production cross section
σ_{photo}	photo effect cross section
$\sigma_{Compton}$	Compton scattering cross section for unpolarized iron
σ_{pol}	polarization dependent Compton cross section
P_γ	photon polarization.
P_e	target Electron polarization ($\sim 7\%$ at saturation).

By reversing the iron magnetization and for small $nL\sigma_{pol}$ the asymmetry δ can be approximated to:

$$\delta = \frac{T_+ - T_-}{T_+ + T_-} = A_\gamma P_\gamma P_e \quad (2.3)$$

T_+ and T_- stand for the transmission for parallel and anti-parallel target electron polarization.

$A_\gamma = nL\sigma_{pol}$ is the analyzing power. The photon polarization P_γ can thus be inferred from the measured asymmetry if A_γ and P_e are known.

In practice the analyzing power is determined from Monte Carlo simulations because it depends on the photon energy and must therefore be convoluted over the photon spectrum. The analyzing power is very sensitive to the polarimeter geometry. Detailed simulation studies on the polarization dependent processes and on the analyzing power are presented in Section 4.6.2.

The photon polarimeter consists of three main components: a 150 mm thick, 50 mm diameter iron absorber with a reversible magnetization, a silicon counter and a SiW calorimeter for the rate and energy measurement of the transmitted photons (Fig. 2.7).

To use the Compton transmission polarimeter also for positrons, the positrons have to be converted back into polarized photons via bremsstrahlung or annihilation in a relatively thin reconversion target (Fig. 2.7). The positron polarimeter consists of three main components: a $0.5 X_0$ tungsten target, a magnetized iron absorber ($\simeq 75$ mm thick, 50 mm diameter) and a CsI(Tl) calorimeter (Fig. 2.8).

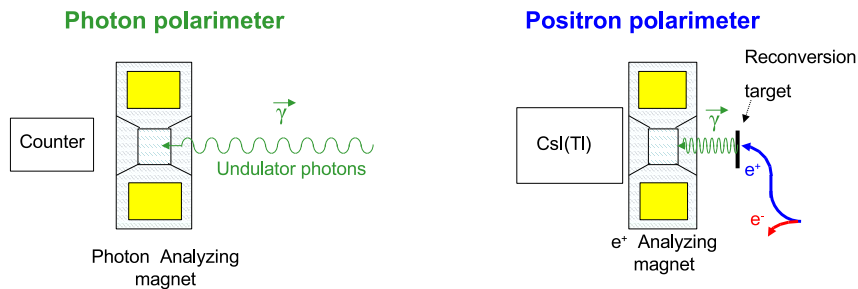


Figure 2.7: Principle of the photon and positron polarimeter

2.3 Positron Diagnostic

The instrumentation on the positron table consists of three parts: the positron production target, the positron transport system and finally the polarimeter.

2.3.1 The positron transport system

The positron transport system guides the positrons from the production target to the reconversion target through a magnetic spectrometer. The positron spectrometer is a system of two magnets separated by 25.4 cm drift space with momentum selection jaws in between. The magnets have opposite polarities so that the total deflection is approximately zero and the transverse displacement is about 46.35 cm (see Fig. 2.9). The cross section of the magnet poles are 90° sectors of a circle. To provide vertical focusing the gap is tapered along the circle radius such that the gap opening is 5.33 cm in the region $r < 6.10$ cm increasing linearly to 10.41 cm at the largest radius of $r = 20.34$ cm. The return flux passes through iron plates on top and bottom connecting the two magnets. The plate dimensions are 73.66 cm \times 20.32 cm \times 3.81 cm and are supported by four cylindrical spacers. For the central orbit the bending radius in each of the magnets is $R_0 \approx 13.08$ cm. In this design the spectrometer selects a well defined positron momentum leading to a quasi-monochromatic beam at the reconversion target.

In addition to the spectrometer, the transport system included a solenoid and a vacuum chambers shown in Fig. 2.9 and 2.10. The produced e^+e^- pairs emerging from the target, with a wide angular distribution, were first focused by the a magnetic field of the solenoid located at 66.92 mm from the target. After the solenoid, the e^+e^- pairs passed the first 90° bending magnet. In this region, electrons were separated from positions and dumped inside the vacuum chamber. A set of jaws with variable aperture was placed between

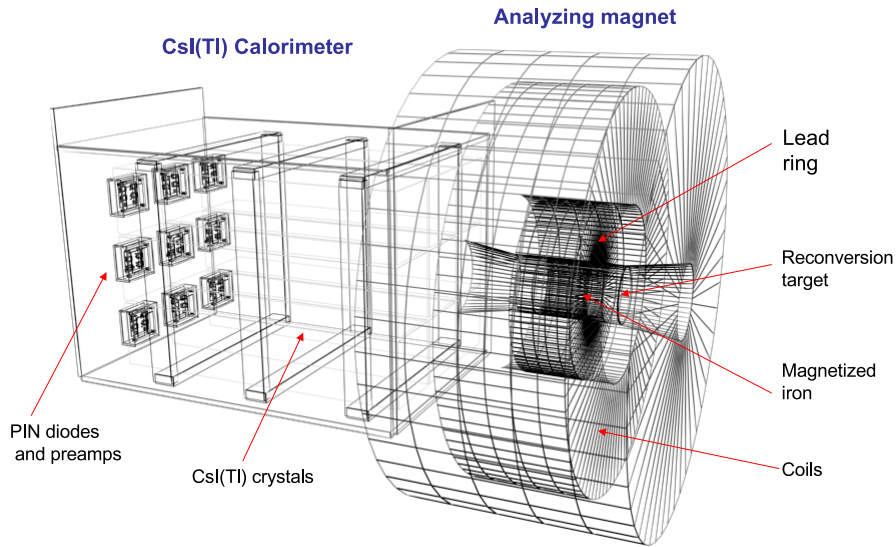


Figure 2.8: Perspective view of the reconversion target, Analyzing magnet and CsI(Tl) calorimeter.

the two 90° bending magnets. The jaws provided the option for high resolution momentum scans. Positrons that pass through the momentum-selecting slit were guided to the reconversion target by the field of the second bending magnet. For a fixed spectrometer current (I_S), the solenoid current (I_L) were optimized for maximum transmission defining the setting point (I_L, I_S). A detailed GEANT-based simulation of the positron transport system is described in section 2.3.1.

Substantial lead and tungsten shielding around the transport system was included to suppress background photons generated during the transport process and reaching the CsI(Tl) calorimeter. This soft background is generated at the production target or when positrons and electrons scatter in material during the transport process.

Momentum-Current relation of the spectrometer (spectrometer energy calibration)

The plan of E-166, was to study the positron's longitudinal polarization as a function of their energy (momentum). Thus, the positron polarization had to be measured at different spectrometer settings. The spectrometer current was successively set to five values $I_S = 100, 120, 140, 160$ and 180 A providing

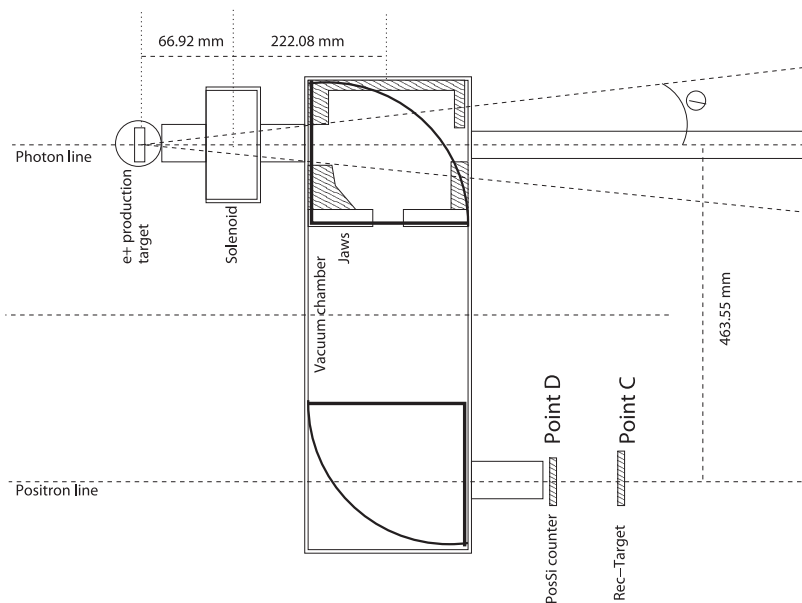


Figure 2.9: Top view of the positron transport system showing the different components (Vacuum chamber, Solenoid and spectrometer) and their distances relative to the e^+ production target. In this figure the photon/positron beam is passing the transport system from left to right.

five different positron momenta. During the run periods of E-166 no in-situ energy measurements of the positron beam was performed. The only known parameter was the spectrometer current.

The knowledge of the magnetic field as a function of the current is crucial and it is closely related to the positron energy selected by the spectrometer. Also, The determination of the calibration function $E_{e^+} = f(I_S)$ relating the positron energy (momentum) for a given spectrometer current required a calibration of the entire transport system. In a test experiment carried out at SLAC after the E-166 runs, the spectrometer's magnetic field was measured as a function of the current using a Hall probe at the location of the maximum magnetic field (in the region of minimum gap between the dipole yokes). In this region, the magnetic field B_S as a function of the spectrometer current I_S was expected to be linear, however the measurement has revealed a non linearity between B_S and I_S as shown in Fig. 2.11. This non linearity has been attributed to a saturation effect in the dipole yokes. The curve $B_s = f(I_S)$ was fitted by a second order polynome leading to a so-called quadratic relation given by:

$$B_S(I_S) = -1.683 \cdot 10^{-6} I_S^2 + 1.536 \cdot 10^{-3} I_S + 1.841 \cdot 10^{-3} \quad (2.4)$$

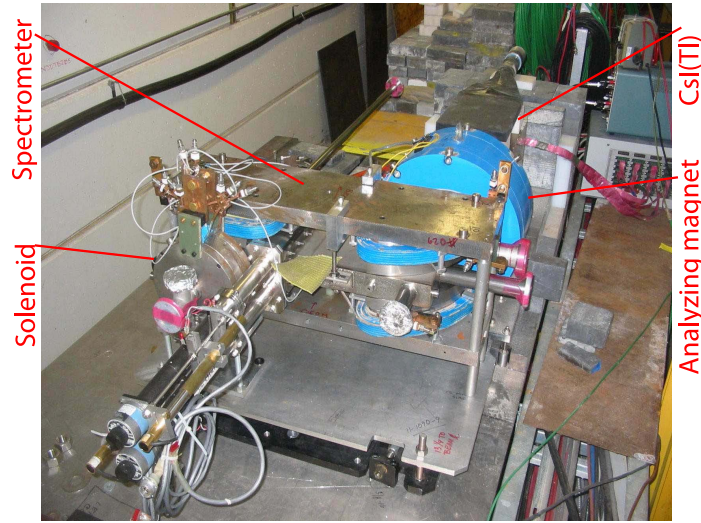


Figure 2.10: Picture of the positron transport system: The solenoid, spectrometer, analyzing magnet and the CsI(Tl) calorimeter.

This relation given by Eq. 2.4 is used as an input to the Geant4 simulation to crosscheck the spectrometer calibration as discussed in Section 4.4.3 and 4.5.2.

For the spectrometer calibration the β -spectrum of a ^{90}Sr source with an endpoint total energy at 2.75 MeV was used measuring its transmission through the transport system. The value of the endpoint total energy was corrected for energy loss in air (no vacuum) and also for the energy loss in the $75\ \mu\text{m}$ stainless steel window at the exit of the vacuum chamber. The corrected endpoint total energy is about 2.515 MeV. The experimental procedure for the calibration was similar to methods used for β -spectroscopy [Bugg(2006)]. It can be summarized in four steps:

- First, the β -source was put at approximately the same position as the conversion target.
- A silicon counter was mounted at the exit of the spectrometer vacuum chamber and the rate of the transmitted electrons was recorded.
- Starting from a low value the spectrometer current was increased progressively with a small step size until the electron rate vanished.
- The spectrometer current corresponding to the endpoint energy of the ^{90}Sr source was determined using Kurie plots.

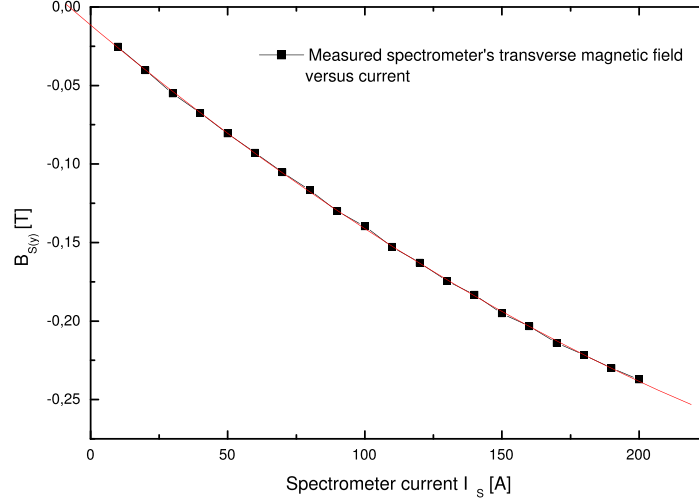


Figure 2.11: The measured spectrometer's transverse magnetic field B_s versus the spectrometer current I_S showing a quadratic behavior given by Eq. 2.4.

From the analysis of the β -spectrum recorded at the PosSi counter, the endpoint energy 2.515 MeV corresponds to a spectrometer current of about 48 A. The positron energy for different spectrometer current $I_S = 100, 120, 140, 160$ and 180 A was derived by extrapolation using Eq. 2.4. The result of the calibration are listed in Table 2.3.

I_S [A]	B_S [T]	E_{e^+} [MeV/c]
100	0.13944	4.78
120	0.16232	5.56
140	0.18400	6.31
160	0.20452	7.01
180	0.22369	7.67

Table 2.3: Position momentum as a function of the spectrometer current. Experimental calibration using the ^{90}Sr beta source with a corrected endpoint total energy at 2.515 MeV corresponding to 48 A (so-called Test 48A).

2.3.2 PosSi counter

At the exit of the spectrometer vacuum chamber, the positron yield was recorded by a Silicon counter (called PosSi) shown in Fig. 2.9. This Silicon counter was a $300\ \mu\text{m}$ single layer sensor covering the exit window of the vacuum chamber upstream of the reconversion target. To evaluate the spatial distribution of the positron flux, the PosSi counter was segmented into four pads (Fig. 2.12) and aligned accurately to the exit window. Its approximate sensitivity was 49.2 positrons/ADC count. The PosSi was a useful counter during the E-166 operations. Because of its geometry ($300\ \mu\text{m}$ Si wafer) and its proper placement in the setup, the PosSi counter was insensitive to the soft background and the positron signal/flux was clearly detectable when the undulator was ON. Table 2.4 shows the recorded positron signal in the PosSi counter for the undulator ON and OFF modes. 435 counts correspond to about 22000 positrons.

undulator	count	std. dev.
ON	435	15
OFF	0.7	1.1

Table 2.4: Recorded Signal (counts) in the PosSi counter for undulator ON and OFF (ON:Positron signal and OFF:background signal)

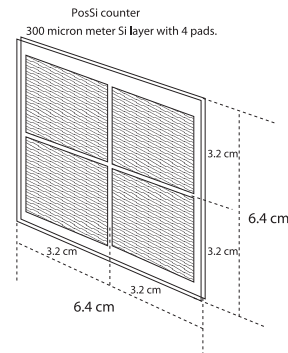


Figure 2.12: Scheme of the PosSi counter a $300\ \mu\text{m}$ silicon sensor with four pads.

After passing the PosSi counter, the positrons are reconverted to photons in a $0.5X_0$ tungsten target (see Fig. 2.7). These photons are then transmitted through a 75 mm thick magnetized iron (analyzing magnet) and finally recorded by the CsI(Tl) calorimeter (see Fig. 2.8).

2.4 The CsI(Tl) calorimeter

The CsI(Tl) calorimeter was one of the main contributions of the DESY Zeuthen and Humboldt University groups to the E-166 setup and was one of the central topic of this thesis. The calorimeter was a set of nine crystals assembled in a 3×3 array (Fig. 2.8, 2.19 and 2.18).

The CsI(Tl) crystals were supplied by Monokristal/Kharkov (Ukraine). CsI(Tl) crystal scintillators are well suitable for MeV-photon calorimetry. The light yield LY and its uniformity are important properties. A quality check of the nine crystals was performed measuring their light yield in terms of photoelectrons and its uniformity along the crystal axis. The relevant parameters for the CsI(Tl) crystals are summarized in Table 2.5.

Light readout

To read out the scintillation light of the CsI(Tl), with a peak emission wavelength at 550 nm, two options were tested. Two prototypes (one crystal each) were built with two different photosensitive detectors coupled to the crystals: a photomultiplier and a Hamamatsu S2744-08 photodiode module¹. In a test-beam at DESY in Hamburg the two prototypes were put in an electron beam line to study the response of the readout chain. The prototype with the photomultiplier has shown a saturation at high beam energies and a gray filter was required to attenuate the light to the photocathode. The Hamamatsu photodiodes with their large dynamic range had no limitations up to 7 GeV. After the test-beam, the photodiode option was chosen to build the final CsI(Tl) calorimeter for the E-166 experiment. The two prototypes were later used to monitor backgrounds in E-166.

The photodiode module is a pair of two independent PIN² diodes glued onto a polystyrene plate (1mm thick). The active area of each PIN diode is $10 \times 20 \text{ mm}^2$ and their thickness of $300 \text{ }\mu\text{m}$. The diodes were operated with a reverse bias voltage of -50V with the cathode grounded. Typical values were a dark current of 3 nA and a capacitance of 85 pF.

Crystal quality checking

The quality check consisted of measuring the light yield and its homogeneity along the crystal. For the light yield measurements, a ^{60}Co source with its two gamma lines at 1.173 MeV and 1.332 MeV was chosen.

¹The Hamamatsu S2744-08 photodiodes used in E-166 are of the same type used in the BaBar experiment.

²PIN stands for P-doped-Intrinsic-N-doped layered silicon structure.

For the homogeneity test, a dedicated setup was used. A ^{60}Co source with a lead collimator were mounted on a moving stage for a horizontal translation along the crystal axis. The CsI(Tl) crystal, the photodiode module and the preamplifier were placed in a light-tight copper box, which also provided electromagnetic shielding.

In the preamplifier, the signal from a single active PIN diode was first fed into a charge sensitive amplifier with gains 1 and gain 32. After the preamplifier, these two signals are called low gain (LG) and high gain (HG). They were fed into a driver board (called UMass board) to produce low impedance, bipolar signals for transmission from the detector to the counting house. The LG-HG correlation of the two photodiodes was measured to be linear with a slope of about $\frac{HG}{LG} = 30$ [Kovermann(2006)]. Before the digitization, the positive signals were inverted and added to the negative ones to give a double amplitude negative pulse to the ADC input. For digitization we used CAEN 8 channels charge integrating ADCs, model V265. For reversing and summing the bipolar signals we used a LeCroy linear FAN-in/FAN-out Model 428F which was for the actual experiment replaced by a dedicated amplifier.

The positions of the ^{60}Co source and collimator were optimized to illuminate a limited area of the crystal with a sufficient photon penetration depth. A step-size of 2 cm was chosen for the translation. To determine the double peak of the ^{60}Co , the photo-peak region was fit with a combination of two Gaussian distributions and the background was described by a polynomial convoluted with an exponential function:

$$f(x) = (ax^2 + bx + c).e^{-dx} + N \left(e^{-\frac{1}{2}\left(\frac{x-\mu}{\sigma}\right)^2} + e^{-\frac{1}{2}\left(\frac{x-\alpha\mu}{\sigma}\right)^2} \right) \quad (2.5)$$

with:

μ Gaussian mean value

$\alpha = \frac{1.332\text{MeV}}{1.173\text{MeV}}$ ratio of the position of the two peaks of the ^{60}Co source

A typical ^{60}Co spectrum recorded in the setup is shown in Fig. 2.14. To extract the photoelectron yield PY inducing the light collection efficiency, an absolute calibration of the ADC was required. It was calibrated in electric charge using an ^{241}Am source directly illuminating the photodiodes. The 59.5 keV photons of the Americium source, when absorbed in the silicon layer, create one electron-hole pair per 3.6 eV of deposited energy. The ^{241}Am photo-peak position was measured and was directly related to the number of created photoelectrons per ADC count. The photoelectron yield of both photodiodes was measured using the same readout electronic chain. A typical

spectrum of the ^{241}Am source is shown in Fig. 2.15. The photoelectron yield PY of a crystal coupled to the photodiode module given in [ph/MeV], can be determined by the ratio of the average ^{60}Co photo-peak position and ^{241}Am photo-peak position given by:

$$\text{PY}[\text{ph/MeV}] = \frac{\text{photo} - \text{peak}({}^{60}\text{Co}) \cdot 16527}{\text{photo} - \text{peak}({}^{241}\text{Am})} \quad (2.6)$$

The results of the quality check for the nine CsI(Tl) crystals are summarized in Fig. 2.16, which shows the measured photoelectron yield for different positions along the crystal axis. All nine crystals have average yields between 4000 and 5500 ph/MeV.

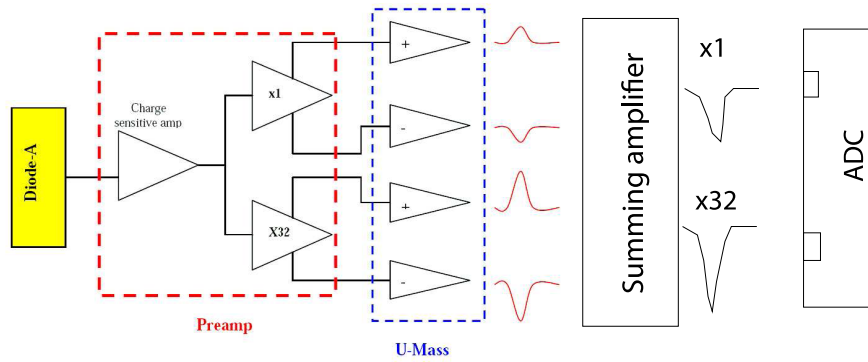


Figure 2.13: Scheme of the readout electronic chain: the Hamamatsu S2744-08 photodiode module, preamplifier, UMass board, summing amplifier and ADC

Mechanical assembly

The lateral cross section of the crystals was $60 \times 60 \text{ mm}^2$. The length was 280 mm, which corresponds to about 15 radiation length (Fig. 2.17). To increase the light collection, each crystal was wrapped with a white tyvek paper which provides diffuse reflections at the crystal surface. To avoid any cross-talk between the crystals, each one was in addition wrapped with a thin copper foil ($30 \mu\text{m}$) acting as an electromagnetic shield. The gain in light yield by adding additional tyvek layers is compromised by the increasing amount of dead material between crystals. Therefore, we have limited the crystal wrapping to two layers of tyvek which led to a total dead space of 1.2 mm. The crystals are stacked in a plastic frame inside a brass box with 6 mm wall thickness. The front wall, towards the analyzer magnet, is machined down to

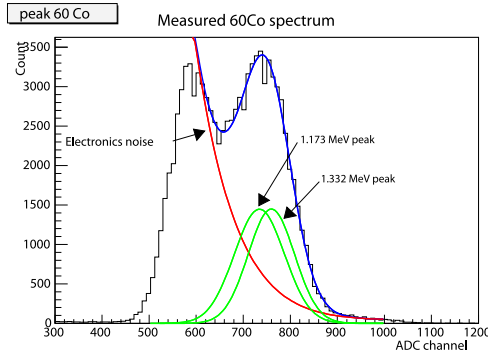


Figure 2.14: Energy spectrum of ^{60}Co measured by the CsI(Tl) crystal coupled to a Hamamatsu S2744-08 photodiode module.

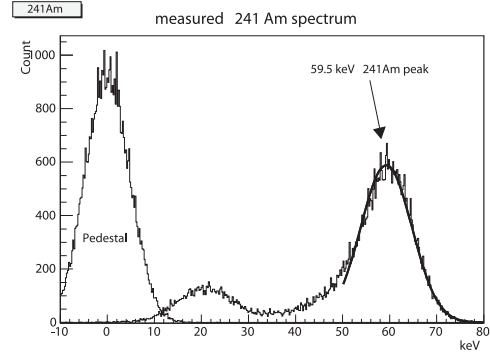


Figure 2.15: Calibrated spectrum of the ^{241}Am source illuminating the S2744-08 photodiode module

2 mm in the sensitive area. The box is light- but not air-tight empty spaces in the brass box were filled with desiccant.

Since the signal contributions of the different crystals in the array vary a lot, with the central crystal contributing about 40%, the crystals have been arranged according to there light yield. The best quality crystal was placed in the center (position 5), followed by the four next neighbors (positions 2, 4, 6, 8) and the edge crystals being the lowest quality (positions 1, 3, 7, 9) (see Fig. 2.19).

2.4.1 CsI(Tl) energy calibration at SLAC

The CsI(Tl) calorimeter was calibrated using cosmic muons and a ^{228}Th source with a gamma-peak at 2.8 MeV. For cosmic muons, the energy deposition per crystal was derived from a GEANT4-based simulation predicting 39.7 MeV deposited energy per crystal for muons passing vertically. The ^{228}Th source was placed on top of the calorimeter. The gamma-peak was clearly seen in crystals 7 and 8. It was well resolved from the noise (Fig. 2.23). For the data taking, a cosmic telescope was set on top of the CsI(Tl) calorimeter. This cosmic trigger was a coincidence of two identical plastic scintillator paddles (called C15 and C16) separated by a distance of 1 meter and covering the entire CsI(Tl) crystals (Fig. 2.20). We recorded events where muons were passing the calorimeter vertically with a small angular spread.

The readout electronic chain at SLAC was different from the test-setup used for the quality check. The calorimeter required 72 cables each 80 meter long connecting the bipolar signals from the FFTB tunnel to the counting

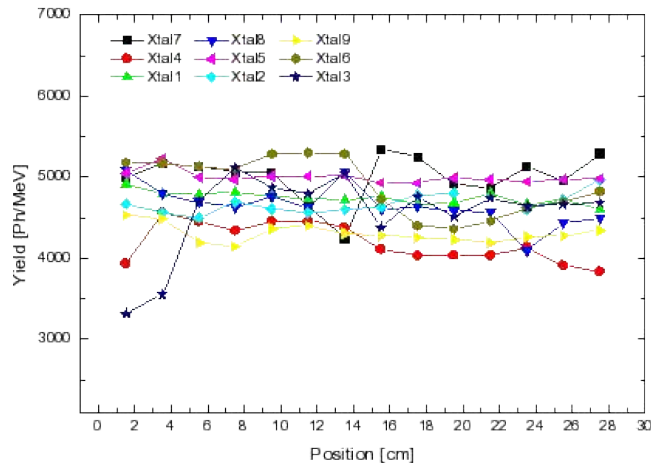


Figure 2.16: Photoelectron yield PY for the nine CsI(Tl) crystals in unit ph/MeV.

room. A dedicated summing-amplifier reduced the 72 channels to 18 channels after summing the bipolar signals for each crystal. Three CAEN V265 ADCs were reading the 18 channels in groups of 6. The data were recorded simultaneously in the low sensitivity LS (4 counts/pC) and in the high sensitivity HS (30 counts/pC) which is one of the features of the CAEN ADC V265. The signals from the CsI(Tl) calorimeter were written to disk in four resolution windows: LG-LS, LG-HS, HG-LS and HG-HS.

High statistics cosmic spectra were recorded and cleaned by some proper cuts. Only events were selected where muons fully pass through one column and no energy is deposited in the neighboring columns. In the nine crystals, the cosmic signal was well separated from the pedestal in both low gain and high gain. The calibration constants were derived from the individual crystal calibrations in the high sensitivity windows (see Table 2.6). The calibration constants of the low sensitivity window were calculated from the correlation between the two sensitivities (LS and HS) with a proportional factor of 0.133. Figure 2.21 shows the cosmic peaks in the nine crystals and Fig. 2.22 shows a cosmic peak fitted by exponential function combined with a Gaussian given by:

$$f(x) = \begin{cases} N e^{-\frac{1}{2}\left(\frac{x-\mu}{\sigma}\right)^2} & x < \mu + t \\ N e^{\frac{1}{\sigma^2}\left(\frac{t}{2} - (x-\mu)\right)} & x \geq \mu + t \end{cases} \quad (2.7)$$

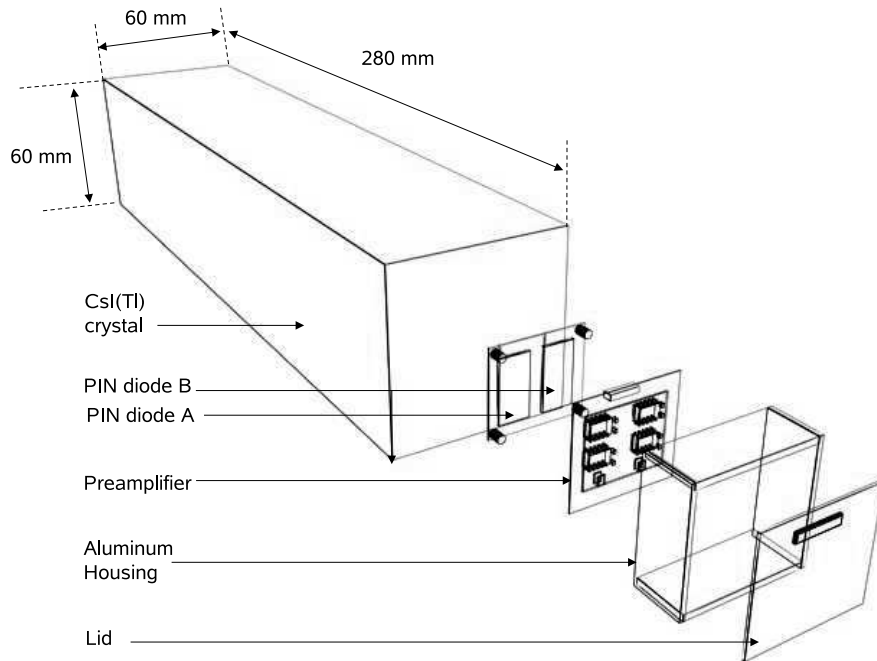


Figure 2.17: Back view of a single CsI(Tl) crystal coupled to a photodiode module.

where $(\mu + t)$ is the transition point from the Gaussian to the exponential decay.

By using the calibration constants, one can monitor the cosmic signal summed over the full calorimeter. The cosmic peak for the full calorimeter was about 120 MeV in the four resolution windows (HG-LS, HG-HS, LG-LS, and LG-HS). This value makes sense, since most of the muons see only three crystals and deposit 40 MeV in each.

This calibration procedure was performed with two high statistics cosmic muons spectra and ^{228}Th spectra before the E-166 data taking period. During the E-166 runs, the calibration constants were used to have an energy scale on the recorded positron signal and background.

A more accurate calibration procedure based on high statistics cosmic runs and pedestals accumulated over nine weeks is described in [Kovermann(2006)]. It was performed four months after the first calibration and has converged in a consistent way to the values obtained from the calibration procedure presented here. The agreement between the two calibrations gives confidence on the stability of the calorimeter response and its readout electronics.

Crystal Parameters	
material	CsI
Thelium	0.08 mol%
light yield	4000 to 5500 Ph/MeV
length	280 mm (15.11 X_0)
width	60 mm
height	60 mm
density	4.51 g/cm ³
radiation length	1.86 cm
molire radius	3.8 cm
decay time of the signal	1 μ s
peak emission wave length	550 nm

Table 2.5: Most relevant parameters of the CsI(Tl) crystals

Crystal number	1	2	3	4	5	6	7	8	9
HG-HS	0.02	0.03	0.03	0.08	0.03	0.03	0.04	0.04	0.04
HG-LS	0.21	0.23	0.26	0.65	0.24	0.23	0.35	0.33	0.32
LG-HS	0.24	0.26	0.34	0.40	0.23	0.29	0.38	0.43	0.49
LG-LS	1.85	2.01	2.55	3.04	1.73	2.19	2.86	3.28	3.70

Table 2.6: Calibration constants in [MeV/ADC] for low and high gain (LG and HG) output signals in both low and high sensitivity of the ADC (LS and HS).

2.5 Photon Diagnostics

The instrumentation on the photon table were mainly dedicated to the photon yield measurement and photon polarimetry. All the devices were accurately aligned along the undulator photon beam (Fig. 2.24 and 2.25).

2.5.1 Ag1SiC, Ag2SiC flux counters

The Ag1SiC and Ag2SiC were a set of identical counters which count undulator photons incident on and transmitted through the analyzing magnet. Each counter was composed of a 555 μ m (0.15 X_0) dens-alloy-170 tungsten converter, a 300 μ m silicon sensor and a 900 μ m G-10 support (Fig. 2.24). They were designed to give approximately equal signal per single photon in the energy range up to 10 MeV and thus to count undulator photons directly. For the E-166 undulator spectrum, the average sensitivity was approximately 4500 photons /ADC count. After calibration, these counters provided an ab-

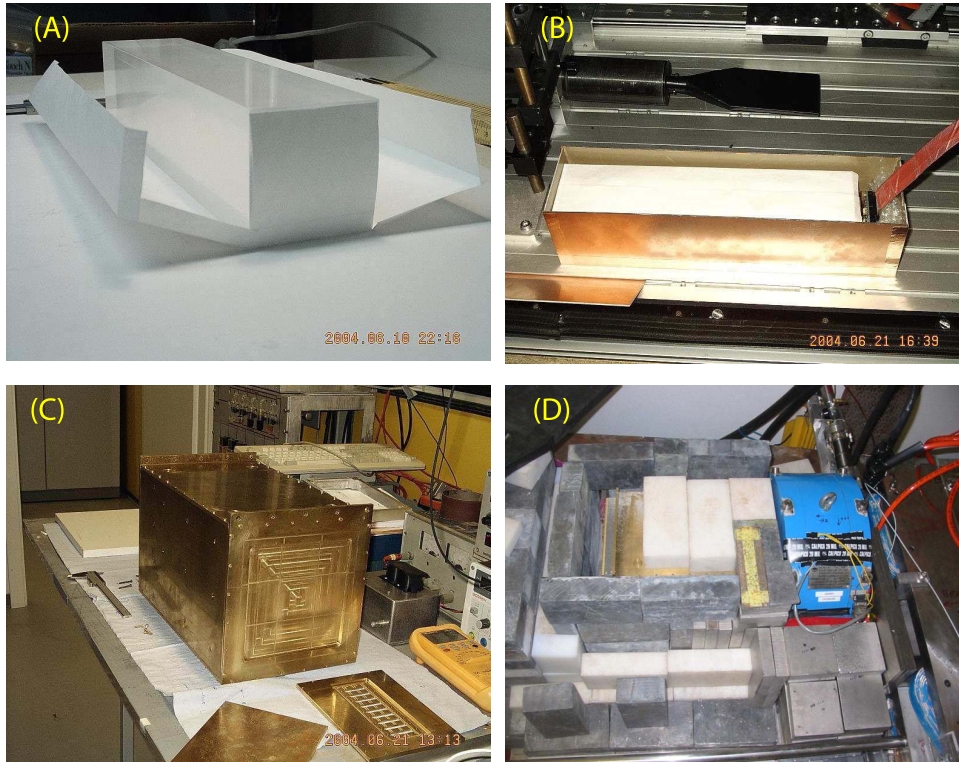


Figure 2.18: (A) CsI(Tl) crystal with tyvek wrapping. (B) Test setup for the quality check. (C) Brass housing for the nine CsI(Tl) crystals. (D) The CsI(Tl) calorimeter at SLAC surrounded by lead, and polyethylene shielding.

solute undulator photon intensity measurement for the experiment.

2.5.2 GCAL : silicon-tungsten calorimeter

GCAL was a sampling calorimeter with nine layers each consisting of 3.7 mm tungsten dens-alloy ($\approx 1 X_0$), 300 μm Silicon and 900 μm G-10, measuring the total energy of the transmitted photons (Fig. 2.24). One ADC count in GCAL corresponds to approximately 845 MeV deposited energy. The silicon sensors were segmented into 4×4 pads, each with an active area of $1.6 \times 1.6 \text{ cm}^2$.

2.5.3 Aero-gel flux counter

A complementary measurement of the incident and transmitted photon flux was made with a pair of Cerenkov counters using aero-gel with an index of

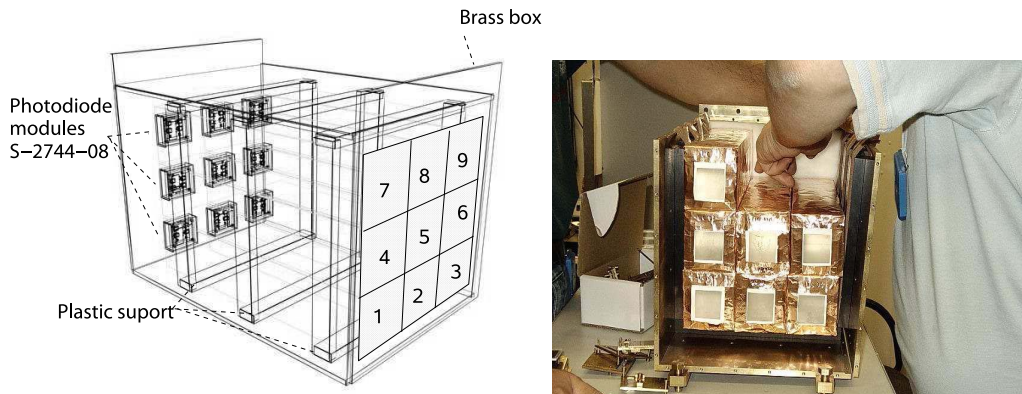


Figure 2.19: Front view (left) and back view picture (right) of the CsI(Tl) calorimeter. 3 x 3 CsI(Tl) crystal coupled to the readout electronics

refraction of $n = 1.009$ as radiator. This extremely low-index material was available from the BELLE experiment. The two counters are deployed before and after the photon analyzing magnet, as shown in Fig. 2.24 and 2.25. The signal in the aero-gel counter was generated by electrons and positrons from the conversion of undulator photons in the aluminum entrance window.

Electrons and positrons of energy larger than 4.3 MeV emit Cerenkov light. This light was guided by an optical system of mirrors and lenses in a light tight environment to a photomultiplier. Because of their threshold energy of 4.3 MeV, the aero-gel counters were insensitive to low energy radiation of the undulator photon beam. Hence, a pair of aero-gel counters that are placed upstream and downstream of the magnetized iron absorber, can confirm the attenuation of this absorber on photons of energy above 5 MeV, independent of possible backgrounds of lower-energy photons.

2.6 Background Detectors

Two background detectors were included in the setup. The placement of the background detectors is shown in Fig. 2.26. A single CsI(Tl) crystal was placed on the positron table inside the lead shielding. It was positioned on the top of the main electron beam pipe to monitor possible soft background generated by the 46.6 GeV electron beam passing below the positron table. A second detector (silicon detector called pCal) was mounted above the seven bending magnets which guide the electron beam to the FFTB dump. In its position, the pCal detects mainly positrons (and photons) generated by the electron beam close to the undulator table far upstream the diagnostic

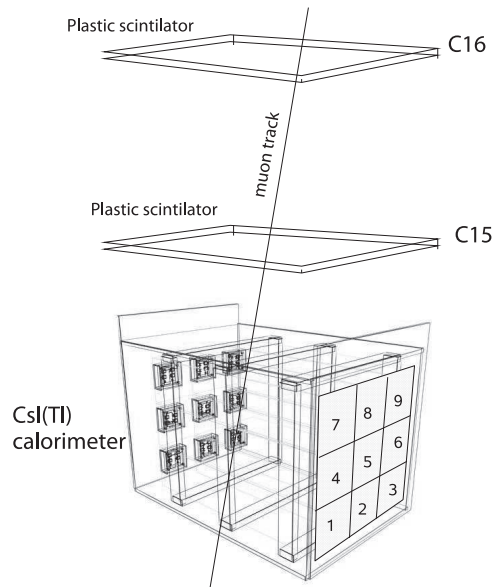


Figure 2.20: Perspective view of the CsI(Tl) calorimeter. 3 x 3 CsI(Tl) crystal with the cosmic trigger C15 and C16.

tables.

2.7 Tuning, operations and performance of the experiment

The E-166 experiment was operated over nine weeks in total, subdivided in two periods; 4 weeks in June 2005 and 5 weeks in September-October 2005.

The adopted experimental protocol can be summarized into seven steps:

- **Step 1:** Establish the gamma line using the OTR screen (2.27 bottom).
- **Step 2:** Send the electron beam through the undulator and align it to 100 % transmission and minimal background.
- **Step 3:** Power the undulator and record the signal of undulator photons.
- **Step 4:** Establish a particular trigger mode (undulator ON and OFF) to discriminate background from the signal in the data analysis.
- **Step 5:** Introduce the conversion target into the gamma line, and produce positrons.

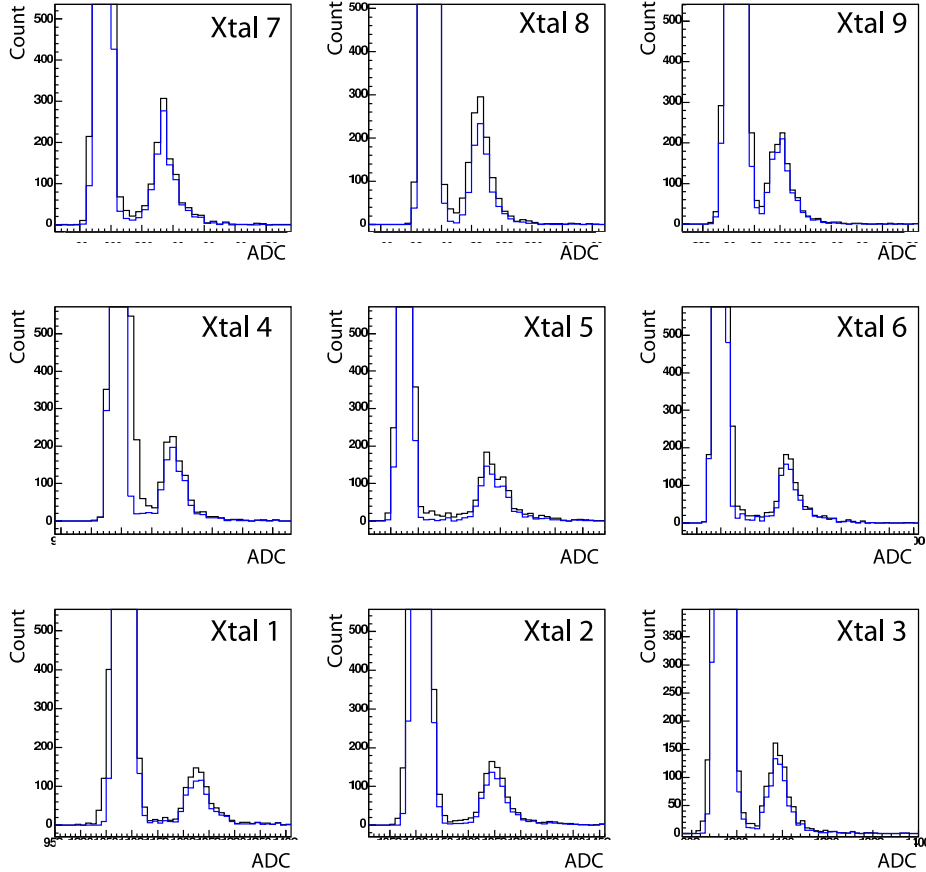


Figure 2.21: Cosmic spectra recorded in the nine crystals of the CsI(Tl) calorimeter.

- **Step 6:** Tune the transport system to get a positron signal in the PosSi counter and the CsI(Tl) calorimeter.
- **Step 7:** Record the photon transmission through the analyzing magnets for the undulator photons and for the positron at five momenta. The photon transmission must be recorded for the two opposite polarities of the analyzing magnet.

The photon line: The photon line is defined by the undulator and a tungsten collimator (named PC7.8) with a 3 mm aperture (see Fig. 2.2) with respect to the nominal electron beam line. To establish the gamma line, a 1 micron titanium foil (OTR) was inserted into the electron beam. In

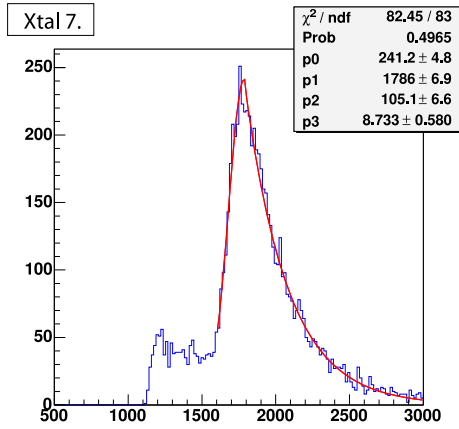


Figure 2.22: Cosmic muons spectrum recorded in crystal 7 and the corresponding fit.

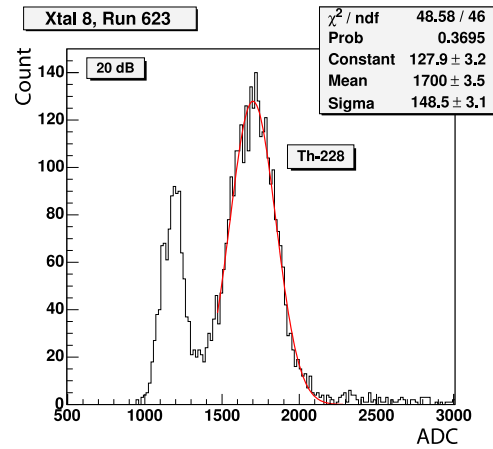


Figure 2.23: ^{28}Th source spectrum recorded in crystal number 8.

bypass mode³ the electron beam was steered using the two dipole magnets X6050 and B04A for X and Y corrections (Fig. 2.27) to guide the resulting photon beam through the collimator aperture (Fig. 2.2). During the steering procedure, the photon flux was recorded in the GCAL for different values of the X6050 and B04A magnetic field. Typical plots in Fig. 2.27 show the maximum transmission through the collimator with respect to magnetic field value of the steering dipoles.

The helical undulator: The undulator was then inserted and aligned, by a remote adjustment in position and angle, using the five stepping motors. During this delicate operation, the electron beam was monitored with a set of BPMs before and after the undulator and also with the help of a phosphor located at the entrance of the undulator (Fig. 2.3). The electrons passed through the 780 μm diameter of the one meter long undulator successfully with a transmission of 60 %. The transmission was then improved progressively to 100 % after several hours. After the alignment the undulator pulsed power supply was energized and a large photon signal was measured by the photon counters AG1SiC and AG2SiC (Fig. 2.28). The undulator trigger was adjusted in time to the electron bunch. To distinguish between background and signal, the undulator was triggered only every second electron bunch. Two trigger numbers were assigned to this configuration (Trig=36896

³The electron beam passing through the bypass pipe, rather than the undulator. See Fig. 2.27.

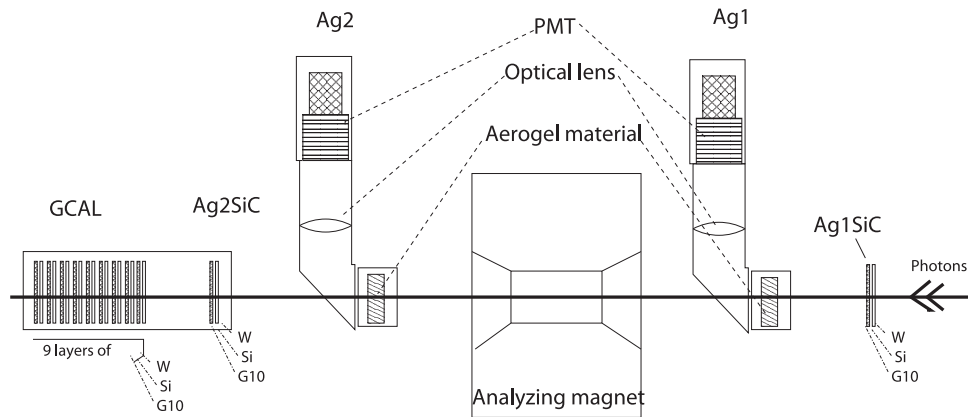


Figure 2.24: Scheme and components on the gamma table showing the silicon photon counters (Ag1SiC, Ag2SiC), the aero-gel counters (Ag1, Ag2), the SiW calorimeter (Gcal) and the photon analyzing magnet

and Trig=36864) for undulator OFF and ON, respectively. The undulator operation proved extremely reliable, with no down time over 9 weeks of operation during the experiment. It produced the expected photon intensity and showed the predicted quadratic dependence of the intensity on the undulator current.

The positron production target: The conversion target was inserted into the photon line and the first positron signal was recorded by the PosSi counter and the CsI(Tl) calorimeter (Fig. 2.29). The undulator ON and Off procedure was very useful for the CsI(Tl) calorimeter data analysis.

Data taking: The data taking had in general the following structure: For each spectrometer setting, a number of “*super-runs*” was taken. One *super-run* consists of 10 cycles with usually 3000 beam pulses. In an automatic procedure the polarity of the analyzer magnet for both the photon and the positron polarimeter was flipped simultaneously between each cycle. In the data sequential events are alternating “signal” and “background” events. Half of the events in one cycle are “background” events, i.e. the undulator was OFF at these beam pulses. The other half are “signal + background” events, which means the undulator was ON (Fig. 2.29).

From the operational point of view, the E-166 experiment was highly successful. All detectors and DAQ system have shown no down time over nine weeks operation and data taking. The operations were carried out in very close collaboration with the SLAC Main Control Center (MCC) operators



Figure 2.25: Picture of the gamma table showing the aero-gel counters (Ag1, Ag2) and the photon analyzing magnet

for beam steering and background reduction. The helical undulator fulfilled its task and provided an intense photon beam. The signal of the produced positrons was clearly seen above a well controlled background. The analyzing magnets were remotely controlled and flipped more than 2800 times without technical problems. In the data taking periods, the experiment has accumulated $9.7 \cdot 10^6$ beam pulses resulting in total of 15 GB of data on disk for offline analysis.

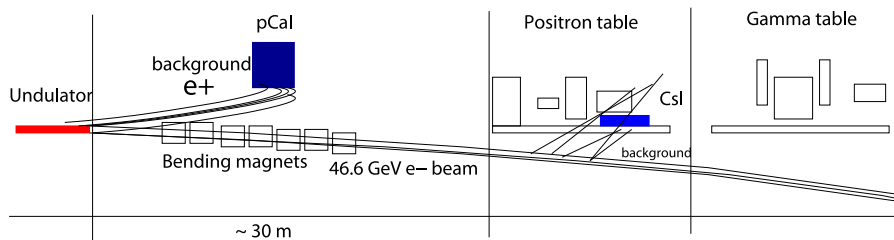


Figure 2.26: Scheme of the setup illustrating the position of the background detectors. The single CsI(Tl) crystal is on the positron table and the pCal detector is above the bending magnets.

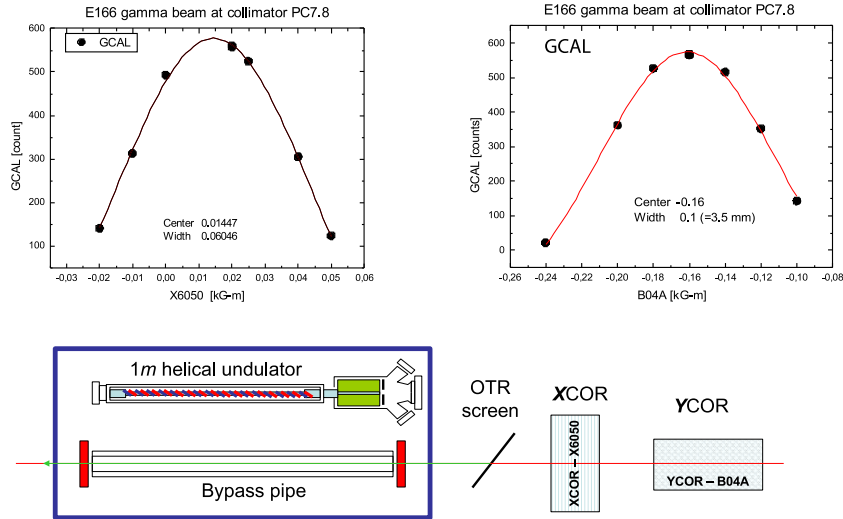


Figure 2.27: Top: Recorded photon signal in Gcal for X and Y steering of the electron beam using B04A and X6050. Bottom: Scheme of the the undulator table together with the magnets B04A and X6050 and the OTR screen (in this figure the electron beam comes from right to left).

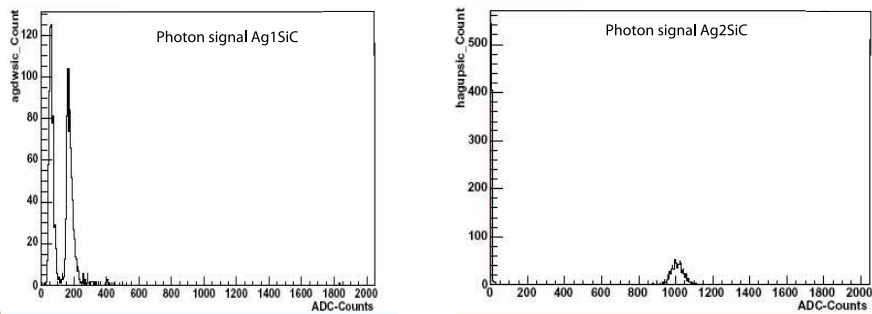


Figure 2.28: Recorded undulator photon signal in AG1SiC and AG2SiC

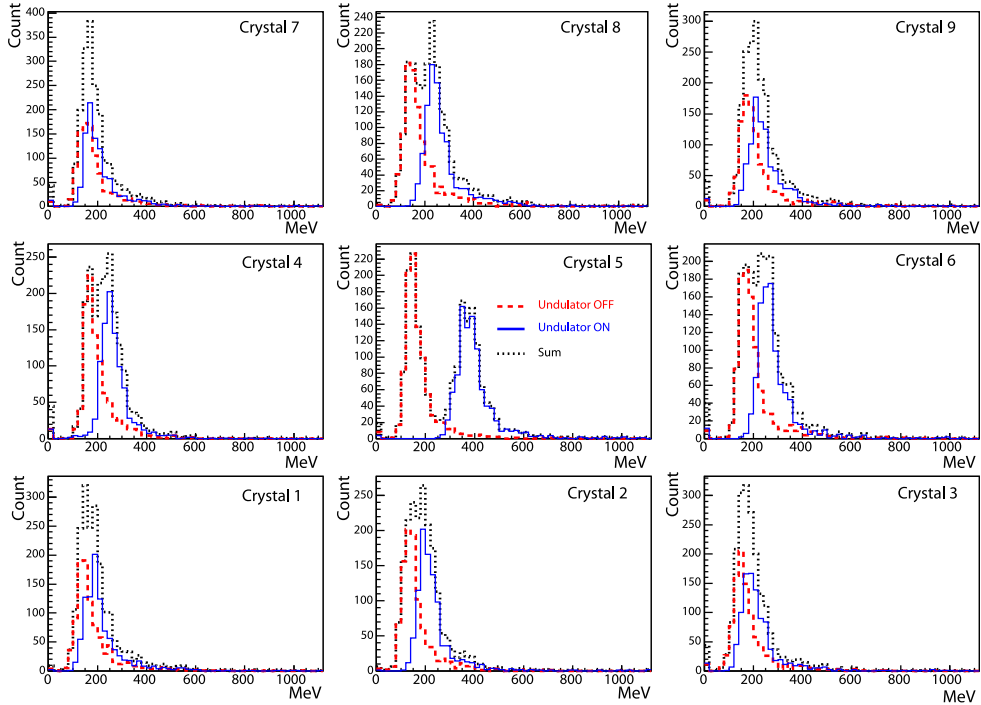


Figure 2.29: Recorded positron signal in the CsI(Tl) calorimeter in the nine crystals. In each crystal/histogram the background signal (undulator OFF) and positron signal (undulator ON) are visible. The background and the signal are much pronounced in the central crystal

Period in 2005	Number of weeks	spectrometer current in [A]	Run type	data [beam pulse]
June	4	150	e ⁺	2.1 10 ⁶
September	5	100	e ⁺	1.2 10 ⁶
		120	e ⁺	1.2 10 ⁶
		140	e ⁺	3.1 10 ⁶
		160	e ⁺	1.2 10 ⁶
		180	e ⁺	1.0 10 ⁶
		160	e ⁻	1.2 10 ⁶

Table 2.7: Statistics on the E-166 data

Chapter 3

Implementation of polarization in Geant4

Most Monte Carlo event generators take into account polarization effects in the initial and final state. These simulation tools were mainly developed for high energy physics experiments (LHC, SLC, ILC studies) including physics within and beyond the standard model. In addition to the event generators, which deliver the particle final state, another set of simulation tools treat the tracking of these elementary particles through the detectors and simulate the interaction of particles and detector response. Usually for a complete simulation study both tools –event generator and detector simulation– are needed. Widely used detector simulation are based on EGS (Electron Gamma Shower) [W. R. Nelson(1985)], GEANT3 [R. Brun(1985)] and GEANT4 [GEANT4(2003), GEANT4(2006)] (GEometry ANd Tracking) but none of these packages initially included polarization. In the last two decades many efforts were made to introduce polarization into these simulation tools.

The simulation tool which had the possibility to track the polarization state of particles in an electromagnetic interaction with matter has been developed in EGS by K. Flöttmann [Flöttmann(1993)] using the Stokes formalism to describe the particle polarization state.

For electron, positron and photon polarimetry, a second simulation tool has been developed by J.M. Hoogduin [Hoogduin(1997)] in GEANT3. This extension takes into account not only the polarization transfer but also the polarization dependence of the cross section in some electromagnetic processes. For the photon and positron polarimetry at the E-166 experiment, a preliminary simulation study was carried out by a polarized GEANT3 extension developed by V. Gharibian [G. Alexander(2003)]. In contrast to the EGS version with the polarization treatment, the two GEANT3 extensions

for particle polarization studies have not been published.

For the needs of detailed simulations within the EUROTeV frame and the E-166 experiment, a general framework of polarized electromagnetic processes in GEANT4 was crucial. It is described below.

We start first with the parameterization of polarization in the Stokes formalism then describe the basic formula for each process with some relevant results from this new extension in GEANT4. The new implementation with a general treatment of polarization (linear, longitudinal/circular) in terms of polarization transfer and cross sections was first initiated by A. Stahl early 2004 and then lead by A. Schällicke [R. Dollan and Schällicke(2006)]. This development was done within the DESY and HU (The Humboldt University in Berlin) E-166/EUROTEV groups with a close collaboration with P. Starovoitov (NCPHEP, Minsk). Within this thesis, our main contribution was focused on three processes: Bremsstrahlung, gamma conversion and photoelectric effect. The first version of the new extension has been proposed to the GEANT4 collaboration and was officially included in the public GEANT 4.8.2 release in December 2006 [GEANT4(2007)].

3.1 Polarization

In electrodynamics, polarization is an important property of electromagnetic waves, such as light. It describes the oscillations of their transverse electric field. More generally, the polarization of a transverse wave describes the preference for an oscillation direction in the plane perpendicular to the direction of propagation. Conventionally we only refer to the electric field vector. In the most general case for a plane-wave satisfying the Maxwell equations and propagating in z-direction in an isotropic medium the electric field \vec{E} can be written as:

$$\vec{E}(\vec{r}, t) = \begin{pmatrix} E_x \\ E_y \\ 0 \end{pmatrix} e^{i(kz - \omega t)} \quad (3.1)$$

- \vec{k} The wave vector pointing to the direction of propagation
- $\omega = kv$ The frequency
- $v = \frac{c}{n}$ The velocity of the wave in a medium characterized by a refractive index n

For a simple plane wave propagating in \vec{k} direction parallel to z, the x and y components of the electric field have exactly the same frequency ω . However, these components have two other defining characteristics that

may differ. First, the two components may not have the same amplitude. Second, the two components may not have the same phase. The electric field oscillation onto the x-y plane describes in the most general case an ellipse (Fig. 3.1).

3.2 Parameterization of Polarization

3.2.1 The Jones vector

Starting from an elliptical polarization state, a common parameterization uses the azimuthal angle Ψ and the ellipticity ε defined by $\tan \chi = \varepsilon$ (see Fig. 3.1). The polarization information of any wave can be fully contained in the amplitude and relative phase of oscillations of two components of the electric field vector \vec{E} expressed by the complex coefficients a_1 and a_2 :

$$\vec{a} = \begin{pmatrix} a_1 \\ a_2 \end{pmatrix} \quad (3.2)$$

so that equation 3.1 can be written as:

$$\vec{E}(\vec{r}, t) = E_0 \begin{pmatrix} a_1 \\ a_2 \\ 0 \end{pmatrix} e^{i(kz - \omega t)} \quad (3.3)$$

with $|a_1|^2 + |a_2|^2 = 1$ and E_0 the real amplitude of the electric field.

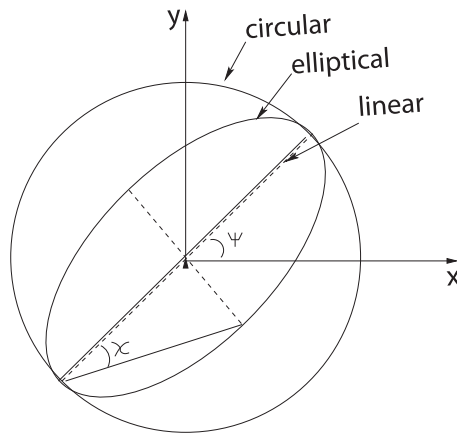


Figure 3.1: Trajectory drawn by the electric field vector in the X-Y plan.

From this general elliptical polarization concept two practical cases can be derived. First, an ellipticity of zero means that a_1 and a_2 are in phase and

corresponds to linear polarization. Second, an ellipticity of 1 means a phase difference of $\frac{\pi}{2}$ between a_1 and a_2 and corresponds to a circular polarization if $|a_1| = |a_2|$ (elliptical polarization if $|a_1| \neq |a_2|$). So one can write the amplitude and phase information in a convenient form represented as a two-dimensional complex vector called the Jones vector \vec{a} given by Eq. 3.2.

3.2.2 Stokes parameters from Jones Vector

In the case of partially polarized radiation, the Jones vector varies in time and space. In this case, only statistical information can be gathered about the variations and correlations between components of the electric field. In contrast to the Jones representation, where the polarization information is related to the amplitude and the phase difference, in 1852 George Gabriel Stokes [McMaster(1961)], introduced a new concept of representing all possible polarization states of a wave in terms of four independent parameters that depend only on the amplitude (intensity I). The Stokes parameters were initially formulated to study the polarization of visible light. This mathematical approach was then extended to describe the polarization state of any electromagnetic radiation and elementary spin- $\frac{1}{2}$ particles like electrons and positrons.

By introducing an orthogonal right-handed coordinate system in which the wave is traveling in the positive z-direction, the Stokes parameters can be defined as:

I_0	Total intensity of the wave
$\zeta_1 = \frac{I_x - I_y}{I_0}$	The degree of linear polarization with respect to the x and y axis.
$\zeta_2 = \frac{I_{45} - I_{135}}{I_0}$	The degree of linear polarization with respect to the axes oriented at 45° to the right of the previous x- and y-axis
$\zeta_3 = \frac{I_l - I_r}{I_0}$	The degree of circular polarization. I_l and I_r are the left and right intensities of circular polarization respectively.

In terms of the Jones Vector, the Stokes parameters can be written by use of the unit matrix σ_0 and the Pauli matrices as follow:

$$I_0 = a_1^* a_1 + a_2^* a_2 = \vec{a}^\dagger \sigma_0 \vec{a} \quad (3.4)$$

$$\zeta_1 = (a_1^* a_1 - a_2^* a_2) / I_0 = (\vec{a}^\dagger \sigma_1 \vec{a}) / I_0 \quad (3.5)$$

$$\zeta_2 = (a_1^* a_2 + a_2^* a_1) / I_0 = (\vec{a}^\dagger \sigma_2 \vec{a}) / I_0 \quad (3.6)$$

$$\zeta_3 = -i(a_1^* a_2 - a_2^* a_1) / I_0 = (\vec{a}^\dagger \sigma_3 \vec{a}) / I_0 \quad (3.7)$$

Where:

$$\sigma_0 = \begin{pmatrix} 1 & 0 \\ 0 & 1 \end{pmatrix} \quad \sigma_1 = \begin{pmatrix} 1 & 0 \\ 0 & -1 \end{pmatrix} \quad \sigma_2 = \begin{pmatrix} 0 & 1 \\ 1 & 0 \end{pmatrix} \quad \sigma_3 = \begin{pmatrix} 0 & -i \\ i & 0 \end{pmatrix}$$

In a more compact form -for a single particle- the Stokes parameters can be written as a four vector known as a Stokes vector.

$$\begin{pmatrix} I_0 \\ \zeta \\ \tilde{\zeta} \end{pmatrix} = \begin{pmatrix} I_0 \\ \zeta_1 \\ \zeta_2 \\ \zeta_3 \end{pmatrix}, \quad (3.8)$$

For single, 100% polarized particle it fulfills the condition:

$$\zeta_1^2 + \zeta_2^2 + \zeta_3^2 = 1 \quad (3.9)$$

In the Stokes formalism, only three parameters (real numbers) are sufficient to fully characterize the polarization state of any electromagnetic wave as well as circular and linear polarization for single photons and polarization of a single electron or positron. The Stokes vector can be extended from the description of single particle polarization to a description of beam polarization in the sense that it defines a mean polarization. In this context Eq. 3.9 becomes an inequality.

3.2.3 Transfer matrix

When a particle undergoes an electromagnetic process, the initial polarization state is transformed in a convenient way into a new set of parameters using the transformation matrix introduced by McMaster [McMaster(1961)]. The polarization transfer from the initial state ($\vec{\zeta}$) to one final state particle ($\vec{\xi}$) and the differential cross section are combined in a 4×4 interaction matrix T characterizing the interaction. In general the interaction matrix T depends on the kinematical variables and the polarized cross section if both initial particle and target particle are polarized. In this framework the general mathematical formulation of the interaction matrix T has the form given by:

$$T = \begin{pmatrix} S & A_1 & A_2 & A_3 \\ P_1 & M_{11} & M_{21} & M_{31} \\ P_2 & M_{12} & M_{22} & M_{32} \\ P_3 & M_{13} & M_{23} & M_{33} \end{pmatrix}. \quad (3.10)$$

with

S	Unpolarized differential cross section
A_j	differential cross section dependent on polarization
P_i	(De)polarization effects
M_{ij}	Polarization transfer to secondaries

Using the full matrix, all polarization effects are taken into account. When an initial particle interacts through an electromagnetic process, the final state polarization can be obtained by applying the interaction matrix to the initial state polarization. One can write:

$$\begin{pmatrix} I \\ \vec{\xi}^{(1)} \end{pmatrix} = T \begin{pmatrix} I_0 \\ \vec{\zeta}^{(1)} \end{pmatrix}, \quad (3.11)$$

where.

I_0	Intensity of the incoming beam
I	Intensity of the outgoing beam
$\vec{\zeta}^{(1)}$ and $\vec{\xi}^{(1)}$	Stokes vectors of the initial and final state particles, respectively. The exponent (1) stands for the primary particle.

Similarly, if secondaries are produced in a interaction one can define a matrix characterizing the polarization transfer to those secondaries. One can write:

$$\begin{pmatrix} I' \\ \vec{\xi}^{(2)} \end{pmatrix} = T' \begin{pmatrix} I_0 \\ \vec{\zeta}^{(1)} \end{pmatrix}. \quad (3.12)$$

where.

I_0	Intensity of the incoming beam
I'	Intensity of the outgoing secondary beam
$\vec{\zeta}^{(1)}$ and $\vec{\xi}^{(2)}$	Stokes parameters of the incoming and the secondary particle polarization state, respectively. The exponents (1) and (2) stand for the primary particle and a produced secondary particle respectively.

3.3 Polarization in GEANT4.

3.3.1 GEANT4

GEANT4¹ is a powerful (object oriented C++ based) package that simulates the passage (interactions) of particles through the matter taking into

¹GEometry ANd Tracking version 4.xx

account interactions of particles with matter. Originally designed for high energy physics experiments, it has found applications outside this domain in areas such as medical physics, biological sciences, radio-protection, and astroparticle physics. The principal features of GEANT4 are the transportation of particles (tracking) through an experimental setup, the simulation of the detector response and the graphical representation of the setup and of the particle trajectories. A powerful interactive mode is also available. Visualization provides a very useful tool for debugging and optimization of the setup. GEANT4 allows to:

- describe an experimental setup by a structure of geometrical volumes,
- assign a medium (material) to each volume,
- include a list of the interaction processes considered (known as physics-list),
- track particles through the various regions of the setup, taking into account geometrical volume boundaries and physical effects according to the nature of the particles themselves,
- track particles through electric and magnetic fields,
- record particle trajectories and the response of the sensitive detectors,
- visualize the detectors and the particle trajectories.

The implementation of effects of particle polarization was always envisioned in GEANT4. A platform was defined, as a basis of the polarization tracking and also the spin precession in a magnetic field. This initial platform made for particle polarization was implemented in such a way to facilitate any further development and improvement of the GEANT4 toolkit. For the electromagnetic processes, only the low energy Compton scattering by linearly polarized gamma rays (low energy processes extension) was implemented in the *G4LowEnergyPolarizedComptonScattering* class. The authors of these implementation are G.Depaola, F.Longo, A.Zoglauer and V.Ivanchenko [Depaola(2003)]. Due to these first efforts, the particle polarization vector and the necessary methods *SetParticlePolarization* and *GetParticlePolarization* are already existing as members of the *G4ParticleGun* and *G4GeneralParticleSource* classes. Moreover, these two methods are not only set for the primary particle generator but they also allow to Get(Set) the polarization vector of any elementary particle at any step during the tracking.

A new polarization manager has been developed which enables the user to define in GEANT4 a material volume with an averaged polarization of the electrons (in the atomic shells) [Schälicke(2006), GEANT4(2007)]. This is needed mainly for polarimetry applications.

In our approach, we have taken advantage of the existing platform and we have developed an extension of polarized EM processes to the toolkit which has a full treatment of polarization states using the Stokes formalism. In the development of the new extension we focused on studying the polarization of three elementary particles: photons, electrons and positrons.

3.3.2 Polarized processes in GEANT4

For the polarization treatment, one can sort the electromagnetic processes in two different categories. In the first set, only the polarization transfer to secondary particles is taken into account. This is the case for gamma conversion and bremsstrahlung processes. In these two processes, the interaction occurs in the field of a nucleus which is assumed to be unpolarized. The second set includes Compton scattering, ionization (Bhabha and Møller scattering), positron annihilation and photoelectric effect. These processes, are described as two body interactions. In addition to the polarization transfer, the differential cross section itself depends on both the incoming particle and the target particle polarization. Also the depolarization of the initial particle is taken into account in the cases where the initial particle does not vanish to produce secondaries. Table 3.1 summarizes and sorts all processes in terms of polarization dependence of the cross section, polarization transfer to secondaries and depolarization effects. Table 3.2 defines the Stokes parameter nomenclature for photons, electrons and positrons in the particle reference frame.

Incoming Particle type	Process Name	Class Name	Pol-Transfer to secondaries	Depolarization	Target particle may be polarized
Photon	Gamma conversion	G4PolarizedGammaConversion	Yes	-	No
	Photoelectric effect	G4PolarizedPhotoelectricEffect	Yes	-	Yes
	Compton scattering	G4PolarizedComptonScattering	Yes	Yes	Yes
Electron	Bremsstrahlung	G4ePolarizedBremsstrahlung	Yes	Yes	No
	Ionization (Møller)	G4ePolarizedIonisation	Yes	Yes	Yes
Positron	Bremsstrahlung	G4ePolarizedBremsstrahlung	Yes	Yes	No
	Ionization (Bhabha)	G4ePolarizedIonisation	Yes	Yes	Yes
	Annihilation	G4eplusPolarizedAnnihilation	Yes	-	Yes

Table 3.1: Processes and Class name of the polarized processes in GEANT4 sorted for Photons, electron and positrons

	Photons	Electrons/Positrons
ζ_1	linear polarization	polarization in x direction
ζ_2	linear polarization but $\pi/4$ to right	polarization in y direction
ζ_3	circular polarization	polarization in z direction

Table 3.2: Stokes parameters for photons, electrons and positrons moving in the positive z direction (the particle reference plane)

3.4 Gamma Conversion and Bremsstrahlung

The gamma conversion process (also known as pair production) is the creation of a particle and its antiparticle, from a photon. This is possible if the primary photon carries energy above a threshold, the total rest mass of the two particles and the situation allows to conserve both energy and momentum. The gamma conversion process occurs when a high-energy photon interacts with the field of an atomic nucleus, allowing to produce an electron and a positron without violating conservation of momentum.

Bremsstrahlung is an electromagnetic radiation produced by the deceleration (acceleration) of a charged particle, such as an electron or positron. Bremsstrahlung radiation has a continuous spectrum.

Gamma conversion and bremsstrahlung are cross-symmetric processes (i.e. the Feynman diagram for electron bremsstrahlung can be obtained from the gamma conversion diagram by flipping the incoming photon and outgoing positron lines) and their cross sections are closely related. For both processes, the interaction occurs in the field of the nucleus and the total and differential cross section are polarization independent. Only the polarization transfer from the incoming particle to the outgoing particles is taken into account, but not to the nucleus. Gamma conversion and bremsstrahlung in the field of atomic electrons has a much lower cross section and is negligible.

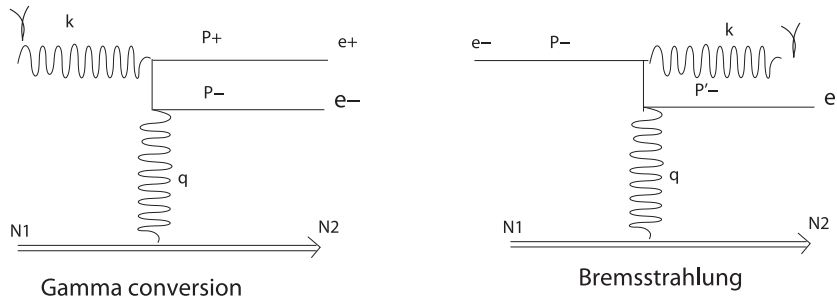


Figure 3.2: Feynman diagrams of gamma conversion and bremsstrahlung processes.

Since the gamma conversion and bremsstrahlung processes occur in the field of a nucleus, which is assumed to be unpolarized, the cross sections, energy loss and mean free path of explicitly generated final state particles can be treated by the generic unpolarized Geant4 classes *G4eBremsstrahlung* and *G4GammaConversion*.

The remaining task is to attribute polarization vectors to the final state particles generated, which is discussed in the following.

3.5 Polarized Bremsstrahlung for Electron and Positron

3.5.1 Polarization transfer from the lepton $e^- (e^+)$ to a photon

This section describes the basic formulas of polarization transfer and depolarization effects in the G_4e Polarized Bremsstrahlung class. The polarization transfer from an electron (positron) to a photon in a bremsstrahlung process was calculated by Olsen and Maximon [Olsen and Maximon(1959)], taking into account both Coulomb and screening effects. In the Stokes formalism, the $e^- (e^+)$ polarization is transferred to a photon finale state through an interaction matrix T_γ^b . For the polarization transfer one can write:

$$\begin{pmatrix} I \\ \vec{\xi}^{(2)} \end{pmatrix} = T_\gamma^b \begin{pmatrix} I_0 \\ \vec{\zeta}^{(1)} \end{pmatrix}. \quad (3.13)$$

The interaction matrix is given by

$$T_\gamma^b = \begin{pmatrix} 1 & 0 & 0 & 0 \\ D & 0 & 0 & 0 \\ 0 & 0 & 0 & 0 \\ 0 & T & 0 & L \end{pmatrix}, \quad (3.14)$$

$$I = (\epsilon_1^2 + \epsilon_2^2)(3 + 2\Gamma) - 2\epsilon_1\epsilon_2(1 + 4u^2\hat{\xi}^2\Gamma) \quad (3.15)$$

$$D = \{8\epsilon_1\epsilon_2u^2\hat{\xi}^2\Gamma\} / I \quad (3.16)$$

$$T = \{-4k\epsilon_2\hat{\xi}(1 - 2\hat{\xi})u\Gamma\} / I \quad (3.17)$$

$$L = k\{(\epsilon_1^2 + \epsilon_2^2)(3 + 2\Gamma) - 2\epsilon_2(1 + 4u^2\hat{\xi}^2\Gamma)\} / I \quad (3.18)$$

and

- ϵ_1 total energy of the incoming lepton $e^+ (e^-)$ in units $m_e c^2$
- ϵ_2 total energy of the outgoing lepton $e^+ (e^-)$ in units $m_e c^2$
- \vec{p} electron (positron) initial momentum in units $m_e c$
- \vec{k} bremsstrahlung photon momentum in units $m_e c$
- \vec{u} component of \vec{p} perpendicular to \vec{k} in units $m_e c$ and $u = |\vec{u}|$
- $k = (\epsilon_1 - \epsilon_2)$, the energy of the bremsstrahlung photon in units of $m_e c^2$
- $\hat{\xi} = 1/(1 + u^2)$

Coulomb and screening effects are contained in Γ , defined by:

$$\Gamma = \ln\left(\frac{1}{\delta}\right) - 2 - f(Z) + \mathcal{F}\left(\frac{\hat{\xi}}{\delta}\right) \quad \text{for } \Delta \leq 120 \quad (3.19)$$

$$\Gamma = \ln\left(\frac{111}{\hat{\xi}Z^{\frac{1}{3}}}\right) - 2 - f(Z) \quad \text{for } \Delta \geq 120 \quad (3.20)$$

with

$$\Delta = \frac{12Z^{\frac{1}{3}}\epsilon_1\epsilon_2\hat{\xi}}{121k} \quad \text{with } Z \text{ the atomic number and } \delta = \frac{k}{2\epsilon_1\epsilon_2} \quad (3.21)$$

$f(Z)$ is the coulomb correction term derived by Davies, Bethe and Maximon [H. Davies(1954)]. $\mathcal{F}(\hat{\xi}/\delta)$ contains the screening effects and is zero for $\Delta \leq 0.5$ (no screening effects). For $0.5 \leq \Delta \leq 120$ (intermediate screening) it is a slowly decreasing function. The $\mathcal{F}(\hat{\xi}/\delta)$ values versus Δ are given in Table 3.3. Intermediate values are interpolated.

The polarization vector of the incoming e^- (e^+) must be rotated into the frame defined by the scattering plane (x-z-plane) and the direction of the outgoing photon (z-axis). The resulting polarization vector of the bremsstrahlung photon is also given in this frame. Using Eq. (3.13) and the transfer ma-

Δ	$-\mathcal{F}\left(\frac{\hat{\xi}}{\delta}\right)$	Δ	$-\mathcal{F}\left(\frac{\hat{\xi}}{\delta}\right)$
0.5	0.0145	40.0	2.00
1.0	0.0490	45.0	2.114
2.0	0.1400	50.0	2.216
4.0	0.3312	60.0	2.393
8.0	0.6758	70.0	2.545
15.0	1.126	80.0	2.676
20.0	1.367	90.0	2.793
25.0	1.564	100.0	2.897
30.0	1.731	120.0	3.078
35.0	1.875		

Table 3.3: $\mathcal{F}(\hat{\xi}/\delta)$ for intermediate values of the screening factor [H. W. Koch(1959)]

trix given by Eq. (3.14) the bremsstrahlung photon polarization state in the

Stokes formalism [McMaster.(1954), McMaster.(1961)] is given by

$$\vec{\xi}^{(2)} = \begin{pmatrix} \xi_1^{(2)} \\ \xi_2^{(2)} \\ \xi_3^{(2)} \end{pmatrix} = \begin{pmatrix} D \\ 0 \\ \zeta_1^{(1)}L + \zeta_2^{(1)}T \end{pmatrix} \quad (3.22)$$

3.5.2 Lepton depolarization

The $e^- (e^+)$ polarization after emitting a bremsstrahlung photon can be calculated using the interaction matrix T_l^b which describes the lepton depolarization. This transfer matrix describing the depolarization effects for the outgoing $e^- (e^+)$ was not given by Olsen and Maximon. It can be calculated from the transfer matrix given in [Flöttmann(1993), Hoogduin(1997)]. For the polarization transfer one can write:

$$\begin{pmatrix} I' \\ \vec{\xi}^{(1)} \end{pmatrix} = T_l^b \begin{pmatrix} I_0 \\ \vec{\xi}^{(1)} \end{pmatrix} \quad (3.23)$$

And the interaction matrix is given by:

$$T_l^b = \begin{pmatrix} 1 & 0 & 0 & 0 \\ D & M & 0 & E \\ 0 & 0 & M & 0 \\ 0 & F & 0 & M + P \end{pmatrix} \quad (3.24)$$

where

$$I = (\epsilon_1^2 + \epsilon_2^2)(3 + 2\Gamma) - 2\epsilon_1\epsilon_2(1 + 4u^2\hat{\xi}^2\Gamma) \quad (3.25)$$

$$F = \epsilon_2 \{4k\hat{\xi}u(1 - 2\hat{\xi})\Gamma\} / I \quad (3.26)$$

$$E = \epsilon_1 \{4k\hat{\xi}u(2\hat{\xi} - 1)\Gamma\} / I \quad (3.27)$$

$$M = \{4k\epsilon_1\epsilon_2(1 + \Gamma - 2u^2\hat{\xi}^2\Gamma)\} / I \quad (3.28)$$

$$P = \{k^2(1 + 8\Gamma(\hat{\xi} - 0.5)^2)\} / I \quad (3.29)$$

with

- ϵ_1 total energy of the incoming e^+/e^- in units $m_e c^2$
- ϵ_2 total energy of the outgoing e^+/e^- in units $m_e c^2$
- \vec{p} electron (positron) initial momentum in units $m_e c$
- \vec{k} photon momentum in units $m_e c$
- \vec{u} component of \vec{p} perpendicular to \vec{k} in units $m_e c$ and $u = |\vec{u}|$
- $k = (\epsilon_1 - \epsilon_2)$, energy of the photon in units of $m_e c^2$
- $\hat{\xi} = 1/(1 + u^2)$

Using Eq. 3.23 and the transfer matrix given by Eq. 3.24 the e^- (e^+) polarization state after emitting a bremsstrahlung photon is given in the Stokes formalism by

$$\vec{\xi}^{(1)} = \begin{pmatrix} \xi_1^{(1)} \\ \xi_2^{(1)} \\ \xi_3^{(1)} \end{pmatrix} = \begin{pmatrix} \zeta_1^{(1)} M + \zeta_3^{(1)} E \\ \zeta_2^{(1)} M \\ \zeta_3^{(1)} (M + P) + \zeta_1^{(1)} F \end{pmatrix}. \quad (3.30)$$

3.5.3 Simulation

Figure 3.3 shows the polarization transfer in the bremsstrahlung process. The high energy bremsstrahlung photons inherit the positron (electron) polarization. Fig. 3.4 describe the positron (electron) depolarization after emitting a bremsstrahlung photon. One can notice that if the positron (electron) loses 50% of its energy via the bremsstrahlung process it is still about 80% polarized. This plot shows 100% polarized e^+ beam of 5 MeV passing through a 0.2 X_0 tungsten target with bremsstrahlung the only process considered.

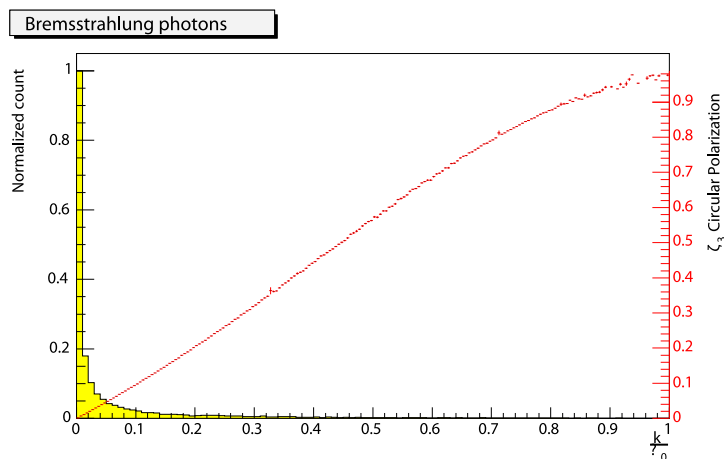


Figure 3.3: Normalized energy distribution (*left axis, histogram*) and degree of circular polarization (*right axis, curve*) of bremsstrahlung photons (polarization transfer) versus the fractional kinetic energy $\frac{k}{\epsilon_0}$ where k is the photon energy and ϵ_0 the initial electron kinetic energy.

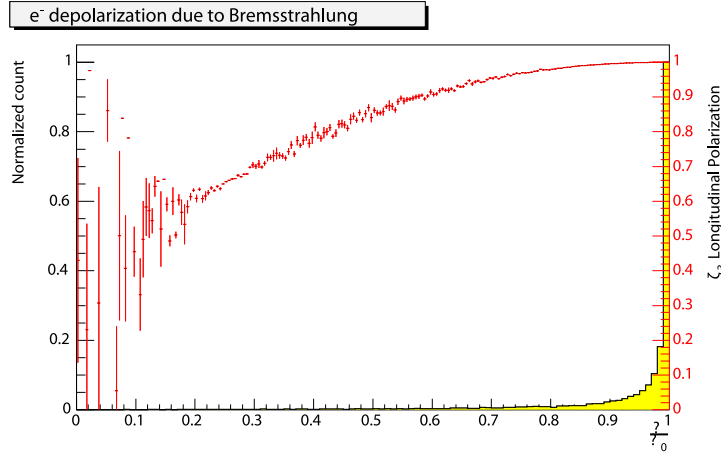


Figure 3.4: Normalized energy distribution (left axis, histogram) and Degree of longitudinal polarization (depolarization effect) (points with error bars, scale on the right) of positrons (electrons) emitting bremsstrahlung photons versus $\frac{\epsilon}{\epsilon_0}$ where ϵ is the electron kinetic energy after the bremsstrahlung process and ϵ_0 the initial electron kinetic energy.

3.6 Polarized Gamma Conversion

3.6.1 Polarization transfer from the photon to the two leptons

This section describes the basic formulas of polarization transfer implemented in the `G4PolarizedGammaConversion` class. Gamma conversion is essentially the inverse process of bremsstrahlung and the interaction matrix is obtained by inverting the rows and columns of the bremsstrahlung matrix and changing the sign of ϵ_2 described in section 3.5. It follows from the work by Olsen and Maximon [Olsen and Maximon(1959)] that the polarization state $\vec{\xi}^{(1)}$ of a positron (electron) after pair production is obtained by:

$$\begin{pmatrix} I' \\ \vec{\xi}^{(1)} \end{pmatrix} = T_l^b \begin{pmatrix} I_0 \\ \vec{\zeta}^{(1)} \end{pmatrix} \quad (3.31)$$

and the interaction matrix is given by:

$$T_l^c = \begin{pmatrix} 1 & D & 0 & 0 \\ 0 & 0 & 0 & T \\ 0 & 0 & 0 & 0 \\ 0 & 0 & 0 & L \end{pmatrix}, \quad (3.32)$$

where

$$I = (\epsilon_1^2 + \epsilon_2^2)(3 + 2\Gamma) + 2\epsilon_1\epsilon_2(1 + 4u^2\hat{\xi}^2\Gamma) \quad (3.33)$$

$$D = \{-8\epsilon_1\epsilon_2u^2\hat{\xi}^2\Gamma\}/I \quad (3.34)$$

$$T = \{-4k\epsilon_2\hat{\xi}(1 - 2\hat{\xi})u\Gamma\}/I \quad (3.35)$$

$$L = k\{(\epsilon_1^2 + \epsilon_2^2)(3 + 2\Gamma) - 2\epsilon_2(1 + 4u^2\hat{\xi}^2\Gamma)\}/I \quad (3.36)$$

and

ϵ_1	total energy of the first lepton $e^+(e^-)$ in units $m_e c^2$
ϵ_2	total energy of the second lepton $e^-(e^+)$ in units $m_e c^2$
\vec{p}	electron=positron initial momentum in units $m_e c$
\vec{k}	photon momentum in units $m_e c$
$k = (\epsilon_1 + \epsilon_2)$	energy of the incoming photon in units of $m_e c^2$
u	electron/positron initial momentum in units $m_e c$
$\hat{\xi}$	$= 1/(1 + u^2)$

Coulomb and screening effects are contained in Γ , defined in section 3.5.

Using Eq. (3.31) and the transfer matrix given by Eq. (3.32) the polarization state of the produced $e^-(e^+)$ is given in the Stokes formalism by:

$$\vec{\xi}^{(1)} = \begin{pmatrix} \xi_1^{(1)} \\ \xi_2^{(1)} \\ \xi_3^{(1)} \end{pmatrix} = \begin{pmatrix} \zeta_3^{(1)} T \\ 0 \\ \zeta_3^{(1)} L \end{pmatrix} \quad (3.37)$$

3.6.2 Simulation

Figure. 3.5 shows the polarization transfer from circularly polarized gammas to the produced e^+e^- . The high energy positron (electron) inherits the primary photon polarization. This plot shows a photon beam of 5 MeV and 100% circularly polarization passing through a 0.2 X_0 unpolarized tungsten target. In the physics list only *G4PolarizedGammaConversion* is considered.

3.7 Polarized Photoelectric Effect

This section describes the basic formulas of polarization transfer in the photoelectric effect class (*G4PolarizedPhotoElectricEffect*). The photoelectric effect is the emission of electrons from matter upon the absorption of electromagnetic radiation, such as ultraviolet radiation or x-rays. The energy of the photon is completely absorbed by the electron and, if sufficient, the

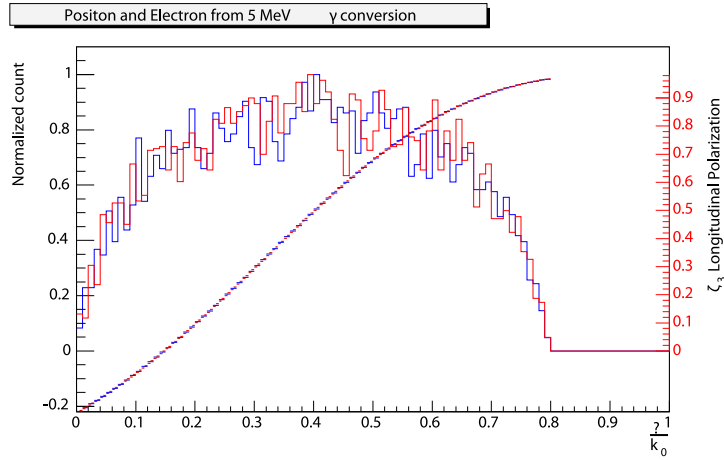


Figure 3.5: Normalized energy distribution (*left axis, histogram*) and degree of longitudinal polarization (polarization transfer) (*Right axis, curve*) of positrons/electrons (from gamma conversion) versus the fraction $\frac{\epsilon}{k_0}$ of kinetic energy transferred to the $e^+(e^-)$.

electron can escape from the material with a finite kinetic energy. A single photon can only eject a single electron, as the energy of one photon is only absorbed by one electron. The electrons that are emitted are often called photoelectrons. If the photon energy is higher than the binding energy the remaining energy is transferred to the electron as a kinetic energy

$$E_{kin}^{e^-} = k - B_{shell} \quad (3.38)$$

In Geant4 the photoelectric effect process is taken into account if:

$$k > B_{shell} \quad (3.39)$$

Where k is the incoming photon energy and B_{shell} the electron binding energy provided by the class *G4AtomicShells*.

3.7.1 Polarization transfer

Let us consider the photoelectric effect with an incoming polarized photon where the polarization state is described by the Stokes vector $\vec{\zeta}^{(1)}$. The polarization transfer to the photoelectron can be described in the Stokes formalism using the same approach as for the Bremsstrahlung and gamma conversion processes. The relation between the photoelectron's Stokes parameters and the incoming photon's Stokes parameters is described by the interaction matrix T_l^p derived from H. Olsen [Pratt(1961)] and reviewed by H.W McMaster

[McMaster.(1961)]:

$$\begin{pmatrix} I' \\ \vec{\xi}^{(1)} \end{pmatrix} = T_l^p \begin{pmatrix} I_0 \\ \vec{\zeta}^{(1)} \end{pmatrix} \quad (3.40)$$

In general, for the photoelectric effect as a two-body scattering, the cross section should be correlated with the spin states of the incoming photon and the target electron. In our implementation the target electron is not polarized and only the polarization transfer from the photon to the photoelectron is taken into account. In this case the cross section of the process remains polarization independent. To compute the matrix elements we take advantage of the available kinematic variables provided by the generic *G4PhotoelectricEffect* class. To compute the photoelectron spin state (Stokes parameters), four main parameters are needed:

- The incoming photon Stokes vector $\vec{\zeta}^{(1)}$
- The incoming photon's energy k .
- the photoelectron's kinetic energy $E_{kin}^{e^-}$ or the Lorentz factors β and γ .
- The photoelectron's polar angle θ or $\cos \theta$.

The interaction matrix derived by H. Olsen [Pratt(1961)] is given by:

$$T_l^P = \begin{pmatrix} 1 + D & -D & 0 & 0 \\ 0 & 0 & 0 & B \\ 0 & 0 & 0 & 0 \\ 0 & 0 & 0 & A \end{pmatrix} \quad (3.41)$$

Where

$$D = \frac{1}{k} \left[\frac{2}{k\epsilon(1 - \beta \cos \theta)} - 1 \right] \quad (3.42)$$

$$A = \frac{\epsilon}{\epsilon + 1} \left[\frac{2}{k\epsilon} + \beta \cos \theta + \frac{2}{k\epsilon^2(1 - \beta \cos \theta)} \right] \quad (3.43)$$

$$B = \frac{\epsilon}{\epsilon + 1} \beta \sin \theta \left[\frac{2}{k\epsilon(1 - \beta \cos \theta)} - 1 \right] \quad (3.44)$$

Using Eq. (3.40) and the transfer matrix given by Eq. (3.41) the polarization state of the produced e^- is given in the Stokes formalism by:

$$\vec{\xi}^{(1)} = \begin{pmatrix} \xi_1^{(1)} \\ \xi_2^{(1)} \\ \xi_3^{(1)} \end{pmatrix} = \begin{pmatrix} \zeta_3^{(1)} B \\ 0 \\ \zeta_3^{(1)} A \end{pmatrix} \quad (3.45)$$

From equation (3.45) one can see that a longitudinally (transversally) polarized photoelectron can only be produced if the incoming photon is circularly polarized. This interesting result is the reason for the use of circularly polarized lasers on a photocathode to produce longitudinally polarized electron beams for accelerators (SLC [R. Alley(1995)]).

3.8 Ionization

3.8.1 Method

The class *G4ePolarizedIonization* includes Møller (e^-e^-) and Bhabha (e^+e^-) scattering which describes the continuous and discrete energy losses of polarized electrons and positrons in a material. This class has been implemented by P. Starovoitov and A. Schällicke [P. Starovoitov(2007b)] and it evaluates both polarization transfer and asymmetries in the explicit delta ray production if the target electron (material) is polarized. The implementation baseline follows the approach derived for the generic class *G4eIonization* described in [GEANT4(2007)]. At very low energies the effects of a polarized beam or target are negligible and are therefore not considered. A user defined energy cut separates between the explicit delta rays due to the processes and the $\frac{dE}{dx}$ energy loss below this energy cut (known in Geant4 nomenclature as the continuous energy losses). In the explicit production of delta rays by Möller or Bhabha scattering, the effects of polarization on total cross section, mean free path and the average polarization of final state particles are taken into account.

3.8.2 Cross section

Møller cross section

The total cross section of the polarized Møller scattering can be expressed as follows

$$\sigma_{pol}^M = \frac{2\pi\gamma^2 r_e^2}{(\gamma - 1)^2(\gamma + 1)} \left[\sigma_0^M + \zeta_3^{(1)}\zeta_3^{(2)}\sigma_L^M + \left(\zeta_1^{(1)}\zeta_1^{(2)} + \zeta_2^{(1)}\zeta_2^{(2)} \right) \sigma_T^M \right], \quad (3.46)$$

Where the r_e is classical electron radius, and

- σ_0^M Unpolarized Møller cross section
- σ_L^M Møller cross section dependent on the longitudinal polarization
- σ_T^M Møller cross section dependent on the transverse polarization

The full expression of the total cross section can be found in [GEANT4(2007)].

Bhabha cross section

The total cross section of the polarized Bhabha scattering can be expressed as follows

$$\sigma_{pol}^B = \frac{2\pi r_e^2}{\gamma - 1} \left[\sigma_0^B + \zeta_3^{(1)} \zeta_3^{(2)} \sigma_L^B + \left(\zeta_1^{(1)} \zeta_1^{(2)} + \zeta_2^{(1)} \zeta_2^{(2)} \right) \sigma_T^B \right], \quad (3.47)$$

where

- σ_0^B Unpolarized Bhabha cross section
- σ_L^B Bhabha cross section dependent on the longitudinal polarization
- σ_T^B Bhabha cross section dependent on the transverse polarization

Differential cross section

The polarized differential cross section is rather complicated, the full result can be found in [P. Starovoitov(2007b), G. W. Ford(1957), Stehle(1958)]. In *G4PolarizedMollerCrossSection* the complete result is available taking all mass effects into account, only binding effects are neglected. Here we state only the ultra-relativistic approximation (URA), to show the general dependencies.

$$\begin{aligned} \frac{d\sigma_{URA}^M}{d\epsilon d\varphi} &= \frac{r_e^2}{\gamma + 1} \times \\ &\left[\frac{(1 - \epsilon + \epsilon^2)^2}{4(\epsilon - 1)^2 \epsilon^2} + \zeta_3^{(1)} \zeta_3^{(2)} \frac{2 - \epsilon + \epsilon^2}{-4\epsilon(1 - \epsilon)} + \left(\zeta_2^{(1)} \zeta_2^{(2)} - \zeta_1^{(1)} \zeta_1^{(2)} \right) \frac{1}{4} \right. \\ &\left. + \left(\xi_3^{(1)} \zeta_3^{(1)} - \xi_3^{(2)} \zeta_3^{(2)} \right) \frac{1 - \epsilon + 2\epsilon^2}{4(1 - \epsilon)\epsilon^2} + \left(\xi_3^{(2)} \zeta_3^{(1)} - \xi_3^{(1)} \zeta_3^{(2)} \right) \frac{2 - 3\epsilon + 2\epsilon^2}{4(1 - \epsilon)^2 \epsilon} \right] \end{aligned} \quad (3.48)$$

The dependence on the azimuthal angle φ is hidden in the transverse stokes parameters $\zeta_1^{(1)/(2)}$ and $\zeta_2^{(1)/(2)}$:

The corresponding Bhabha cross section is implemented in GEANT in the class *G4PolarizedBhabhaCrossSection*. In the ultra-relativistic approxi-

mation it reads

$$\begin{aligned} \frac{d\sigma_{URA}^B}{d\epsilon d\varphi} = \frac{r_e^2}{\gamma - 1} \times \\ \left[\frac{(1 - \epsilon + \epsilon^2)^2}{4\epsilon^2} + \zeta_3^{(1)}\zeta_3^{(2)} \frac{(\epsilon - 1)(2 - \epsilon + \epsilon^2)}{4\epsilon} + (\zeta_2^{(1)}\zeta_2^{(2)} - \zeta_1^{(1)}\zeta_1^{(2)}) \frac{(1 - \epsilon)^2}{4} \right. \\ \left. + (\zeta_3^{(1)}\zeta_3^{(1)} - \zeta_3^{(2)}\zeta_3^{(2)}) \frac{1 - 2\epsilon + 3\epsilon^2 - 2\epsilon^3}{4\epsilon^2} + (\zeta_3^{(2)}\zeta_3^{(1)} - \zeta_3^{(1)}\zeta_3^{(2)}) \frac{2 - 3\epsilon + 2\epsilon^2}{4\epsilon} \right] \end{aligned} \quad (3.49)$$

where

- r_e classical electron radius
- E_{p1} energy of the scattered electron/positron
- m_e electron mass
- E_{k1} energy of the incident electron/positron
- γ $E_{k1}/m_e c^2$
- ϵ $(E_{p1} - m_e c^2)/(E_{k1} - m_e c^2)$
- $\vec{\zeta}^{(1)}$ Stokes vector of the incoming electron/positron
- $\vec{\zeta}^{(2)}$ Stokes vector of the target electron
- $\vec{\xi}^{(1)}$ Stokes vector of the outgoing electron/positron
- $\vec{\xi}^{(2)}$ Stokes vector of the outgoing (2nd) electron
- φ The azimuthal angle defined by the polarization vector and the interaction plane.

3.8.3 Simulation

Figures 3.6, 3.7 show the polarization transfer to δ -electrons in the Møller and Bhabha scattering. One can notice that the high energy delta electrons inherit the polarization of the incoming particle (e^- or e^+). Fig. 3.8 describes the depolarization effects in the Bhabha scattering and one can see that even if the primary particle loses 50% of its energy it is still about 80% polarized. These results are produced by sending a 5 MeV, 100% longitudinally polarized positrons (electrons) through 0.2 X_0 unpolarized Tungsten target. In the physics list only the *G4ePolarizedIonization* process is active.

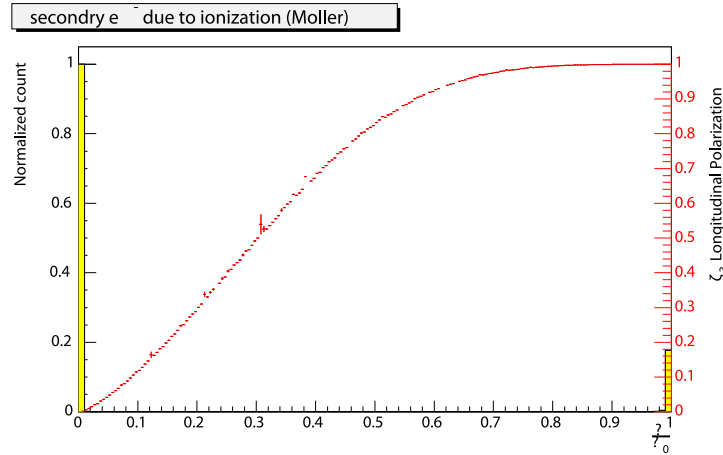


Figure 3.6: Normalized energy distribution (*left axis, histogram*) and degree of longitudinal polarization (polarization transfer - depolarization) (*right axis, curve*) of electrons versus the fractional kinetic energy loss $\frac{\epsilon}{\epsilon_0}$, where ϵ is the electron's kinetic energy and ϵ_0 the initial electron's kinetic energy.

3.9 Positron - Electron Annihilation

3.9.1 Method

The class *G4eplusPolarizedAnnihilation* simulates annihilation of polarized positrons with electrons in a material. The implementation evaluates the polarization transfer and, if the material is polarized, asymmetries in the produced photons. It takes into account the effects of polarization on the total cross section, mean free path, the distribution of final state photons, and calculates the average polarization of these photons. The electrons in the material are assumed to be free and at rest. The annihilation into three or more photons is neglected.

Total Cross Section

The total cross section of the annihilation of a polarized e^+e^- pair into two photons could be expressed as follows

$$\sigma_{pol}^A = \frac{\pi r_e^2}{\gamma + 1} \left[\sigma_0^A + \zeta_3^{(1)} \zeta_3^{(2)} \sigma_L^A + \left(\zeta_1^{(1)} \zeta_1^{(2)} + \zeta_2^{(1)} \zeta_2^{(2)} \right) \sigma_T^A \right], \quad (3.50)$$

with

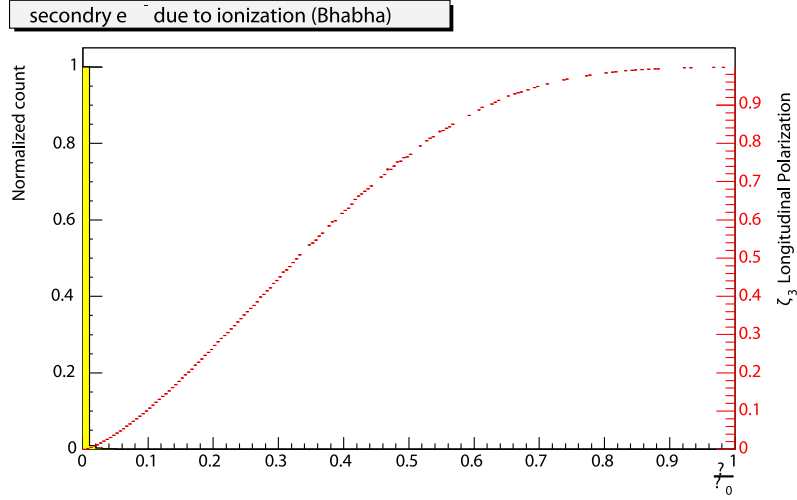


Figure 3.7: Normalized energy distribution (*left axis, histogram*) and degree of longitudinal polarization (polarization transfer) (*right axis, curve*) to electrons versus the fractional kinetic energy loss $\frac{\epsilon}{\epsilon_0}$, where ϵ is the electron kinetic energy and ϵ_0 the initial positron kinetic energy.

- σ_0^A unpolarized e^+ Annihilation cross section.
- σ_L^A e^+ Annihilation cross section dependent on linear polarization.
- σ_T^A e^+ Annihilation cross section dependent on longitudinal polarization.

The full expression of the total cross section can be found in [GEANT4(2007)].

Differential Cross Section

The fully polarized differential cross section is implemented in the class *G4PolarizedAnnihilationCrossSection*, which takes all mass effects into account, but binding effects are neglected [P. Starovoitov(2007a), Page(1957)]. In the ultra-relativistic approximation (URA) and including only longitudinal polarization the cross section is rather simple:

$$\frac{d\sigma_{URA}^A}{d\epsilon} = 2\pi \frac{r_e^2 Z}{\gamma - 1} \cdot \left(\frac{1 - 2\epsilon + 2\epsilon^2}{8\epsilon - 8\epsilon^2} (1 + \zeta_3^{(1)}\zeta_3^{(2)}) + \frac{(1 - 2\epsilon) (\zeta_3^{(1)} + \zeta_3^{(2)}) (\xi_3^{(1)} - \xi_3^{(2)})}{8(\epsilon - 1)\epsilon} \right) \quad (3.51)$$

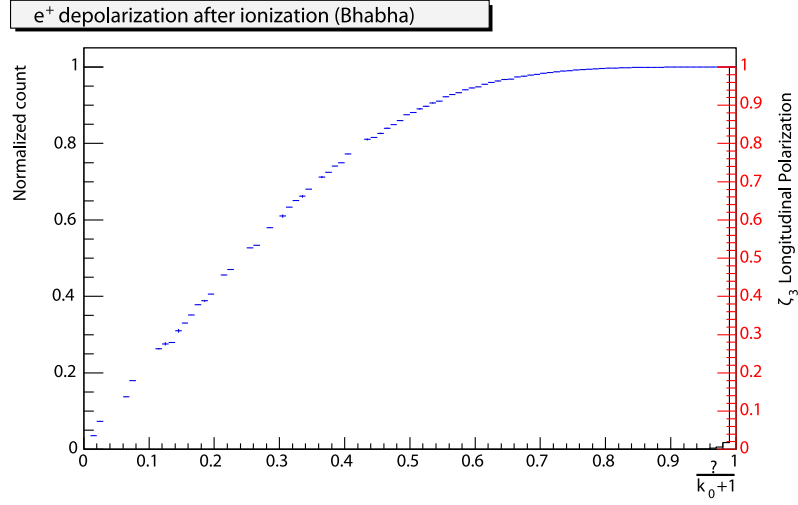


Figure 3.8: Normalized energy distribution (*left axis, histogram*) and degree of longitudinal polarization (depolarization effect) (*right axis, curve*) of positrons in Bhabha scattering versus the fractional kinetic energy loss of the initial particle $\frac{\epsilon}{\epsilon_0}$ where ϵ is the positron's total energy after Bhabha scattering and ϵ_0 the initial positron's kinetic energy.

- r_e classical electron radius
- E_{k_1} energy of the incident positron
- $\epsilon = (E_{p_1} - m_e c^2) / (E_{k_1} - m_e c^2)$
- $\gamma = E_{k_1} / m_e$
- $\vec{\zeta}^{(1)}$ Stokes vector of the incoming positron
- $\vec{\zeta}^{(2)}$ Stokes vector of the target electron
- $\vec{\xi}^{(1)}$ Stokes vector of the 1st photon
- $\vec{\xi}^{(2)}$ Stokes vector of the 2nd photon

3.9.2 Simulation

Figure 3.9 shows the polarization transfer from the primary positron to the photons in the annihilation process. Similarly to the previous processes, the high energy particles (photons) inherit the polarization of the incoming positron. This result is obtained by sending a 5 MeV, 100% longitudinally polarized positrons through an unpolarized tungsten target ($0.2 X_0$). In the physics list, only the *GeplusPolarizedAnnihilation* process is active.

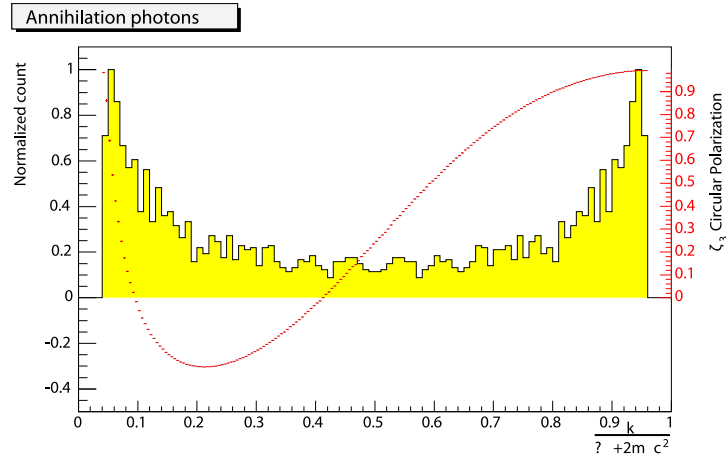


Figure 3.9: Normalized energy distribution (*left*) and degree of circular polarization (polarization transfer) (*right*) of annihilation photons versus the fractional total energy loss $\frac{k}{\epsilon_0 + 2m_e c^2}$ where k is the photon energy and ϵ_0 the initial positron kinetic energy.

3.10 Compton scattering

3.10.1 Method

The class *G4PolarizedCompton* simulates Compton scattering of polarized photons with (possibly polarized) electrons in a material. The implementation follows the approach described for the class *G4ComptonScattering*. The scattered photon and the electron ejected are created taking the effect of polarization on the total cross section and mean free path into account. The electrons in the material are assumed to be free and at rest.

3.10.2 Total cross section

The total cross section of Compton scattering reads

$$\sigma_{pol}^C = \frac{\pi r_e^2}{4 X^2 (1 + 2 X)^2} \left[\sigma_0^C + \zeta_3^{(1)} \zeta_3^{(2)} \sigma_L^C \right] \quad (3.52)$$

with

- σ_0^C unpolarized Compton cross section
- σ_L^C longitudinal polarization dependent cross section
- X $E_{k_1}/m_e c^2$

The full expression of the total cross section can be found in [GEANT4(2007)].

3.10.3 Differential Compton cross section

In the ultra-relativistic approximation the dependence of the differential cross section on the longitudinal/circular degree of polarization is:

$$\begin{aligned} \frac{d\sigma_{URA}^C}{d\epsilon} = 2\pi \frac{r_e^2}{4X} & \left(\frac{\epsilon^2 + 1}{2\epsilon} + \frac{\epsilon^2 - 1}{2\epsilon} \left(\zeta_3^{(1)} \zeta_3^{(2)} + \zeta_3^{(2)} \xi_3^{(1)} - \zeta_3^{(1)} \xi_3^{(2)} \right) \right. \\ & \left. + \frac{\epsilon^2 + 1}{2\epsilon} \left(\zeta_3^{(1)} \xi_3^{(1)} - \zeta_3^{(2)} \xi_3^{(2)} \right) \right) \end{aligned} \quad (3.53)$$

where r_e = classical electron radius

m_e = electron mass

E_{k_1} = energy of the incident photon

X = $E_{k_1}/m_e c^2$

ϵ = $(E_{p_1} - m_e c^2)/(E_{k_1} - m_e c^2)$

The fully polarized differential cross section is available in the class *G4PolarizedComptonCrossSection* [GEANT4(2007)]. It takes all mass effects into account, but binding effects are neglected [P.Starovoitov(2007), F. W. Lipps(1954)].

3.10.4 Simulation

Figures 3.10 and 3.11 show the depolarization effects on the primary photons after Compton scattering and the polarization transfer from the primary photon to the Compton electron respectively. These simulation results are obtained by sending 5 MeV, 100% circularly polarized photons through an unpolarized 0.2 X_0 tungsten target. In the physics list only *G4PolarizedCompton* process is active.

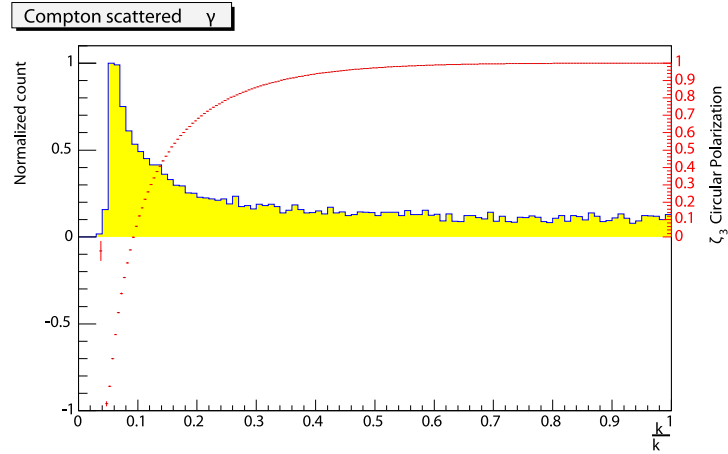


Figure 3.10: Normalized energy distribution (*left axis, histogram*) and degree of circular polarization (depolarization effect) (*right axis, curve*) of Compton scattered photons versus the fractional total energy loss of the initial state $\frac{k}{k_0}$ where k is the scattered photon energy and k_0 the initial photon energy.

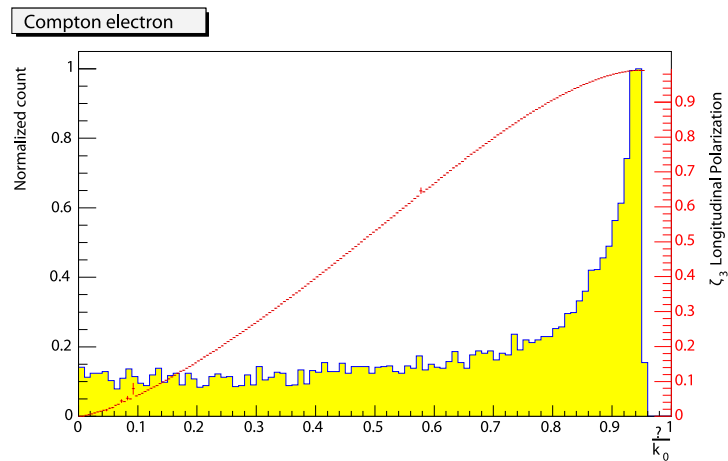


Figure 3.11: Normalized energy distribution (*left axis, histogram*) and degree of longitudinal polarization (polarization transfer) (*right axis, curve*) of Compton electrons versus the fractional total energy loss of the initial state $\frac{\epsilon}{k_0}$ where ϵ is the Compton electron total energy and k_0 the initial photon energy.

Chapter 4

Simulation of the positron generation and polarimetry

4.1 Introduction

In this chapter, the simulation of the generation and polarimetry of the positrons is described. The goal is the determination of the analyzing power for each spectrometer setting which is needed for the measurement of the positron polarization. In the following, three parts are discussed: the positron production mechanism, the transport system (spectrometer) and the positron polarimeter. The setup on the positron table is illustrated in Fig. 4.12 and the relevant parameters for the simulation are listed in Table 4.5.

The complete simulation study, starting from the undulator radiation, the e^+e^- production, particle tracking in the magnetic field of the transport system and the polarimetry, has been subdivided into four steps.

- In a first step, the undulator photons energy spectrum and polarization is generated (see Section 4.2).
- In a second step, the undulator photons are sent to a $0.2 X_0$ tungsten (W) target and the e^+e^- produced are collected. The collection is done at the surface of the target and concerns the spatial, energy, and angular distribution plus the polarization information of the produced particles (see Section 4.3).
- In a third step, the collected e^+e^- are sent through the transport system which dumps the electrons and guides the positrons to the polarimeter section. This third step focuses on the particle tracking from the positron conversion target through the spectrometer magnetic field up to the reconversion target (see Section 4.4).

- In the fourth and final step the positron polarimeter is simulated (see Section 4.6). In this part, the primary particles are positrons as collected at the reconversion target. These positrons are sent to the $0.5 X_0$ tungsten reconversion target to generate polarized photons via bremsstrahlung and/or annihilation processes. The photons are then transmitted through the magnetized absorber and collected by the CsI(Tl) calorimeter. By reversing the magnetization of the absorber an asymmetry in the photon transmission is recorded by the CsI(Tl) crystals.

From the recorded asymmetry the analyzing power of the polarimeter system is derived. The analyzing power is then used to derive the positron longitudinal polarization from the measured asymmetries discussed in Chapter 6. The analyzing power can only be extracted from simulations. It is sensitive to the polarimeter geometry, and the positron's energy, angular, and spatial distribution at the reconversion target.

4.2 The Helical Undulator Radiation

In this section we discuss the radiation and polarization of the E-166 undulator introduced in Section 2.2.1. The helical undulator principle and its polarized radiation is described in [Kincaid(1977), J. P. Blewett(1977), Mikhailichenko(2002)]. The basic formulas of the undulator radiation and its polarization are reviewed in this section. The positron production and its degree of longitudinal polarization are closely related to the energy range and polarization of the undulator photons.

An electron beam passing through the undulator is affected by the intrinsic helical magnetic field and starts to oscillate. The beam oscillations result in emission of circularly polarized photons. The undulator radiation can be understood as the inverse Compton scattering of the electron beam off virtual undulator photons.

Under such a helical profile of the magnetic field, a single electron describes a spiral trajectory with a constant velocity βc along the beam axis (z-axis):

$$\vec{r}(t) = \left[r \sin\left(\frac{2\pi\beta c}{\lambda_u}t\right), r \cos\left(\frac{2\pi\beta c}{\lambda_u}t\right), \beta ct \right] \quad (4.1)$$

with

$$\vec{\beta} = \beta \left(1 - \frac{K^2}{\gamma^2}\right)^{1/2} \vec{e}_r \quad \text{and} \quad r = \frac{K\lambda_u}{2\pi\gamma}.$$

The radiation spectrum of a moving charged particle in a helical magnetic field is calculated by means of the Lienard-Wiechert integral [J.D.Jackson(1982)] given by:

$$I(\omega, \Omega) = \frac{d^2 I}{d\omega d\Omega} = \frac{e^2 \omega^2}{16\pi^3 \varepsilon_0 c} \left| \int_{-\infty}^{+\infty} \vec{n} \times (\vec{n} \times \vec{\beta}(t)) e^{i\omega(t - \frac{\vec{n}\vec{r}}{c})} dt \right|^2 \quad (4.2)$$

Where

$$\begin{aligned} \vec{n} &: && \text{unit vector in the direction of observation} \\ \Omega &: && \text{solid angle} \\ \vec{r}(t) &: && \text{electron trajectory} \\ \vec{\beta} &= \frac{d\vec{r}}{dt} \frac{1}{c} \end{aligned}$$

Introducing the dimensionless parameter K , the undulator radiation spectrum and the energy cutoff for different harmonics can be determined by three convenient and independent parameters: The K -factor which is related to the undulator period λ_u , the on-axis transverse magnetic field \vec{B} and the γ factor which translates the electron beam energy. For a small K -factor, the first harmonic is dominant (see fig 4.1) and thus relevant for the positron production. But the gamma conversion cross section scales with the photon energy and higher harmonics may also have a relatively important contribution to the positron production depending on the kinematical region of interest. The undulator K -factor and the energy cutoff E_1 of the first harmonic are given by:

$$K = \frac{e}{2\pi m_0 c} B \lambda_u = 0.934 B[T] \lambda_u[cm] \quad (4.3)$$

$$E_1 = \hbar\omega_1 = \hbar \frac{4\pi\gamma^2 c}{(1 + K^2)\lambda_u} \quad (4.4)$$

The K -factor determines the shape of the radiation spectrum, while the energy cutoff of the first harmonic E_1 defines the scale of the energy axis. For a helical undulator, the photon number integrated over a solid angle ($0 < \theta < \pi/2$) is given by:

$$\frac{dN_{ph}}{dE} \left[\frac{1}{m.MeV} \right] = \frac{10^6 e^3}{4\pi\varepsilon_0 c^2 \hbar^2} \frac{K^2}{\gamma^2} \sum_{n=1}^{\infty} \left(J_n'(x)^2 + \left(\frac{\alpha_n}{K} - \frac{n}{x} \right)^2 J_n'(x)^2 \right) \quad (4.5)$$

with

$\alpha_n^2 = \left[n \frac{\omega_1(1+K^2)}{\omega} - 1 - K^2 \right]$
 $J_n(x)$ the Bessel functions
 $x = 2 K \frac{\omega}{\omega_1(1+K^2)} \alpha_n$
 and the degree of circular polarization is given by:

$$P_{n=1}(s) = P_{n=2}(s) = \frac{2s - 1}{1 - 2s + 2s^2} \quad (4.6)$$

$s = \frac{E}{E_n}$ is the photon energy normalized to the energy cutoff of the harmonic number n .

A typical undulator photon spectrum for the first three harmonics and their respective polarization profile for the E-166 parameters listed in Table 4.1 are shown in Fig. 4.1 (A) and (B).

The radiated power by an electron beam with energy E_e passing one meter of undulator is given by:

$$\frac{d^2U_u}{dLdt} = 2.32 \cdot 10^{-4} \frac{(E_e/GeV)^2 K^2}{\lambda_u^2/mm} (n_e \cdot 10^{10}) (f_{rep}/Hz) \text{ W/m}, \quad (4.7)$$

in which n_e is the number of electrons per pulse and f_{rep} is the pulse repetition rate.

A small contribution of higher-order radiation (second and third harmonics) can be seen in Fig. 4.1 (A) for normalized energies $1 \leq \frac{E}{E_n} \leq 3$. For the E-166 parameters, the contribution of the first three harmonics to the total undulator radiation are given in Table 4.2. For an electron beam energy of 46.6 GeV and an undulator K -factor of 0.19, the fraction of the first harmonic photons is about 96 %. The degree of circular polarization for photons at the sharp edge energy cutoff of any harmonic seen independently of the others reaches the value of +1. However the overlap of successive harmonics may induce a slightly lower value than +1.

The undulator photon spectrum and its circular polarization profile as shown in Fig. 4.1 are taken as an input to the simulation for the polarized positron production discussed in the next sections.

4.3 Polarized Positron (Electron) Production

In this section the energy distribution and the polarization profile of the positrons and electrons generated by the undulator photons are determined as they emerge off the conversion target. In the experiment both the positrons and electrons are studied for the need of cross-checks and comparison with the simulation. Therefore we have tried to understand the production mechanism

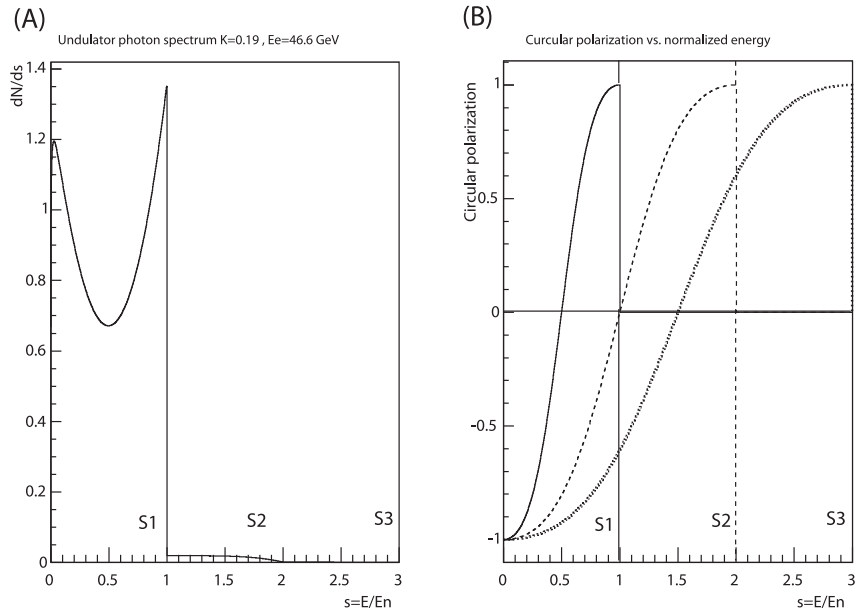


Figure 4.1: (A) Undulator photon spectrum for the first three harmonics ($n=1, 2, 3$). (B) their respective circular polarization profile versus normalized energy $s = \frac{E}{E_n}$

and polarization for both particles. For the positron (electron) generation, the polarized processes were used and which track the polarization transfer from the primary photons to the leptons produced as discussed in Chapter 3.

In the simulation, the undulator spectrum (the first three harmonics), including the information on the photon circular polarization, is sent to a $0.2 X_0$ Tungsten target (see Section 2.2.2) and the positrons (electrons) produced are collected. Because of the small target thickness (0.81 mm), only a small fraction (8%) of the primary photons are converted into e^+e^- . The relevant processes at the target are gamma conversion, Compton scattering, photoelectric effect and ionization. From the e^+e^- produced in the target material, only a small fraction will have the capability to escape from the target and reach its surface which leads to a small e^+e^- yield (up to about 2%).

4.3.1 Positron and Electron Yield

Starting from an undulator photon as a mother particle interacting with the target material, the production mechanisms for positrons and electrons

Parameter	Units	Value
electron beam energy	GeV	46.60
magnetic field of undulator	T	0.8008
undulator period	cm	0.2540
K-value		0.1900
energy of first harmonic	MeV	7.836
wavelength of first harmonic	nm	$1.582 \cdot 10^{-4}$
number of harmonics calculated		3
total number of photons per e^-	m^{-1}	0.4281
total radiated power	MeV/m	1.762

Table 4.1: Undulator radiation parameters in E-166 for an electron beam energy of 46.6 GeV and $K=0.19$.

Harmonic number n	fraction	E_n [MeV]
1	0.958394	7.836
2	0.039644	15.672
3	0.001962	23.508

Table 4.2: Contribution of the first, second and third harmonic to the total undulator radiation and their energy cutoff E_n for $K=0.19$.

differ. For positrons, only the gamma conversion process is responsible, while electrons can be produced by four processes. In addition to the gamma conversion, electrons can be generated by Compton scattering, photoelectric effect and ionization.

In the energy range of the undulator spectrum with its three harmonics (up to $E_3 = 23$ MeV) depending on the cross sections, all four processes contribute and result in a larger yield for electrons. The electron yield is larger by a factor 2.2 if compared to the positron yield (see Fig. 4.2).

The positron (electron) yield $Y_{e^+(e^-)}^{4\pi}$ at the conversion target is defined by the ratio

$$Y_{e^+(e^-)}^{4\pi} = \frac{N_{e^+(e^-)}^{4\pi}}{N_\gamma} \quad (4.8)$$

Where $N_{e^+(e^-)}^{4\pi}$ is the number of positrons (electrons) collected at the surface of the conversion target in 4π steradian and N_γ is the number of undulator photons sent to the target.

The values of the positron (electron) yield are listed in Table 4.3 and the energy distribution of electrons created by different processes are shown in Fig. 4.3. The processes contributing to the electron production versus energy

is illustrated in Fig. 4.4 and their fractional numbers are given in Table 4.4. About 50% of the electrons come from Compton scattering, 39% from gamma conversion and the rest is distributed over the photoelectric effect (7.5%) and ionization (3.5%).

The energy conservation in the gamma conversion process leads to a maximum energy $E_{1(max)}^{e^+}$ for a produced positron given for the first harmonic by:

$$E_{1(max)}^{e^+} = E_1 - m_0c^2 = 7.3 \text{ MeV} \quad (4.9)$$

For electrons, the upper limit in energy $E_{1(max)}^{e^-}$ can be derived from the energy conservation in Compton scattering which leads to:

$$E_{1(max)}^{e^-} = E_1 + m_0c^2 = 8.3 \text{ MeV} \quad (4.10)$$

Where E_1 is the energy cutoff of the first harmonic given by Eq. 4.4 and $m_0c^2=0.511$ MeV the electron rest mass. For the E-166 parameters $E_1 = 7.8 \text{ MeV}$

For positrons and electrons, the relative deviation in the energy upper limit ($E_{1(max)}^{e^-} - E_{1(max)}^{e^+} = 2m_0c^2 = 1.02 \text{ MeV}$) and the production mechanism lead to a significant difference in the energy distribution and the expected polarization profile. The positron energy distribution is compared to the electron energy distribution in Fig. 4.2(A) and the ratio N_{e^-}/N_{e^+} versus energy is plotted in (B).

Particle	Yield [$e^+(e^-)/\gamma$]
Positron	0.0085
Electron	0.0187

Table 4.3: Positron and electron yield for $K=0.19$ and $E_e = 46.6 \text{ GeV}$. Target W alloy with thickness = 0.81 mm

In the experiment we have selected five positron momenta and one electron momentum. The momentum selection was performed using a magnetic spectrometer (Section 2.3.1) and will be discussed in details in Section 4.4.3. The momentum resolution $\Delta P/P$ of the selected distributions was better than 5%, thus comparison of the ratio N_{e^-}/N_{e^+} as a function of energy can serve as a sensitive crosscheck of the experimental data and the simulation of the spectrometer calibration and yields. The ratio of the integrated positron (electron) numbers $N_{e^-}^{Tot}/N_{e^+}^{Tot} = 2.2$ characterizes the yield for positrons and electrons. But the ratio N_{e^-}/N_{e^+} is energy dependent and may reach values up to 7 as seen in the energy region between 5 MeV and 8 MeV. In this specific energy range one can see from Fig. 4.3 and 4.4 that Compton scattering

dominates the electron production. As an example: at an energy of 7 MeV near the positron upper limit, about 75% of the electron production comes from Compton scattering and only 13% from gamma conversion and 12% from photoelectric effect. At this energy the ratio N_{e^-}/N_{e^+} is about 7.

Process	Fraction
Compton fraction	0.498697
Gamma Conversion	0.38753
Photoelectric	0.0772942
Ionization	0.0364795

Table 4.4: Different contributions to the electron production for $K=0.19$, electron beam energy $E_e = 46.6$ GeV. Target W alloy thickness = 0.81 mm

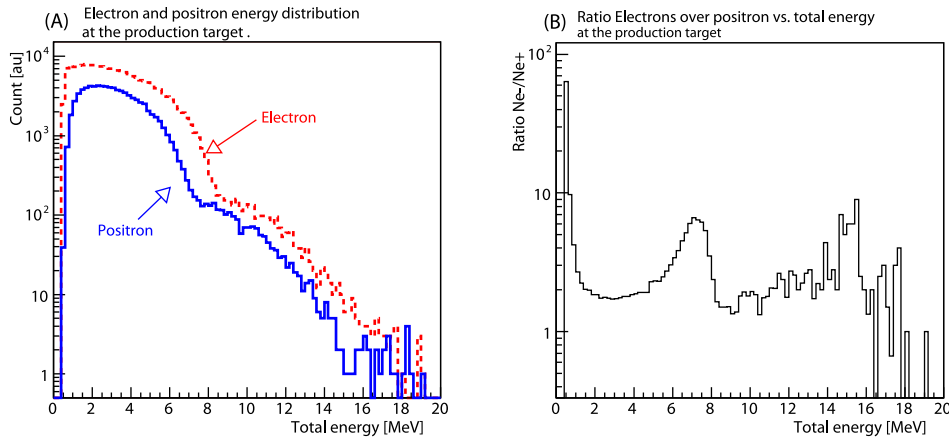


Figure 4.2: (A) Electron and positron energy distribution at the surface of the production target. (B) Ratio of electrons to positrons ($\frac{N_{e^-}}{N_{e^+}}$) versus the e^+e^- energy

4.3.2 Positron and Electron Polarization

Since the production mechanism for positrons and electrons is not the same, the expected longitudinal polarization for these particles is different. Figure 4.5 shows significant deviations when comparing the polarization profiles for both particles. At low energies, below 6 MeV, electrons show a lower longitudinal polarization than to positrons. This is mainly due to the reduced polarization transfer from the photon to the electron in Compton scattering, photoelectric effect and ionization. For positrons at energies above 6 MeV, a

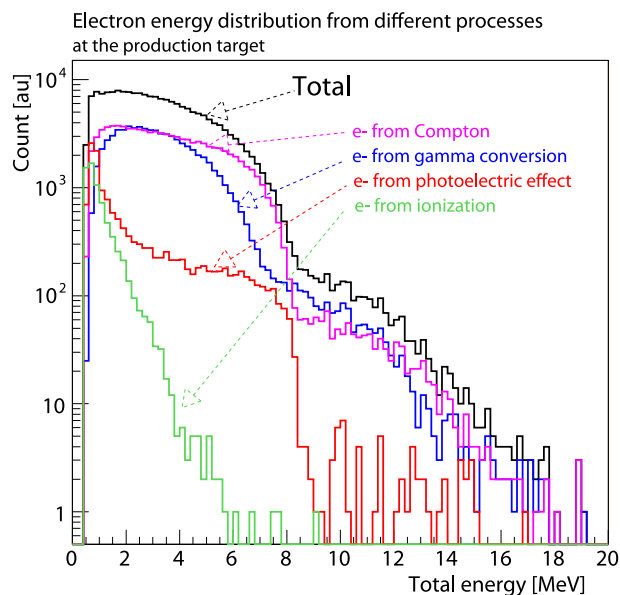


Figure 4.3: Electron energy distribution from different processes (gamma conversion, Compton effect, photoelectric effect and ionization).

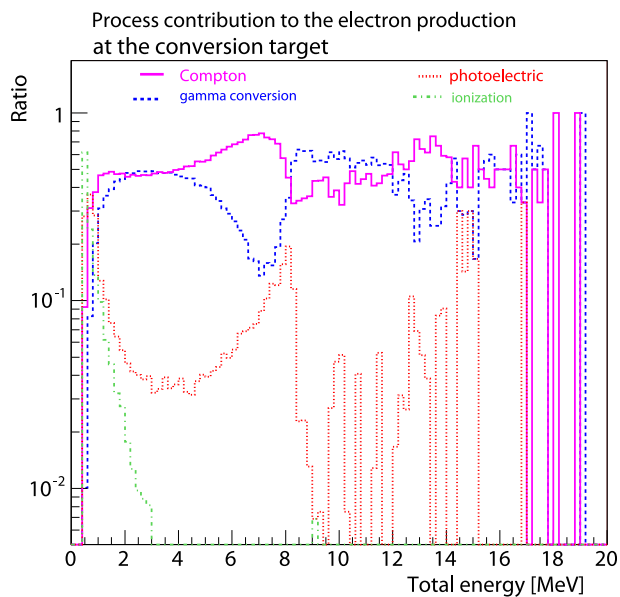


Figure 4.4: Contributions of different processes to the electron production at the conversion target ($\frac{N_{process}(e^-)}{N_{e^+}}$) versus the e^- energy.

drop in polarization with a minimum at an energy around $E_{1(max)}^{e^+} = 7.3 \text{ MeV}$ can be seen. Similarly for electrons, a minimum polarization around an energy $E_{1(max)}^{e^-} = 8.3 \text{ MeV}$ is notable. From the simulation, a maximal longitudinal polarization of $P_{e^+}^{max} \approx 80\%$ and $P_{e^-}^{max} \approx 87\%$ at about 6 MeV and 7 MeV respectively is expected.

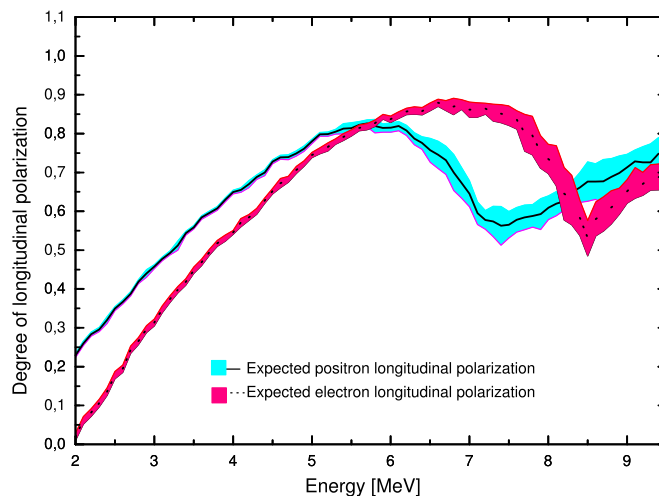


Figure 4.5: Positron and electron expected longitudinal polarization with statistical error bands.

4.4 The $e^+(e^-)$ Transport System

4.4.1 Overview of the setup

The transport system (Section 2.3.1) guided the positrons from the conversion target to the polarimeter section while dumping the electrons. It selects a narrow momentum range ($\frac{\sigma}{E} \leq 5\%$) from the broad e^+ distribution emitted at the production target.

The selection mechanism and the e^+e^- kinematics in the magnetic field, was simulated using Geant4. In this section, we describe the geometry of the transport system and the field map implemented using a combination of the measured axial field for the solenoid and the MERMAID based field map for the spectrometer.

Due to the specific geometry of the spectrometer dipoles and solenoid field close-by, the transport system has a complex magnetic field distribution. To record the spatial and momentum distribution of particles in the transport process, two virtual detectors are placed in the setup. The first one at the position of the PosSi counter and the second at the reconversion target (Fig. 4.12).

At the entrance region of the transport system, the angular acceptance is limited due to the geometry of the setup. The conversion target is located 147.6 mm away from the entrance of the vacuum chamber. An inner radius of 18 mm of the vacuum pipe leads to an angular acceptance of about $2\theta = 14^\circ$. In the absence of a solenoid (lens) magnetic field, the positron fraction within the angular acceptance ($\cos\theta \geq 0.992$) is less than 5.4%.

Relevant Parameters	Material and values
undulator photons	3 first harmonics
undulator photon beam shape	3 mm disk.
Geant4 energy cutoff for photons	1 keV
conversion target material	tungsten (W).
conversion target thickness	0.2 X0
reconversion target material	tungsten (W).
reconversion target thickness	0.5 X0.
reconversion target radius.	radius = 25 mm
vacuum (vacuum chamber)	10^{-3} Torr
vacuum pipe (entrance-spectrometer)	inner radius = 18 mm
vacuum pipe (exit-spectrometer)	inner radius = 24 mm
jaws opening (momentum slit)	30 mm
solenoid magnetic field.	SLAC's measurement
spectrometer magnetic field.	MERMAID
magnetic field (implementation method)	3D linear interpolation
step length (G4 tracking in a magnetic field)	100 μm

Table 4.5: Target and beam parameters used for the simulation of the e^+e^- transport system

4.4.2 Solenoid Magnetic Field

Due to the limitation in the angular acceptance discussed above, a solenoid was placed between the conversion target and the entrance of the spectrometer's vacuum chamber. The solenoid's magnetic field can be tuned to provide a proper focusing to maximize the positron yield at the reconversion target.

The focal point of the positions is energy (momentum) dependent and leads to a continuum of focal points at different positions along the solenoid axis. In a simplest scheme shown in Fig. 4.8 (A), the low energy particles are focused close to the center of the solenoid and the high energy ones are focused further from the center. In the experiment the solenoid was tuned to focus the produced positrons on the reconversion target. The beam formed by drifting particles that emerge from the solenoid and reach the reconversion target is quasi-monochromatic.

Implementation

The solenoid magnetic field was measured along the z axis for different x positions using a one dimensional Hall probe which provides only the B_z component. The measured $B_z(x, y = 0, z)$ at different x coordinates for $y=0$ is shown in Fig. 4.6. To model the solenoid and its focusing effect, both B_z and B_r are required. To recover the missing components in the complete solenoid 3D space an extrapolation method which fulfills Maxwell's equation $\text{div} \vec{B} = 0$ is used. The $B_r(r, \phi, z)$ and $B_z(r, \phi, z)$ are derived from the measured on-axis B_z using a 3D cylindrical extrapolation method for solenoid magnetic fields given by [Pöchel(2004)]:

$$B_r = -\frac{r}{2} \left(\frac{dB_0(z)}{dz} - \frac{r^2}{8} \frac{d^3 B_0(z)}{dz^3} \right) \quad (4.11)$$

$$B_\phi = 0 \quad (4.12)$$

$$B_z = B_0(z) - \frac{r^2}{4} \frac{d^2 B_0(z)}{dz^2} \quad (4.13)$$

where $B_0(z)$ is the measured axial field of the solenoid.

Following this approach, the on-axis B_z component is fitted by a Gaussian function and the full 3D map of the solenoid field is calculated.

By scanning the solenoid current from 0 A up to 400 A, the positron statistics at the entrance region increases to an optimum point then it decreases for higher current. The maximum statistics at the entrance region is recorded for a solenoid current $I_L = 200$ A. At this current 13.5 % of all positrons from the conversion target enter the spectrometer vacuum chamber. The positron yield is increased by the solenoid by a factor of 2.5. The focusing is then followed by beam transport through the double-bend magnets to the reconversion target. Detailed results and illustrations on the solenoid focusing effects can be found in [Laihem(2006b), Laihem(2006c)].

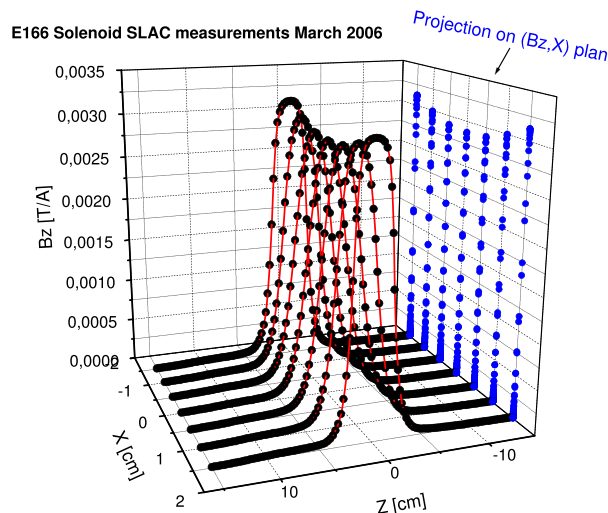


Figure 4.6: Measured solenoid magnetic field for different x position

4.4.3 Spectrometer Magnetic Field

The spectrometer magnetic field used in the simulation was calculated using the MERMAID software [Mikhailichenko(2005)] for a spectrometer current of 150 A. MERMAID uses a finite-element-based calculation algorithm which takes into account the geometry and the magnetic properties of different components of a given setup. For the E-166 spectrometer, the field map consists of ten parallel xz plans grouped into a 3D lattice covering the region of the vacuum chamber and extending from the conversion target up to the polarimeter section. In this 3D lattice, at each node (x,y,z) the three components (Bl_x, Bl_y, Bl_z) are given. In Fig. 4.9, the calculated magnetic field is compared to the measured field which shows a good agreement. The 3D plot and the contour of the component B_y at the midplane (ie. $y=0$) are shown in Fig. 4.10.

Spectrometer Magnetic Field versus Electrical Current

The MERMAID field map was calculated for a fixed spectrometer current of 150 A. To extrapolate the field map to different spectrometer currents, measurements of the magnetic field as a function of the spectrometer current were done [Bugg(2006)].

In the absence of saturation effects the magnetic field changes linearly

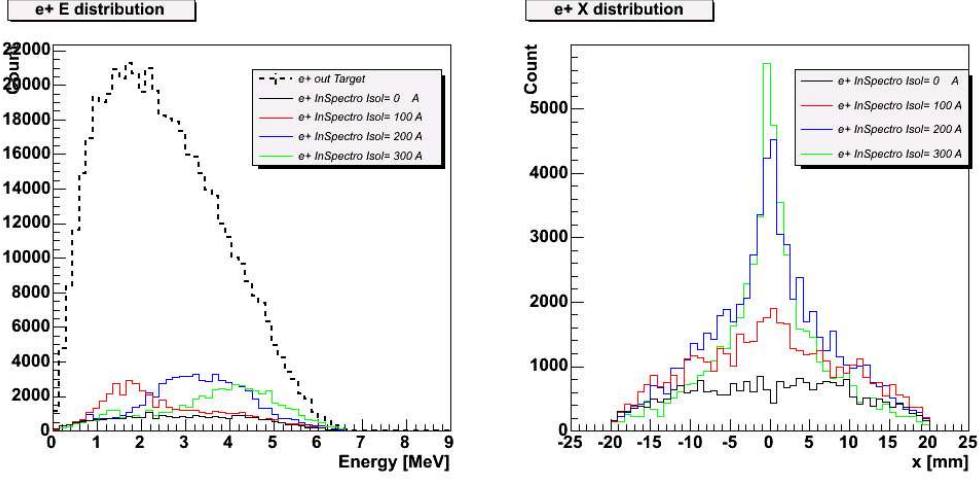


Figure 4.7: The left plot shows the primary positron energy distribution at the conversion target which is compared to the energy distribution of positrons entering the spectrometer vacuum chamber for different solenoid currents. The right plot shows their respective x distribution at the entrance of the vacuum chamber with a focusing effect when increasing the solenoid current. In the legend, "InSpectro" stands for "at the entrance of the spectrometer vacuum chamber" and " I_{sol} " stands for the solenoid current I_L .

with the current. But the measurements exhibit a non-linearity which is attributed to saturation in the iron yokes. The measurements were done using a one-dimensional Hall probe in the region closest to the dipole yokes where the magnetic field is maximum. In this region the transverse magnetic field versus current shows a quadratic behavior given by:

$$B_y(I_S) = aI_S^2 + bI_S + c \quad (4.14)$$

in which B_y is the transverse magnetic field, I_S is the spectrometer current and $a = -1.683 \cdot 10^{-6} T/A^2$, $b = 1.536 \cdot 10^{-3} T/A$ and $c = 1.841 \cdot 10^{-3} T$.

In the case of linear relation between the spectrometer current I_S and the magnetic field B_S , the MERMAID field map $B_S(150 A)$ is extrapolated to different spectrometer current I_S using:

$$\vec{B}_S(I_S) = \frac{I_S}{150 A} \cdot \vec{B}_S(150 A) \quad (4.15)$$

In the case of the quadratic relation given by Eq. 4.14, the extrapolation of the field map $B_S(150 A)$ uses:

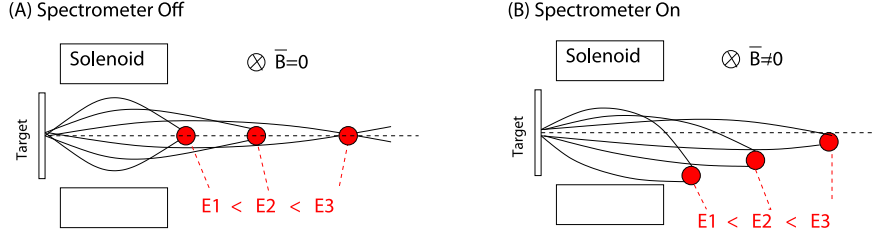


Figure 4.8: (A): scheme of the system Target-Lens-spectrometer (OFF) illustrating the focusing effect of the solenoid for different e^+ energy. (B) Combined effect on the focusing and drift when the spectrometer is ON

$$\vec{B}_S(I_S) = \frac{aI_S^2 + bI_S + c}{B_S^{max}(150 A)} \cdot \vec{B}_S(150 A) \quad (4.16)$$

with $B_S^{max}(150 A) = 0.2T$ the maximum measured (calculated) magnetic field in the region where the distance between the yokes is minimal (see Fig. 4.9).

Implementation

The MERMAID field map is implemented in the Geant4 system using a 3D linear interpolation method. This method consists of segmenting the 3D space of the field region into parallepipeds defined by 8 nodes where the calculated field values are given. In the tracking procedure, a particle entering the field region, is localized by its coordinates and a parallepiped is assigned until it enters the next parallepiped. In this way, the e^+ inside the parallepiped is under a combined magnetic field resulting from the 8 surroundings nodes. The B_x , B_y and B_z component at any point x , y and z inside the parallepiped are given by:

$$\begin{aligned} B_x = & Blx_{i,j,k}(1-x)(1-y)(1-z) + Blx_{i,j,k+1}(1-x)(1-y)z \\ & + Blx_{i,j+1,k}(1-x)y(1-z) + Blx_{i,j+1,k+1}(1-x)yz \\ & + Blx_{i+1,j,k}x(1-y)(1-z) + Blx_{i+1,j,k+1}x(1-y)z \\ & + Blx_{i+1,j+1,k}xy(1-z) + Blx_{i+1,j+1,k+1}xyz \end{aligned} \quad (4.17)$$

$$\begin{aligned}
B_y = & Bly_{i,j,k}(1-x)(1-y)(1-z) + Bly_{i,j,k+1}(1-x)(1-y)z \\
& + Bly_{i,j+1,k}(1-x)y(1-z) + Bly_{i,j+1,k+1}(1-x)yz \quad (4.18) \\
& + Bly_{i+1,j,k}x(1-y)(1-z) + Bly_{i+1,j,k+1}x(1-y)z \\
& + Bly_{i+1,j+1,k}xy(1-z) + Bly_{i+1,j+1,k+1}xyz
\end{aligned}$$

$$\begin{aligned}
B_z = & Blz_{i,j,k}(1-x)(1-y)(1-z) + Blz_{i,j,k+1}(1-x)(1-y)z \\
& + Blz_{i,j+1,k}(1-x)y(1-z) + Blz_{i,j+1,k+1}(1-x)yz \quad (4.19) \\
& + Blz_{i+1,j,k}x(1-y)(1-z) + Blz_{i+1,j,k+1}x(1-y)z \\
& + Blz_{i+1,j+1,k}xy(1-z) + Blz_{i+1,j+1,k+1}xyz
\end{aligned}$$

as a function of x, y, z and Blx, Bly, Blz the calculated field values at the 8 nodes $(i, j, k), (i, j, k+1), (i, j+1, k), (i, j+1, k+1), (i+1, j, k), (i+1, j, k+1), (i+1, j+1, k), (i+1, j+1, k+1)$ as shown in Fig. 4.11.

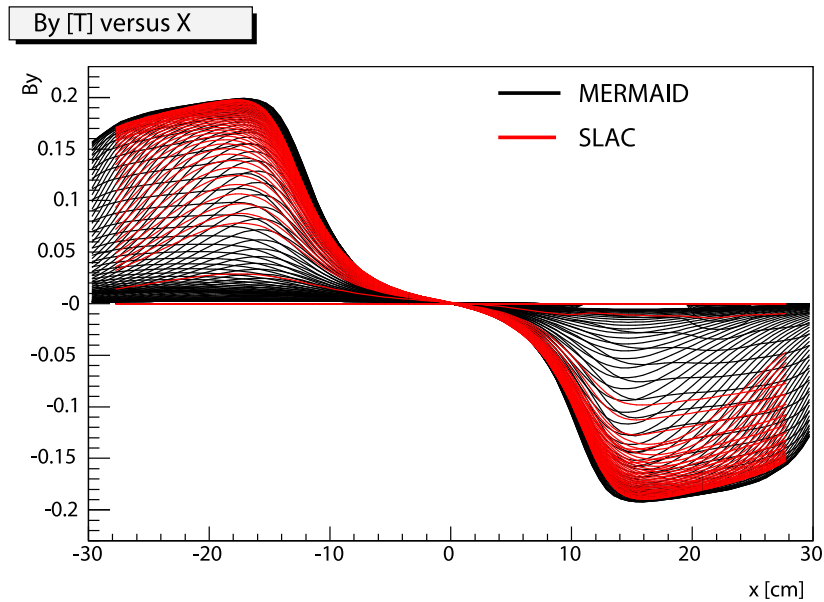


Figure 4.9: Spectrometer field map for the mid plan $y=0$. Comparison between the MERMAID calculation and the measured field map from SLAC.

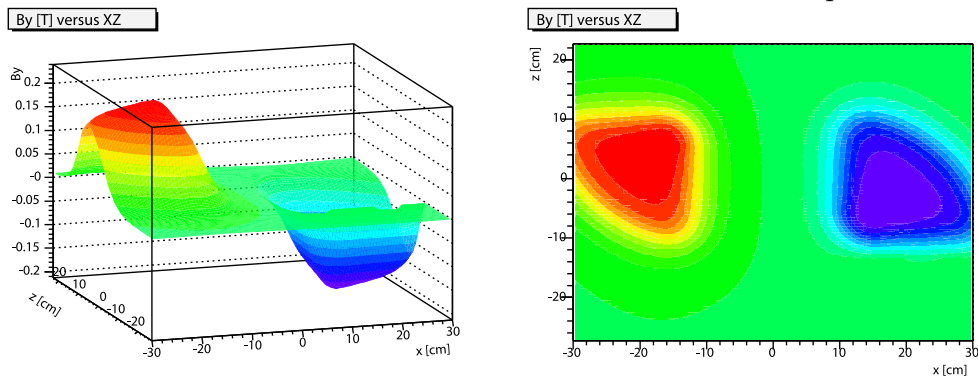


Figure 4.10: Spectrometer field map (MERMAID) for $y=0$ (mid plan). Left: 3d view of the transverse magnetic field B_y versus XZ . Right: contour plot of B_y versus XZ

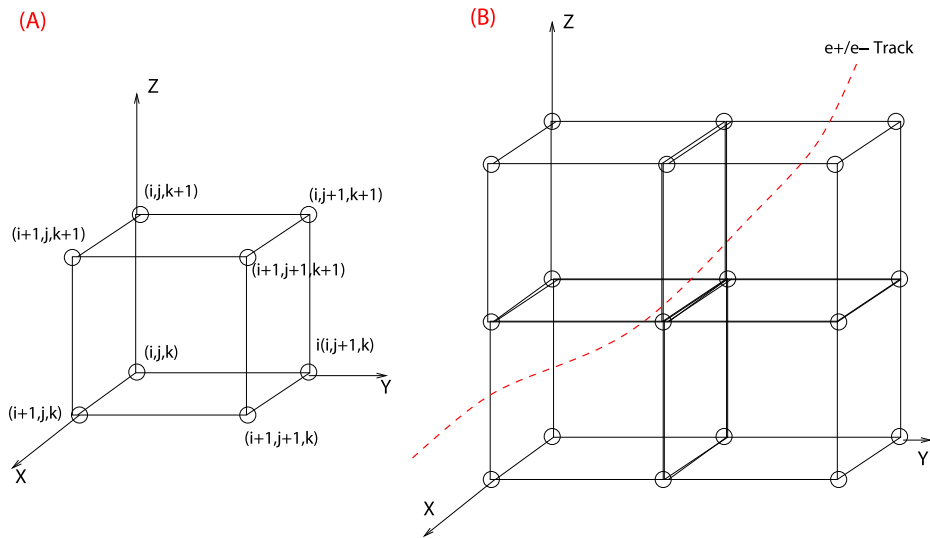


Figure 4.11: (A): Scheme of one segment for the 3D interpolation. (B): Scheme of the 3D segmentation method for the e^+e^- tracking in the field map

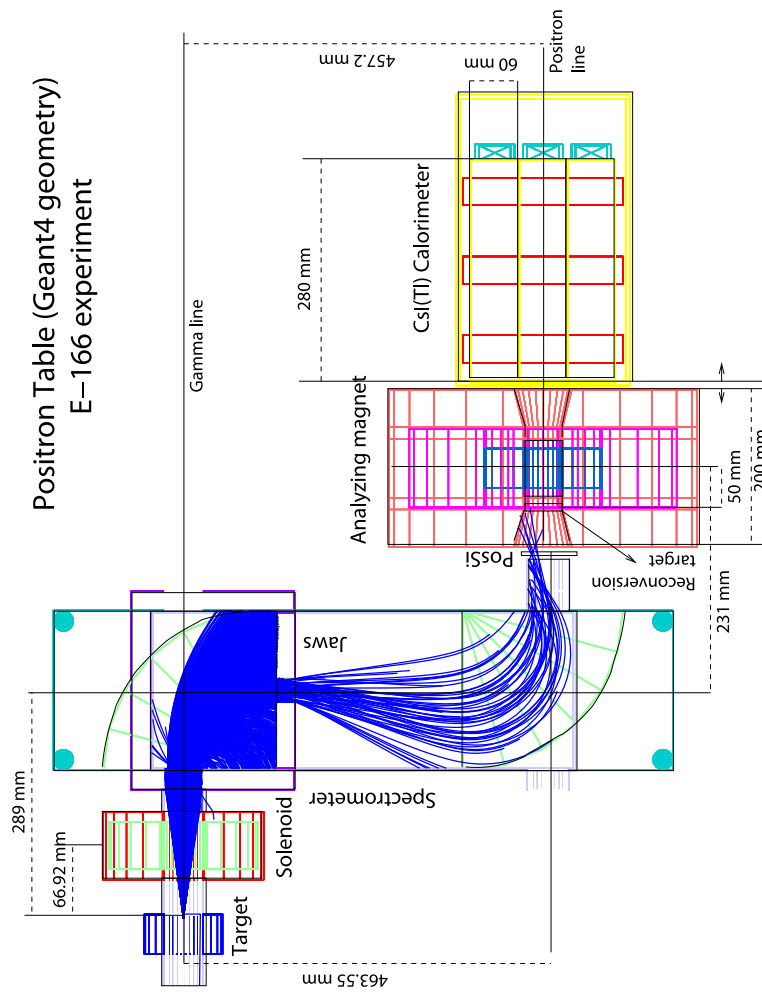


Figure 4.12: Schematic of the E-166 transport system illustrating the positron tracks under the solenoid and spectrometer magnetic field

4.5 Simulation Of The e^+e^- Transport

The positrons collected at the conversion target (see Section 4.3) are sent through the transport system and tracked in the magnetic field up to the polarimeter stage. In the tracking procedure, the momentum and spatial distributions of the positrons are recorded by two planes placed at the position of the PosSi counter and at the reconversion target (see Fig. 4.12). The simulation protocol adopted in the study can be summarized in 4 points.

1. Determination of the setting points (I_S, I_L) . The setting point is defined by a spectrometer current I_S and a solenoid current I_L for which the transmission through the transport system is maximum.
2. Determination of the positron transmission through the spectrometer system for each setting point (I_S, I_L) .
3. Determination of the positron energy (momentum) distribution at the PosSi counter and at the reconversion target for each setting point (I_S, I_L) . This step is the spectrometer momentum calibration.
4. Determination of the positron spatial distribution at the PosSi counter and at the reconversion target.

4.5.1 Setting Points and Transmission through the Spectrometer

The setting points are derived from the simulation following a similar procedure as adopted in the experiment. The procedure consists of scanning the solenoid current I_L for a given spectrometer current I_S to localize the maximum transmission through the transport system. In the simulation, the solenoid current I_L is scanned from 0 A up to 400 A with a step size of 25 A for each spectrometer current I_S set to 100 A, 120 A, 140 A, 160 A and 180 A. The spectrometer's magnetic field B_S versus the spectrometer current was implemented using two approaches. The first approach has a linear relation between B_S and I_S and the second approach was implemented using the quadratic relation discussed in Section 4.4.3. The simulation results are compared to the experimental setting points in Fig. 4.13 which shows a good agreement at low spectrometer currents. However, at high spectrometer currents up to 12% deviation from the experimental data is observed.

The transmission through the transport system is energy dependent and it is defined as $T_{PosSi}^{e^+}(E) = \frac{N_{PosSi}^{e^+}}{N_{Tr}^{e^+}(E)}$ where $N_{PosSi}^{e^+}$ is the number of positrons

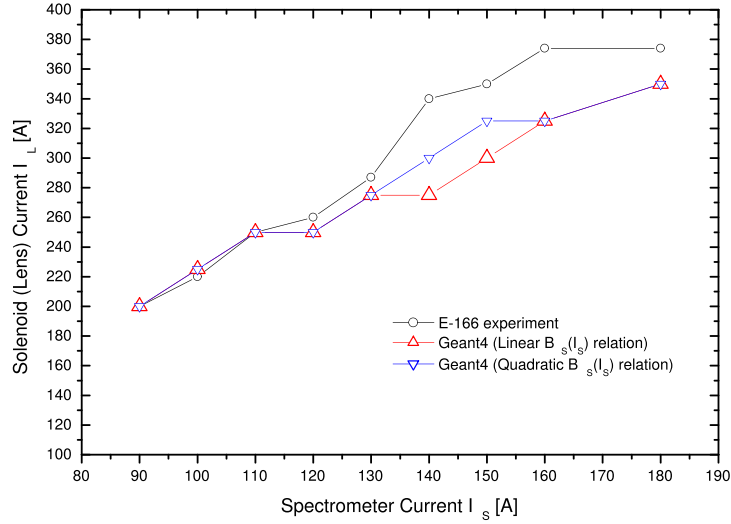


Figure 4.13: Solenoid current for which the e^+ yield at the PosSi counter is maximum for different spectrometer currents. Comparison between simulation (linear and quadratic approaches) with experimental data.

recorded at the PosSi counter and $N_{Tr}^{e^+}$ the total number of positrons emitted at the conversion target. The results on the transmission are listed in Table 4.6 for different spectrometer currents.

The yield at the PosSi counter in units of positrons per undulator gamma is derived $F_{PosSi}^{e^+}[e^+/\gamma] = T_{PosSi}^{e^+} Y_{e^+}^{4\pi}$ and is compared to the measured flux in Fig. 4.14. $T_{PosSi}^{e^+}$ is the transmission and $Y_{e^+}^{4\pi}$ the positron yield at the conversion target given by equation 4.8

4.5.2 Momentum-Current relation of the spectrometer

The transport system, guides the positrons from the conversion target to the polarimeter section in a selective way. At the reconversion target, the energy distribution of the transmitted positrons depends strongly on the spectrometer magnetic field. The magnetic spectrometer was operated at five different currents (100, 120, 140, 160 and 180 A), selecting five different positron momenta. A direct energy measurement of the positron beam during the transport was not possible. A detailed simulation of the transport system has to resolve the Momentum-Current relation by deriving the mean

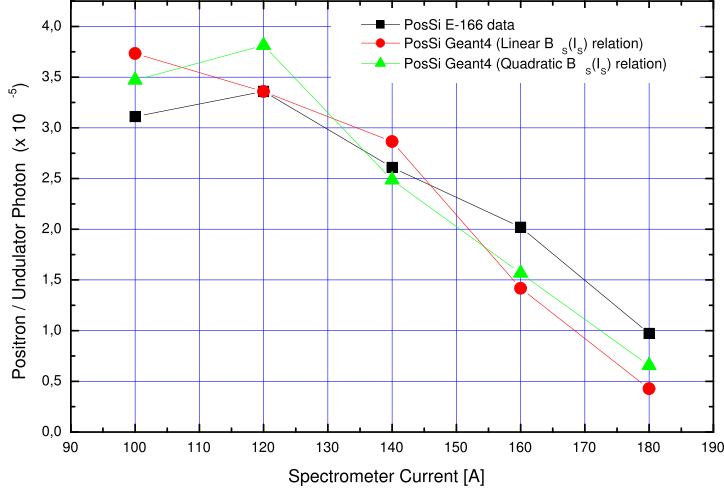


Figure 4.14: The positron yield at the PosSi counter for different spectrometer current compared to the measured flux.

energy (momentum) of the positron beam reaching the reconversion target for different spectrometer currents.

In the simulation of the e^+ transport, the energy distribution of the positron beam is recorded at the PosSi counter and at the reconversion target (see Fig. 4.15) for the five setting point listed in Table 4.7.

A comparison of the simulation results with a test experiment discussed in Section 2.3.1 shows consistency as illustrated in Fig. 4.17.

4.5.3 Positron spatial distribution

In addition to the energy distribution discussed in Section 4.5.2, the knowledge of the positron spatial distribution at the reconversion target is crucial for the polarimeter section. In a preliminary study discussed in the E-166 proposal [G. Alexander(2003)], the positron beam at the reconversion target was assumed to be a pencil beam, well centered with a normal incidence on the reconversion target. But in the simulation a more realistic positron spatial distribution is computed. The distribution at the PosSi counter and at the reconversion target has a half-moon shape as shown in Fig. 4.18. The x and y distributions at the exit of the spectrometer vacuum chamber, at the PosSi counter and at the reconversion target are shown in Fig. 4.19.

At the PosSi counter, the positron beam is offset to the left side. The

I_S	E-166 Data I_L	Geant4 I_L	E-166 Data (Yield)	Geant4 (Yield)	Geant4 (Transmission)
[A]	[A]	[A]	$10^{-5}[e^+/\gamma]$	$10^{-5}[e^+/\gamma]$	[%]
100	220	225	3.11	3.4704	0.40
120	260	250	3.36	3.8136	0.44
140	340	300	2.61	2.4863	0.29
160	374	325	2.02	1.5670	0.18
180	374	350	0.97	0.6561	0.07

Table 4.6: Expected e^+ yield at the PosSi counter and transmission through the spectrometer compared to the measured yield.

I_S	I_L	Geant4	Test 48A
[A]	[A]	E_{e^+} [MeV/c]	E_{e^+} [MeV/c]
100	225	4.56	4.78
120	250	5.33	5.56
140	300	6.04	6.31
160	325	6.70	7.01
180	350	7.33	7.67

Table 4.7: Position momentum as a function of the spectrometer current. Comparison between Geant4 simulation and experimental calibration using the ^{90}Sr beta source in column (Test 48A).

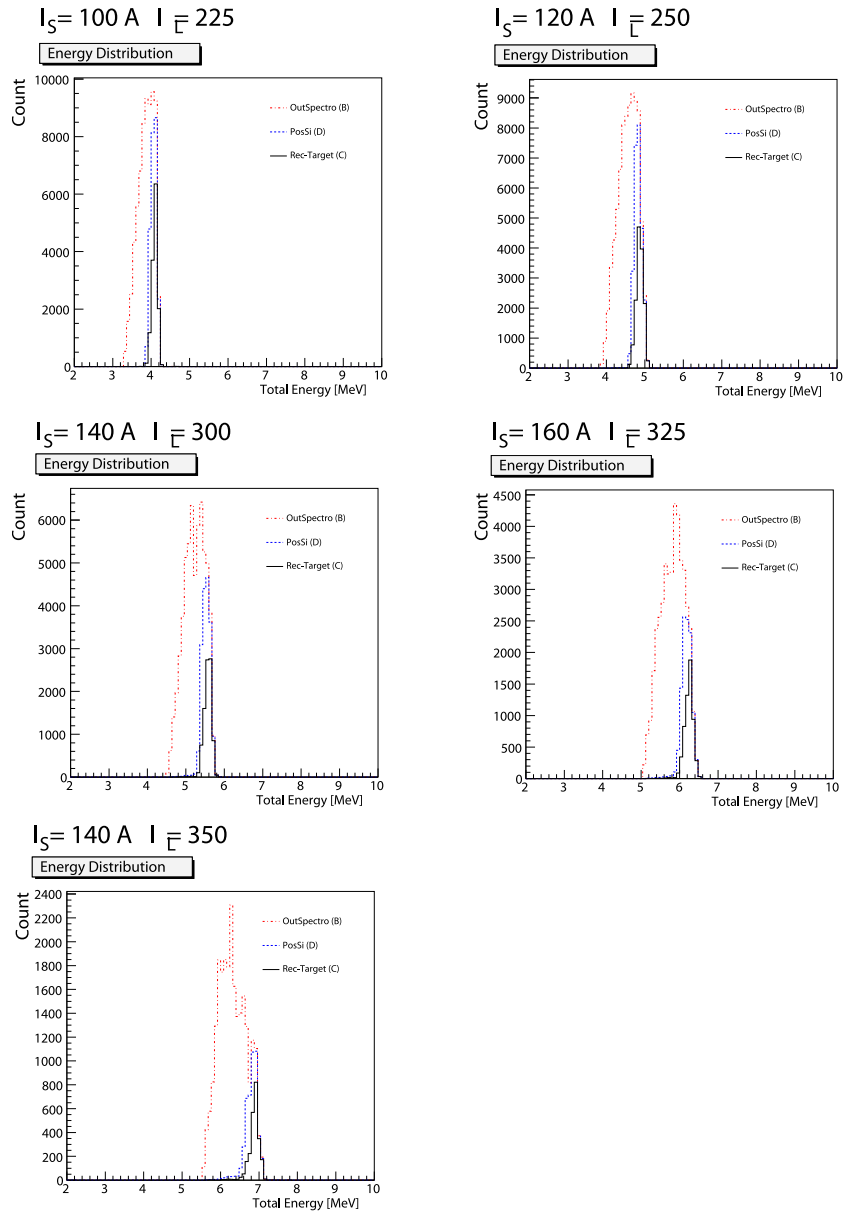


Figure 4.15: Positron energy distribution at the PosSi counter and at the reconversion target for different setting points.

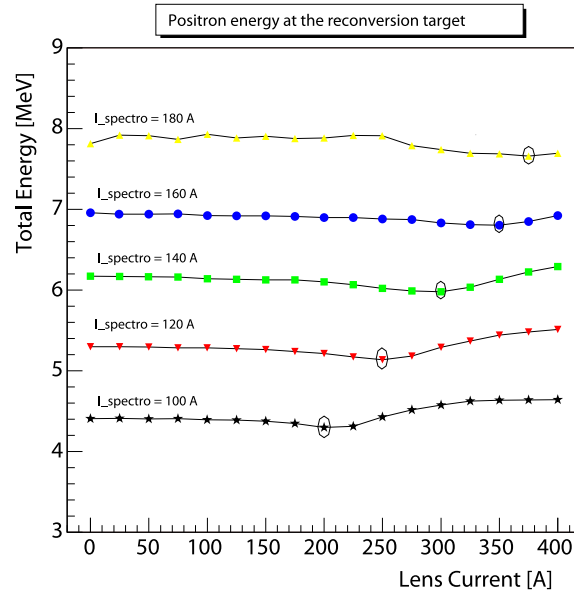


Figure 4.16: Mean positron energy at the reconversion target versus the solenoid current. The points with small circles stand for the setting points.

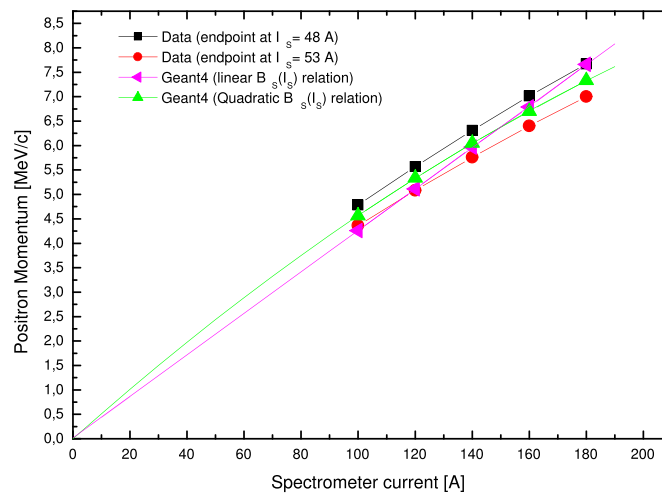


Figure 4.17: Spectrometer calibration. Comparison between Geant4 simulation and experimental calibration using a ^{90}Sr beta source (test experiment discussed in Section 2.3.1).

shape is characterized by a sharp vertical edge. A detailed investigation [Laihem(2006a)] has been performed to understand the origin of the edge and the half-moon shape. The positron beam is cut off when it passes through the spectrometer jaw reducing the round shape to a half-moon. Due to this offset – The weak point in the spectrometer– the loss of positrons in the exit pipe is 87.5%. Only 12.5% from the total number of positrons emerging from the spectrometer to the exit pipe reach the reconversion target. The rest are simply stopped inside of the exit pipe.

4.6 The Positron Polarimeter

4.6.1 Setup of the E166 positron Polarimeter

The positron polarimeter consists of the reconversion target, the analyzing magnet, and the CsI(Tl) calorimeter (see Fig. 4.20). In the simulation study initially an ideal monoenergetic pencil beam without angular divergence going directly to the center of the reconversion target was used. This is called in what follow the ideal beam configuration. In a second study a more realistic positron beam as predicted by the simulation of the transport system is used with its energy, spatial and angular distributions. This is called in what follow the realistic beam configuration.

4.6.2 The analyzing power

To derive the analyzing power the positron polarization was set to 1 as well as the absolute polarization of electrons in the iron absorber. The use of maximum polarization improves the statistical significance of the simulation and can be scaled to real values. In both the ideal and realistic beam configurations, the asymmetry δ in the transmitted signal for each of the nine crystals is recorded when reversing the magnet polarity.

The asymmetry δ is defined by:

$$\delta = \frac{E^- - E^+}{E^- + E^+}, \quad (4.20)$$

with $E^{-(+)}$ the mean energy of the transmitted signal deposited in a single crystal. The statistical error on the asymmetry is given by:

$$\Delta\delta = \frac{2}{(E^- + E^+)^2} \cdot \sqrt{(E^+ \Delta E^-)^2 + (E^- \Delta E^+)^2}, \quad (4.21)$$

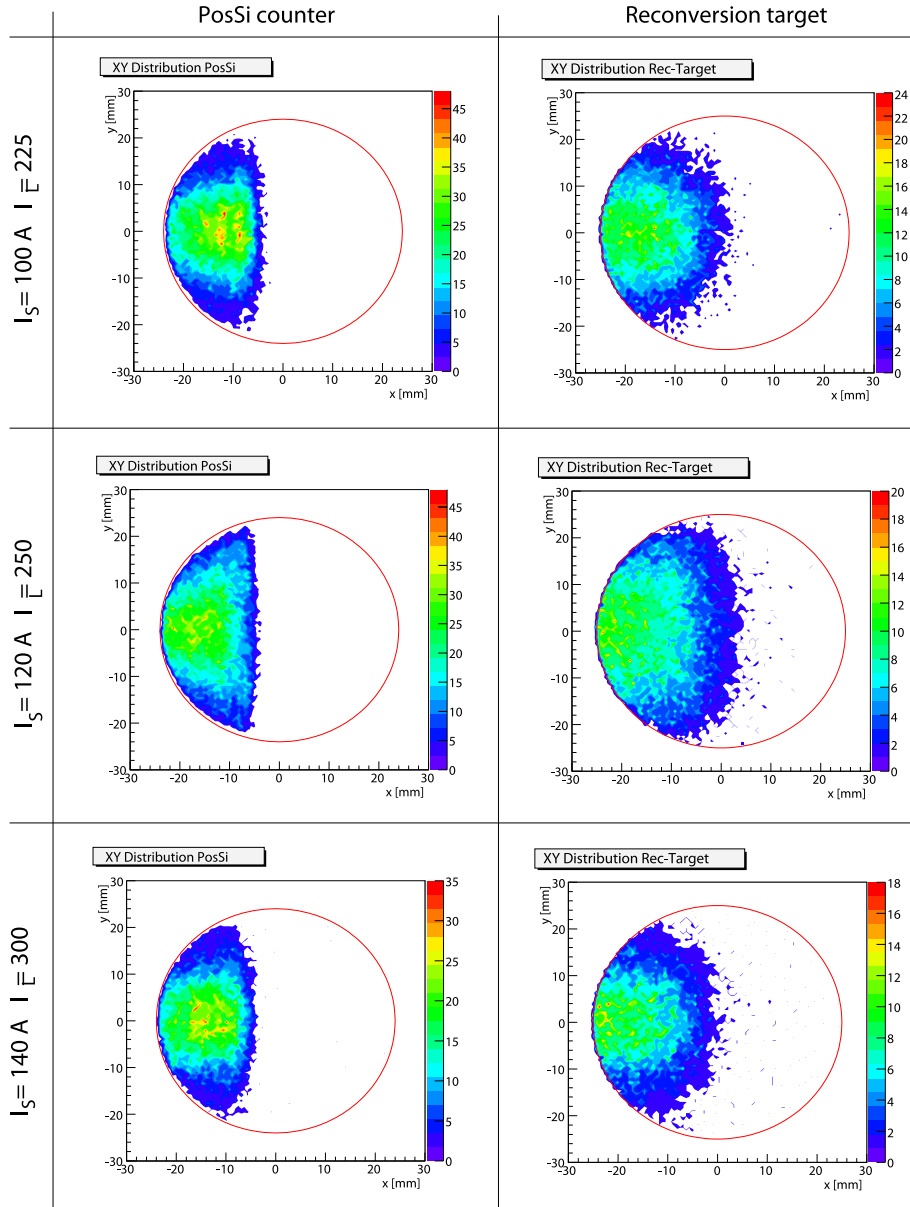


Figure 4.18: The positron spatial distributions at the PosSi counter in the left column and at the reconversion target in the right column for spectrometer currents 100, 120, 140 A.

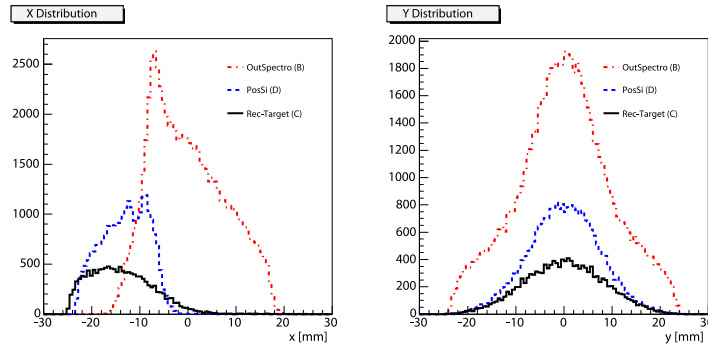
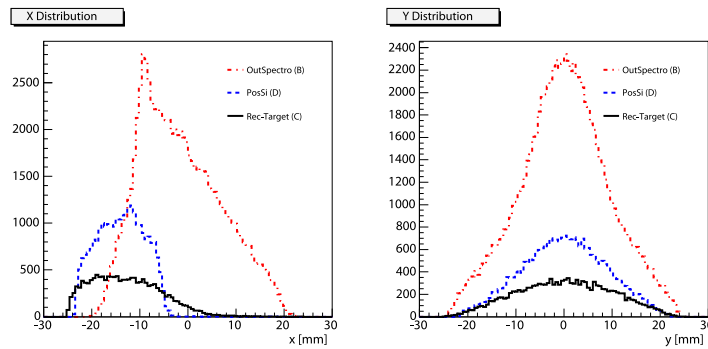
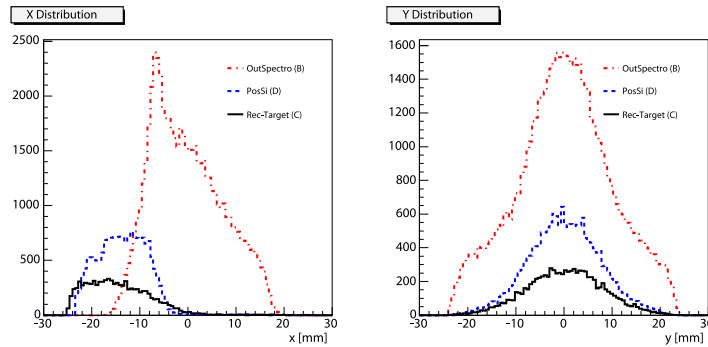
$I_S = 100 \text{ A} \quad I_{\bar{e}} = 225$

 $I_S = 120 \text{ A} \quad I_{\bar{e}} = 250$

 $I_S = 140 \text{ A} \quad I_{\bar{e}} = 300$


Figure 4.19: The positron X and Y distribution at the exit window of the vacuum chamber, at PosSi counter and at the reconversion target for different spectrometer currents 100, 120, 140 A.

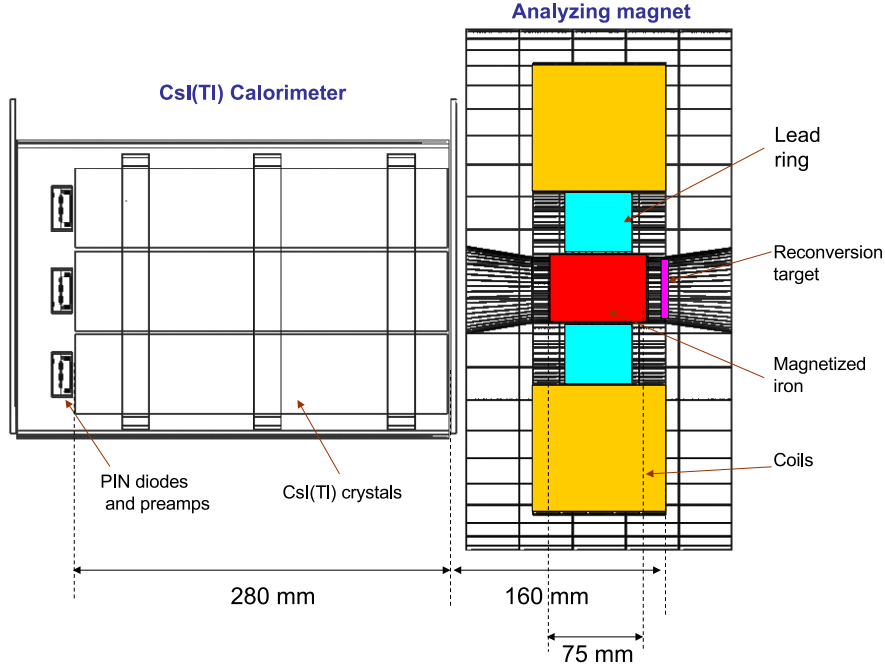


Figure 4.20: Side view of the E166 positron polarimeter

where the error $\Delta E^{-(+)}$ of the mean value $E^{-(+)}$ is calculated by:

$$\Delta E^{-(+)} = \frac{RMS^{-(+)}}{\sqrt{N}}, \quad (4.22)$$

with N the number of positron (electron) bunches sent to the reconversion target.

The relevant parameters used in the Geant4 simulation of the polarimeter are listed in Table 4.8. For the ideal beam configuration the positron energy used in the simulation are listed in Table 4.7 for different setting points and for the realistic beam configuration the energy distributions at the reconversion target shown in Fig. 4.15 were used.

With a maximum polarization of the positrons (+1) and for the magnetized absorber (± 1) the recorded asymmetry in the CsI(Tl) calorimeter gives directly the value of the analyzing power. The analyzing power is calculated as:

$$A_{e^+} = \frac{\delta}{P_{e^+} P_{e^-}} \quad (4.23)$$

where A_{e^+} , P_{e^+} and P_{e^-} are the positron (electron) analyzing power, the positron (electron) longitudinal polarization and the iron polarization.

Particle	$e^+(e^-)$
Number of particle per bunch	$4 \cdot 10^4$
number of bunches	$5 \cdot 10^5$
particle polarization	-1
iron polarization	± 1

Table 4.8: Particle and beam parameters used in the simulation of the positron (electron) polarimeter.

Ideal e^+ beam configuration

In this ideal configuration the analyzing power and asymmetries will be maximal and constitute an upper limit. Any deviation from this ideal case like an energy or angular spread will dilute the asymmetry and thus decreases the analyzing power. Figure 4.21 shows the recorded signal in the nine crystals of the CsI(Tl) calorimeter for positive and negative magnet polarity. In this figure, the positron polarization was set to -1. The analyzing power in the ideal case as a function of the $e^+(e^-)$ energy is shown in Fig. 4.22. It shows that for a given energy, the analyzing power for positrons is higher as for electrons. This difference is mainly due to the annihilation process which is only present for positrons.

Realistic e^+ beam configuration

In this second approach a realistic beam at the reconversion target was used. The beam parameters are described by the energy and the spatial distributions as shown in Fig. 4.15 and 4.19, respectively. The analyzing power is calculated for the five setting points and shows slightly lower values if compared to the ideal case as shown in Fig. 4.23. In Fig. 4.24 the positron analyzing power is compared to the electron analyzing power for the realistic beam parameters.

The positron analyzing power for an ideal and realistic beam configurations are compared in Table 4.9 together with their statistical errors. Table 4.10 shows a comparison between the positron and electron analyzing power both derived from a realistic beam at the reconversion target. The analyzing power for positrons and electrons for the nine crystals and for the CsI(Tl) calorimeter are summarized in Tables 4.11 and 4.12 respectively.

$I_S[A]$	$E^{e^+}[\text{MeV}/c]$	$A_{e^+} \pm \Delta A_{e^+}$ pencil beam	$A_{e^+} \pm \Delta A_{e^+}$ realistic beam
100	4.56	0.1578 ± 0.0024	0.1498 ± 0.0016
120	5.33	0.1646 ± 0.0023	0.1563 ± 0.0015
140	6.04	0.1687 ± 0.0021	0.1616 ± 0.0014
160	6.70	0.1693 ± 0.0020	0.1651 ± 0.0013
180	7.33	0.1683 ± 0.0019	0.1686 ± 0.0013

Table 4.9: The analyzing power in the central crystal for different setting points. Comparison between pencil beam and realistic beam at the reconversion target.

$I_S[A]$	$E^{e^+}[\text{MeV}/c]$	$A_{e^+} \pm \Delta A_{e^+}$ positrons e^+ realistic beam	$A_{e^-} \pm \Delta A_{e^-}$ electrons e^- realistic beam
100	4.56	0.1498 ± 0.0016	0.1371 ± 0.0018
120	5.33	0.1563 ± 0.0015	0.1417 ± 0.0016
140	6.04	0.1616 ± 0.0014	0.1469 ± 0.0015
160	6.70	0.1651 ± 0.0013	0.1528 ± 0.0014
180	7.33	0.1686 ± 0.0013	0.1557 ± 0.0014

Table 4.10: The analyzing power in the central crystal for different setting points. Comparison between positrons and electrons for a realistic beam configuration at the reconversion target.

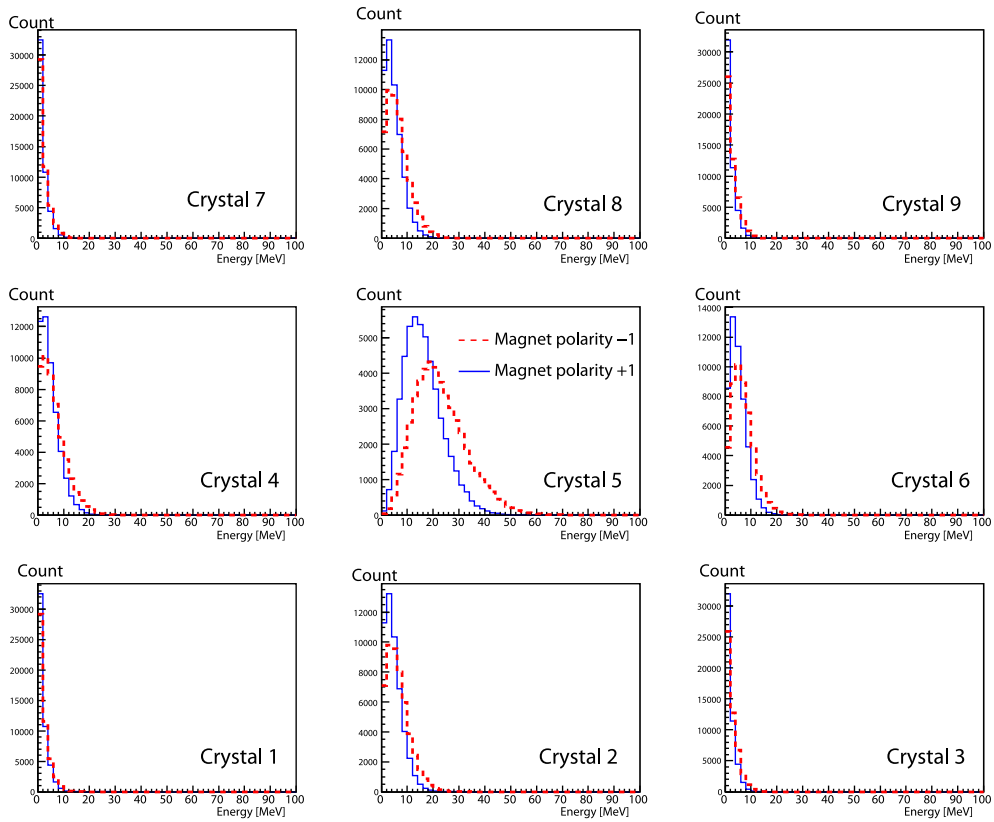


Figure 4.21: The positron signal in the nine crystals of the CsI(Tl) calorimeter recorded for two opposite magnet polarities (+1 and -1). In this figure, the positron polarization was set to -1.

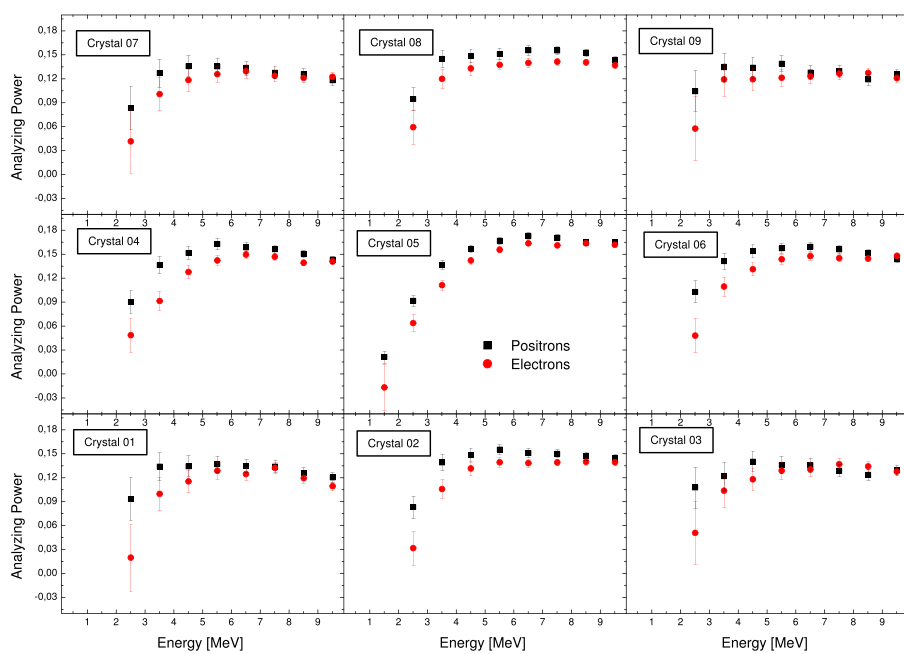


Figure 4.22: Positron and electron analyzing powers: Monoenergetic pencil beam centered at the reconversion target

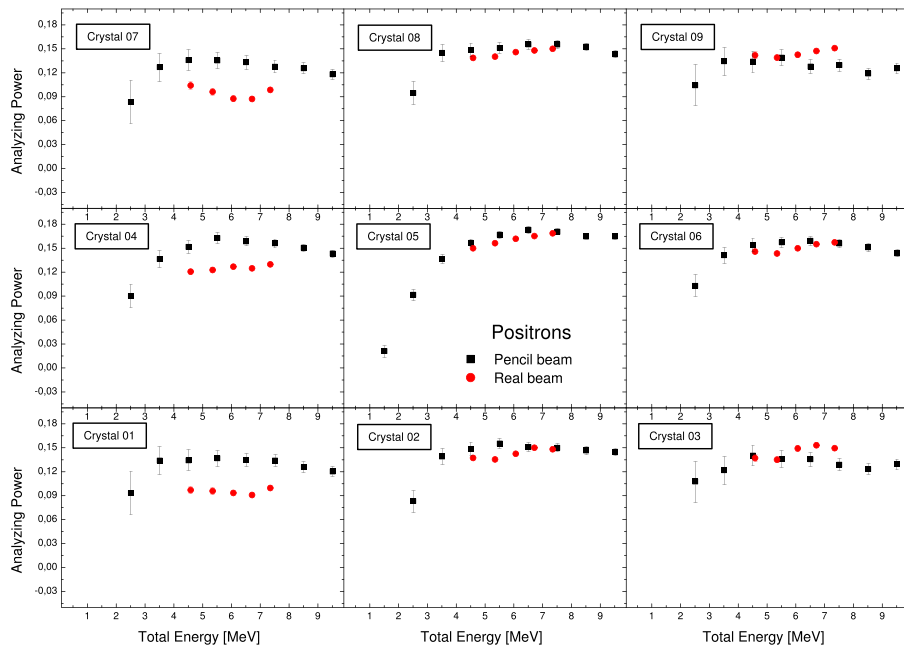


Figure 4.23: Analyzing power for positrons: comparison between ideal and realistic beam configuration

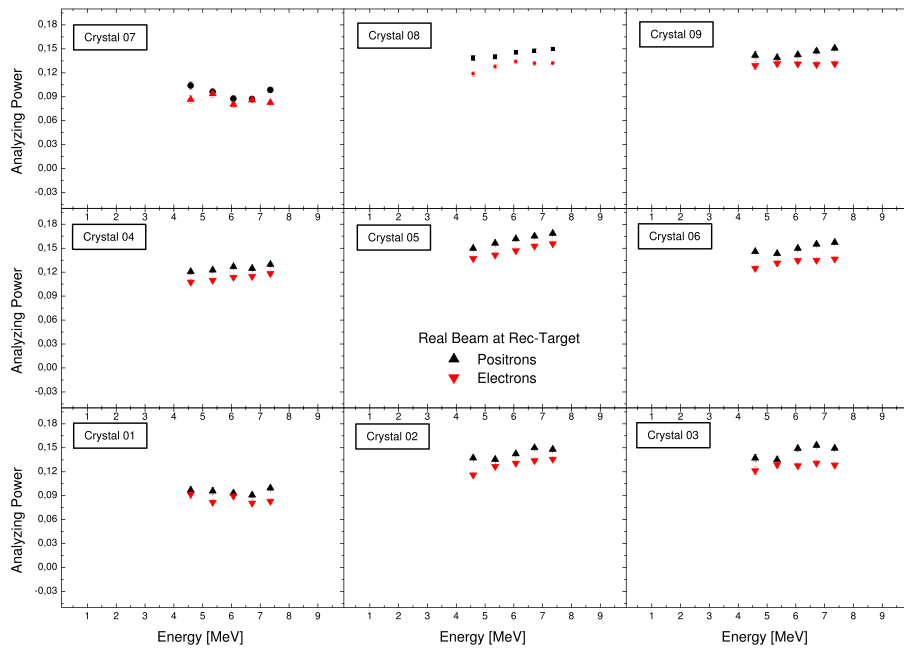


Figure 4.24: Positron and electron analyzing power: in the realistic beam configuration at the reconversion target

I_s	Crystal 01	Crystal 02	Crystal 03	Crystal 04	Crystal 05	Crystal 06
100	0.0969±0.0046	0.1372±0.0028	0.1369±0.0042	0.1205±0.0030	0.1498±0.0016	0.1457±0.0025
120	0.0956 ±0.0040	0.1351±0.0025	0.1349±0.0036	0.1226±0.0027	0.1563±0.0015	0.1434±0.0022
140	0.0933±0.0035	0.1422±0.0023	0.1489±0.0033	0.1266 ±0.0025	0.1616±0.0014	0.1499±0.0021
160	0.0907±0.0032	0.1499±0.0021	0.1530±0.0029	0.1245±0.0023	0.1651±0.0013	0.1550±0.0019
180	0.0994±0.0029	0.1479±0.0020	0.1494±0.0027	0.1296±0.0022	0.1686±0.0013	0.1573±0.0018

I_s	Crystal 07	Crystal 08	Crystal 09	Full CsI(Tl)
100	0.1039±0.0046	0.1385±0.0028	0.1418±0.00425	0.1390±0.00123
120	0.0959±0.0039	0.1400±0.00254	0.1389±0.0037	0.1407±0.0011
140	0.0873±0.0036	0.1457±0.0023	0.1424±0.0033	0.1455±0.0011
160	0.0870±0.0032	0.1477 ±0.0021	0.1470±0.0030	0.1484±0.0011
180	0.0984±0.0029	0.1499±0.0020	0.1507±0.0027	0.1514±0.0011

Table 4.11: The analyzing power for the positron signal in the single crystals and the full calorimeter for different spectrometer currents.

I_S	Crystal 01	Crystal 02	Crystal 03	Crystal 04	Crystal 05	Crystal 06
100	0.0917±0.0049	0.1160±0.0030	0.1213±0.0046	0.1075±0.0032	0.1371±0.0018	0.1249±0.0028
120	0.0816±0.0040	0.1266±0.0026	0.1287±0.0038	0.1097±0.0028	0.1417±0.0016	0.1315±0.0024
140	0.0894±0.0036	0.1308±0.0023	0.1274±0.0034	0.1135±0.0026	0.1469±0.0015	0.1347±0.0021
160	0.0806±0.0032	0.1338±0.0022	0.1307±0.0030	0.1147±0.0023	0.1528±0.0014	0.1350±0.0020
180	0.0829±0.0029	0.1358±0.0020	0.1283±0.0028	0.1182±0.0022	0.1557±0.0014	0.1365±0.0019

I_S	Crystal 07	Crystal 08	Crystal 09	Full CsI(Tl)
100	0.0865±0.0049	0.1187±0.0030	0.1290±0.0046	0.1236±0.0013
120	0.0936±0.0041	0.1276±0.0026	0.1314±0.0038	0.1286±0.0012
140	0.0804±0.0036	0.1338±0.0024	0.1312±0.0034	0.1320±0.0012
160	0.0858±0.0032	0.1318±0.0022	0.1304±0.0030	0.1345±0.0011
180	0.0825±0.0029	0.1320±0.0021	0.1313±0.0028	0.1363±0.0011

Table 4.12: The analyzing power for the electron signal in the single crystals and the full calorimeter for different spectrometer currents.

4.6.3 The expected asymmetries

With the positron (electron) polarization from the target (see Section 4.3.2) and the analyzing power determined in the previous section one can now predict the asymmetries one expect to measure in the CsI(Tl) calorimeter. Figure 4.25 shows the polarization profile of the positrons (electrons) produced at the conversion target and the corresponding analyzing power in the energy range between 2 and 9.5 MeV.

The expected asymmetries for ideal beam and realistic beams are shown in Fig. 4.26. They are calculated as:

$$\delta = A_{e^+}P_{e^+}P_{e^-} \quad (4.24)$$

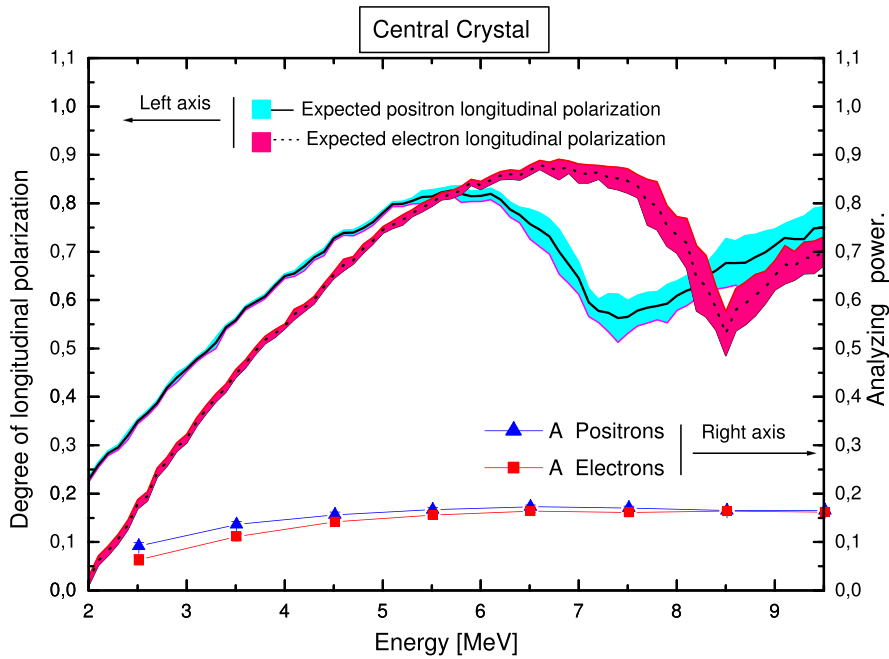


Figure 4.25: The expected positron/electron polarization at the target (left scale) and the analyzing power (right scale) versus energy (Full simulation).

In the next chapter we discuss the data analysis and compare to the expected asymmetries described here.

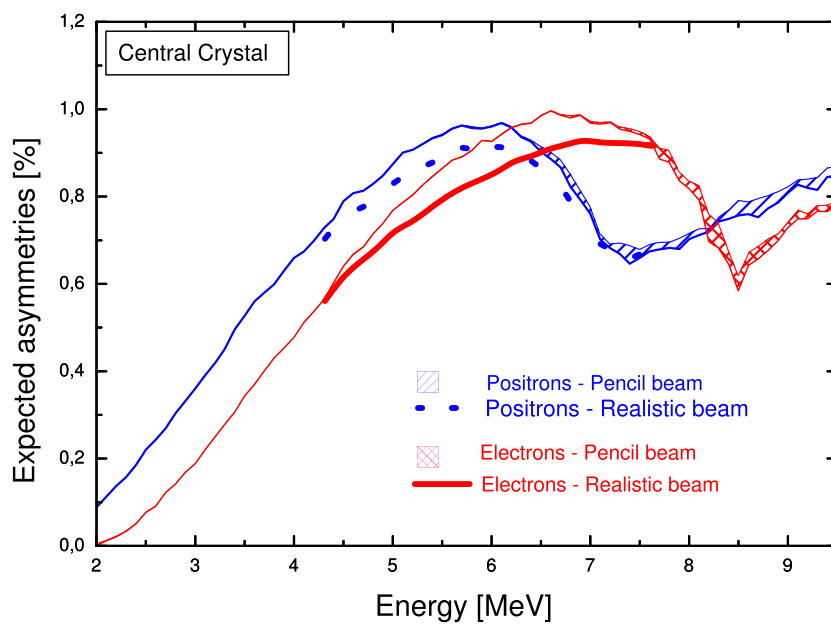


Figure 4.26: Predicted asymmetries for positron and electrons in the case of ideal beam and realistic beam.

Chapter 5

Analysis, Results and Discussion.

The E-166 data runs took place at SLAC in 2005. The analysis of the recorded data is a common effort of the collaboration. It is still ongoing. There are still a few systematic problems that are not fully solved. The current status is summarized here. In this chapter, we will focus on the analysis of the CsI(Tl) data to which we contributed directly.

5.1 Data structures

In the following the structure of the data recorded by E-166 is described introducing the internal nomenclature.

Undulator ON: For these events the undulator pulse is in phase with the electron beam. The precise timing was adjusted to the beam current measurement with a toroidal pickup coil. In this configuration, undulator photons are generated. The signal in all detectors are recorded with a trigger number 36864. It consist of **signal plus background** \equiv **sb**. For simplicity, the undulator ON events are called in the following signal events referred to as **sb**.

Undulator OFF: In the undulator OFF configuration, the undulator was pulsed out of time with the electron beam, usually 15 ms before the passage of the electron bunch. In this configuration, no undulator photons are generated. The detectors record background created by the electron beam. No background from the photon beam is present.

These events will be called **background** \equiv **b**. The trigger number 36896 is assigned to this data.

Magnet polarity: In the experiment the iron core of the analyzing magnet was magnetized to saturation with an electrical current of ± 60 A through the magnet coils. The direction of the longitudinal magnetic field B_z was checked with a Hall probe close to the iron core. For $+60$ A the direction of B_z was opposite to the electron beam (positive polarity) and for -60 A, B_z had the same direction as the electron beam (negative polarity). See Fig. 5.2. In what follows, the signs $+$ and $-$ correspond to $+60$ A and -60 A, respectively.

A cycle: A cycle consists of a set of 3000 beam pulses alternating between undulator ON and OFF for a given magnet polarity. In one cycle half of the events (pulses) are background **b** and the other half are signal plus background events **sb**

Super-runs: A super-run consists of 10 cycles. The magnet polarity for both photon and positron polarimeters was reversed automatically between the cycles in a 30 seconds break. During a super-run the spectrometer current was unchanged, so that a super-run refers to a fixed positron (electron) momentum. For each spectrometer setting, several super-runs are taken. Each super-run is identified by a unique run number. The structure of a super-run is illustrated in Fig. 5.1.

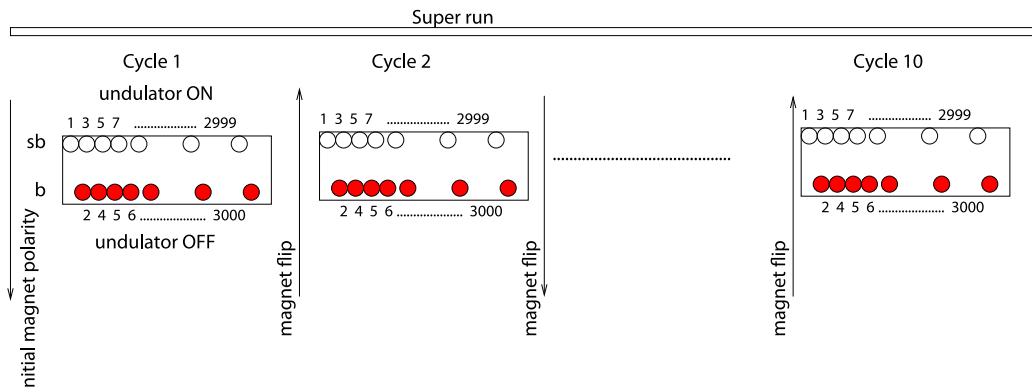


Figure 5.1: Data structure of a super-runs.

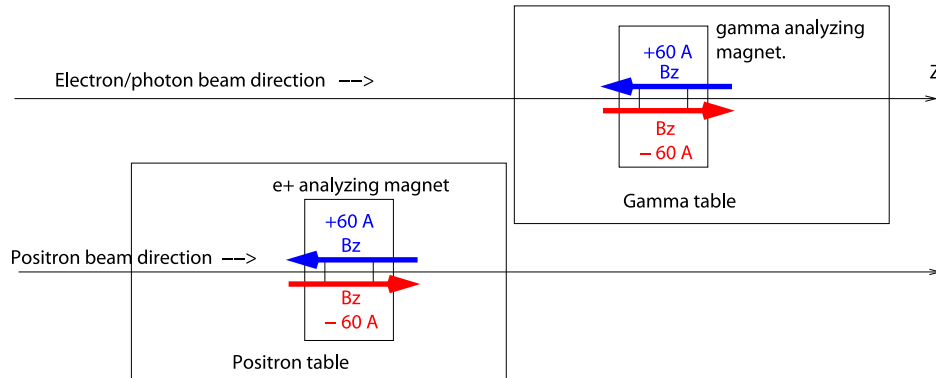


Figure 5.2: Direction of magnetization of the iron core for the positron and photon polarimeter at ± 60 A.

5.2 Analysis Procedure

5.2.1 Analysis strategy

The general analysis structure for one super-run is the following:

- Reject events with unstable beam or background conditions. Whole consecutive cycles are rejected, if they contain too many unstable events.
- The signal from the central crystal of the CsI(Tl) calorimeter is extracted and normalized to the beam current measured by the toroid.
- The background from the undulator OFF events is subtracted from the signal (undulator ON events) on an event by event basis.
- For each cycle the background corrected energy in the central crystal is histogrammed. The mean value and its error is determined from a Gaussian fit.
- The asymmetry between consecutive cycles with opposite magnet polarity is determined.
- For each spectrometer setting (positron momentum) the asymmetries from all accepted pairs of cycles are averaged.
- The asymmetry is translated into a positron polarization with the analyzing power derived from the Monte Carlo simulation.

5.2.2 Data selection

The main goal of the analysis is to determine the asymmetry in the photon signal transmitted through the magnetized iron core. This asymmetry should be related mainly to the polarized Compton scattering. But experimentally many artifacts may contribute to false asymmetries. The expected asymmetry derived from the simulation is less than 1%. Thus, it is very important to ensure stable experimental conditions for adjacent cycles.

The most important aspects are:

- 1) The iron core should be magnetized up to saturation in both polarities.
- 2) A similar electron beam current. The positron yield depends on the undulator photon flux which is directly related to the beam current.
- 4) A similar positron flux reaching the reconversion target. The positron transport system with its complex field may interfere with the analyzing magnet's fringe field. The interference may change when flipping the magnet polarity and may induce a false asymmetry. This point is discussed in detail later on.
- 3) Similar positron energy (momentum) reaching the reconversion target. The spectrometer current defines the positron momentum and should be kept to the same value for adjacent cycles.
- 5) A similar background conditions. The criteria on the background conditions is based on a specific background detector called pCal (discussed in section 2.6).

In the analysis pairs of adjacent cycles with opposite magnet polarity are selected on the basis of stability in the beam current and background conditions. The selection is based on the toroid signal which measure the electron beam current and the pCal detector which is sensitive to the background conditions.

Toroid signal based selection

The selection procedure and event rejection is done in three steps:

Cycle selection: In first step, the beam current (toroid signal) is histogrammed for a pair of adjacent cycles for all super-runs of a given spectrometer setting. Only cycles with a narrow Gaussian distribution of the beam current are accepted (Fig. 5.3).

Pair of adjacent cycles: As described in 5.2.1 The super-runs are divided into pairs of adjacent cycles. Whole pairs are rejected if one of the cycles failed the previous condition.

Clean-up: Finally individual events (pulses) are rejected if the beam current is more than 3σ away from its mean value during one cycle. Table 5.1 lists selected event samples used in the analysis for the different spectrometer settings.

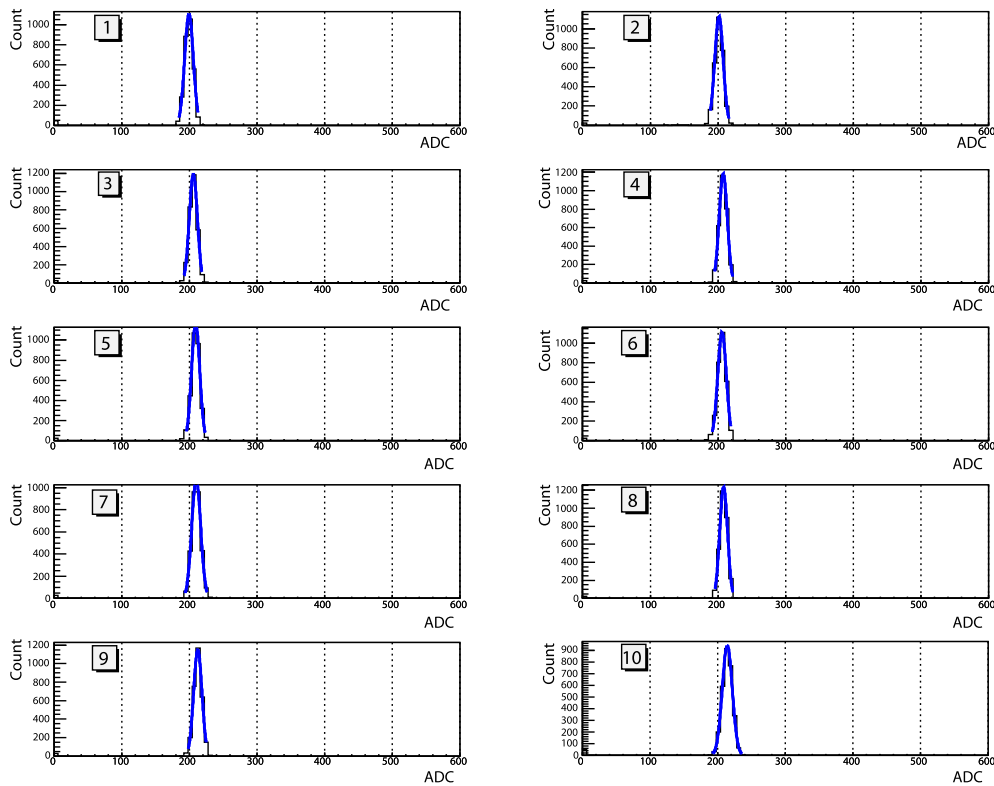


Figure 5.3: The toroid signal recorded in ten cycles of a super-run.

pCal signal based selection

The same procedure is applied to the pCal signal to reject events with abnormal backgrounds. Figures 5.4 and 5.5, shows the pCal signal recorded in ten cycles of a super-run.

The remaining pairs of cycles are then stored for further analysis.

I_{spec} [A]	I_{lens} [A]	Analyzed	$E(e^\pm)$ [MeV]	run mode	number of events [10^3]
100	220	Yes	4.59	e^+	1240
120	260	Yes	5.36	e^+	1119
140	340	Yes	6.07	e^+ (1)	1422
140	340	No	6.07	e^+ (2)	1320
160	360	Yes	6.72	e^+	1014
160	360	Yes	6.72	e^-	870
180	374	Yes	7.35	e^+	390
180	374	No	7.35	e^+ (ff)	624

Table 5.1: List of event samples used for the different spectrometer settings with the corresponding number of events before and after the selection used in the analysis to determine the asymmetry for the central crystal. The two data sets at 140 A were taken in the first and second run period, respectively, the label 'ff' indicates the data set for which the undulator was run with ferro-fluid for cooling.

5.2.3 Background subtraction

The dominating background in E-166 is believed to be a soft background due to bremsstrahlung photons produced when a small fraction of the electron beam scrapes the tungsten collimator at the entrance of the undulator (Fig. 2.3).

The background is visible in Fig. 5.6 in the CsI(Tl) calorimeter for the undulator OFF configurations. We continuously tried to minimize the background by steering the beam and aligning the undulator table.

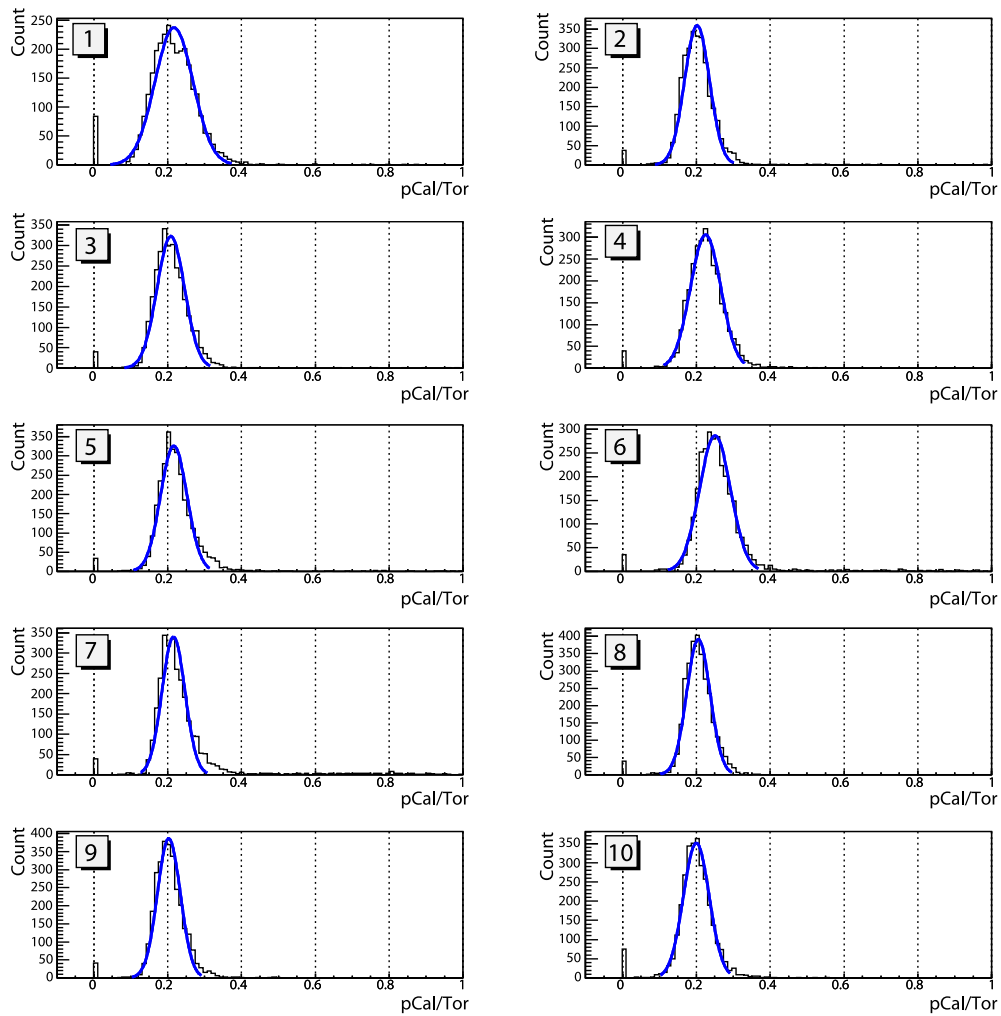


Figure 5.4: Example of a good background conditions. The pCal signal recorded during ten consecutive cycles of a super-run. In this case no cycle has been rejected.

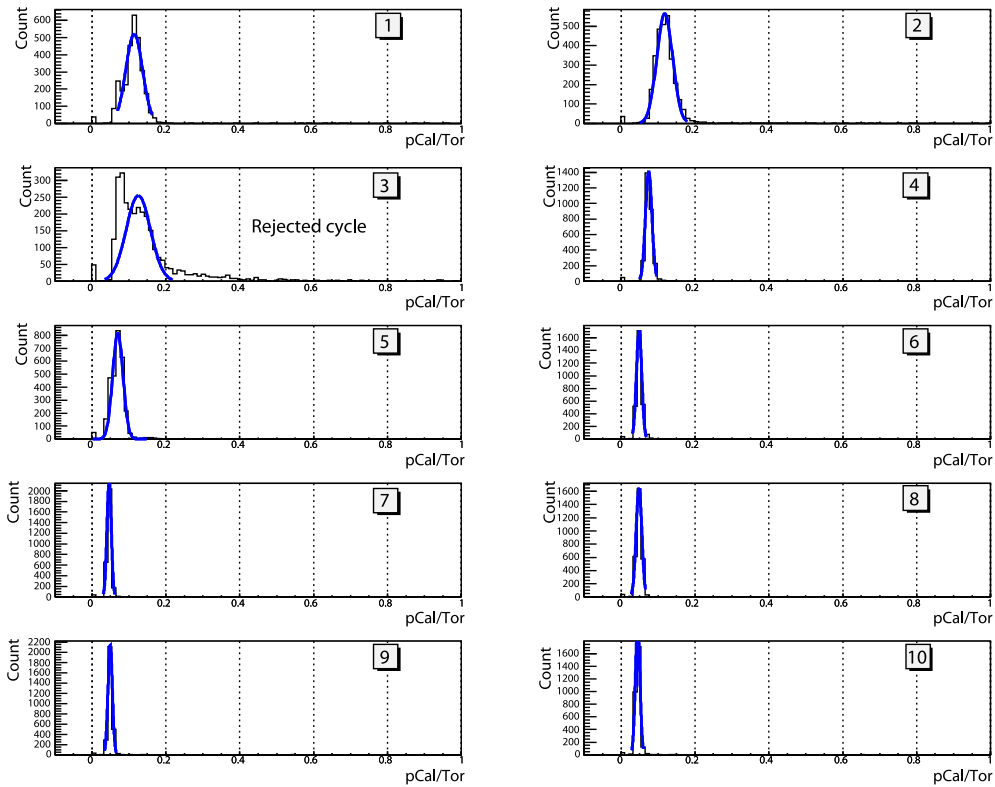


Figure 5.5: Example of unstable background conditions during one super-run. The pCal signal recorded during ten consecutive cycles. In this case the first three cycle pairs have been rejected.

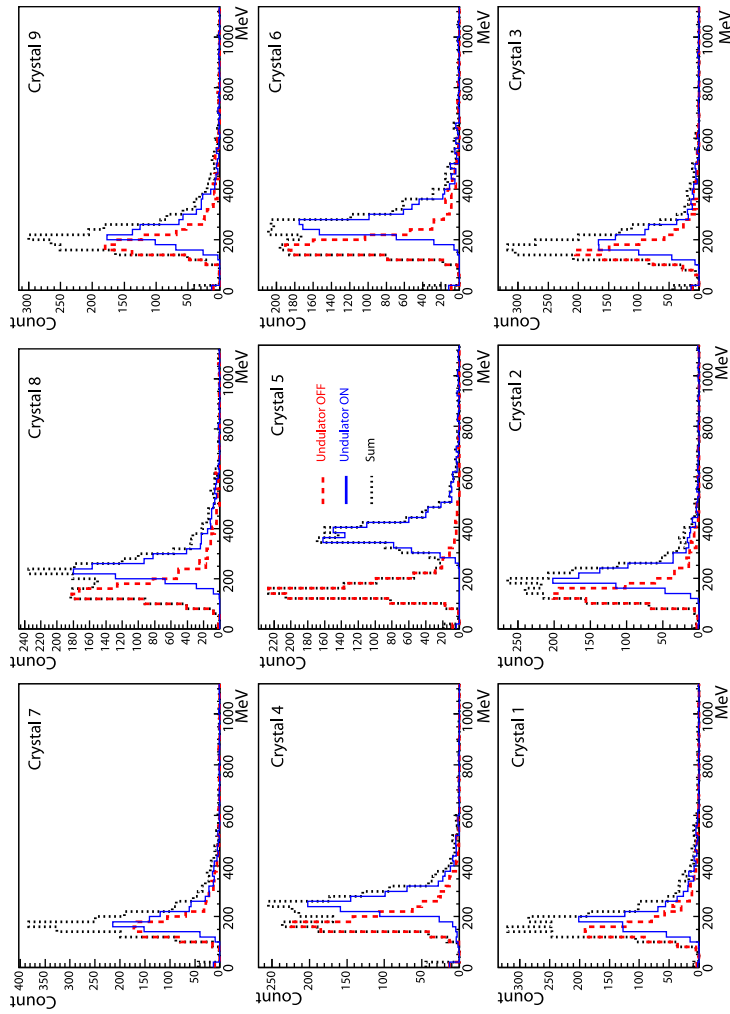


Figure 5.6: Background and positron signal events recorded in the CsI(Tl) calorimeter in the nine crystals. The undulator OFF stands for background events and undulator ON for background+signal events.

In the analysis, we focused on the signal in the central crystal (crystal 5). Several procedures have been investigated to subtract the background which contaminates the positron signal in the CsI(Tl) calorimeter. Two methods A and B are described in this section and for references we also quote method C and D developed by A. Schäliker [A. Schälicke(2005), R. Dollan(2005)] and the Tel-Aviv group [Alexander and Reinherz-Aronis(2005)], respectively.

Mathematically the extracted mean energy from all methods described below are equivalent. However depending on the Gaussian fit and mainly the truncated fit in the peak region, the mean value derived from the fit may differ from one method to an other.

Method A and B

In one cycle, background events and signal events are alternatively recorded with a rate of 10 Hz. The idea of method A is to subtract from the deposited energy of each signal event \mathbf{sb}_i the following background event \mathbf{b}_{i+1} (see Fig. 5.8). Both events are normalized to the beam current (toroid signal) before subtraction. The distribution obtained has a Gaussian core and relatively long tails to both sides (see Fig. 5.7). The tails were truncated. The truncation was optimized with respect to stability and statistical accuracy of the mean value of the signals in the core region. The energy normalized to the beam current is histogrammed and the mean value and its error are extracted from a Gaussian fit within a 2σ range (Fig. 5.7). The mean energy can be written as:

$$E_A = \frac{1}{n} \sum_{i=1}^n (sb_i - b_{i+1}) \quad (5.1)$$

where sb_i is a signal event (signal + background), b_{i+1} is the following background event and n the number of pairs (sb_i, b_{i+1}).

Method B is similar to method A. But now the previous background event is subtracted from the signal and not the following as illustrated in Fig. 5.8. Similarly, the mean energy can be written as:

$$E_B = \frac{1}{n} \sum_{i=1}^n (sb_{i+1} - b_i) \quad (5.2)$$

The resulting energy distribution from these two similar methods do affect the asymmetry. There are large event-to-event fluctuations both in background and signal events within a cycle. This causes a large signal spread for background subtracted events. No short-range correlations in time, in particular no correlations in sequential signal and background events, have been observed.

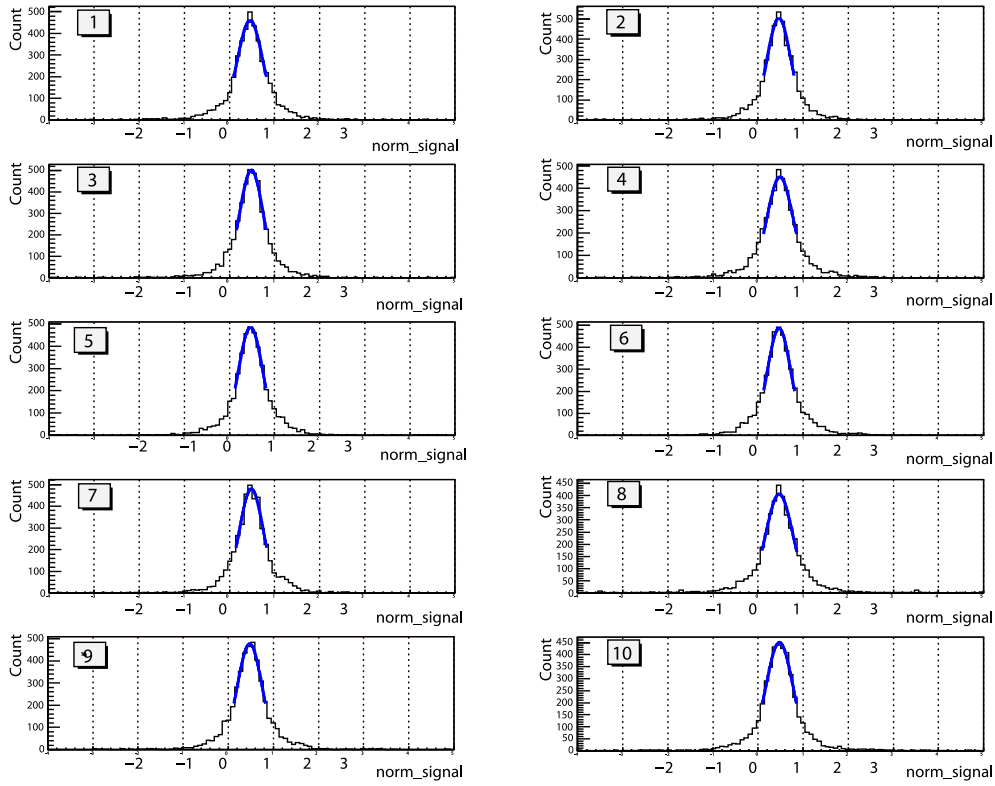


Figure 5.7: Background subtracted positron signal distribution (normalized to the toroid signal) for the central crystal recorded in ten consecutive cycles. Example of a good super-run (the distributions are fitted with a Gaussian in a 2σ range).

Method C

For reference method C [Alexander and Reinherz-Aronis(2005)], is included. There signal subtracted background events are histogrammed and averaged over all cycles with same magnet polarity of a run. The mean energy can be written as:

$$E_C = \frac{1}{N_r} \sum_{i=1}^{N_r} (sb_i - b_i) \quad (5.3)$$

Where N_r is the total number of events in cycles with same magnet polarity for all runs of a given setting point.

Method D

Method D was developed to minimize the effect of fluctuations from event to event [A. Schällicke(2005), R. Dollan(2005)]. The energy deposition of every background event of a cycle is subtracted from each signal event and all combinations are filled into a histogram. The mean signal of the cycle is defined as the mean of this distribution:

$$E_D = \frac{1}{n_s n_b} \sum_{i=1}^{n_s} \sum_{j=1}^{n_b} (s_i - b_j) \quad (5.4)$$

The number n_s of signal events is similar to the number n_b of background events for all cycles. The fact that each event is multiply used is accounted for in the statistical treatment of the errors. The mean of a truncated distribution is a more stable measure of the average signal. There the mean energy is determined by a fit of the sum of two Gaussians (“double Gaussian”) to the peak region of the distribution within $\pm 2\sigma$. The whole procedure of the background subtraction and truncation has been checked by simulations. In particular the error determination has been scrutinized by repeating the experiment many times in the simulation. This method was proposed for the E-166 data analysis.

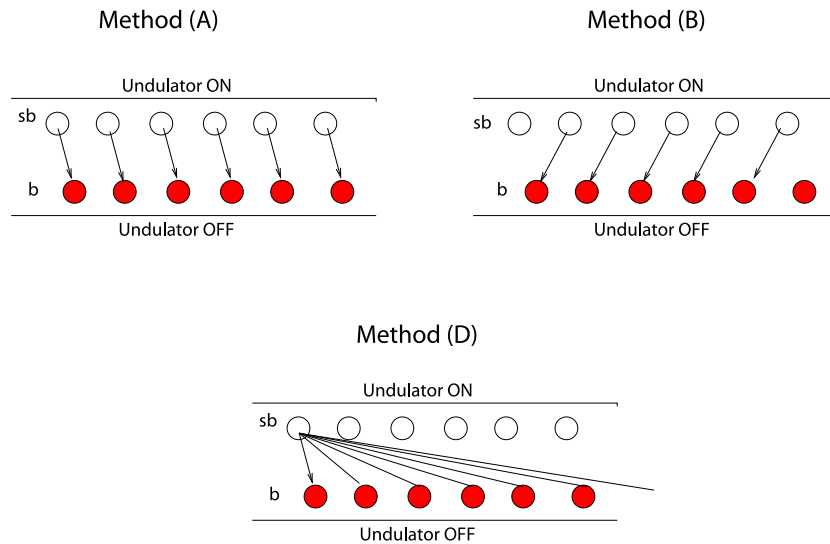


Figure 5.8: Scheme describing the background subtraction in the analysis methods A, B and, D.

5.2.4 Asymmetries

Asymmetries are derived from pairs of adjacent cycles with opposite magnet polarity. The mean energy deposition of the “positive” cycle E_i^+ is subtracted from the “negative” cycle E_i^- .

Only the mean energy deposition in the central crystal of the CsI(Tl) Calorimeter is used:

The asymmetry δ_i is defined by:

$$\delta_i = \frac{E_i^- - E_i^+}{E_i^- + E_i^+}, \quad (5.5)$$

with the statistical error.

$$\Delta\delta_i = \frac{2}{(E_i^- + E_i^+)^2} \cdot \sqrt{(E_i^+ \Delta E_i^-)^2 + (E_i^- \Delta E_i^+)^2}, \quad (5.6)$$

where the errors ΔE_i^- and ΔE_i^+ on the mean values are derived from the Gaussian fit.

5.3 Systematic Uncertainties

One of the most critical aspects in the polarization measurement are fake asymmetries introduced by systematic errors. A potential source is the fringe field of the analyzing magnet. This and other uncertainties are discussed below.

The data analysis of the E-166 experiment is not completed yet. Systematic errors are still under investigation. The current status is critically reported here.

5.3.1 Flux asymmetries and corrections

As discussed in section 5.2.2, any systematic change in the positron flux with the magnet polarity would introduce a fake asymmetry. The analyzing magnet’s fringe field extends and overlaps with the spectrometer field in the region close to the reversion target. This causes a change in the net field when the magnet polarity is reversed. Because of the asymmetric spatial distribution of positrons at the exit of the spectrometer’s vacuum chamber this may affect the positrons moving to the reversion target asymmetrically when the magnet polarity is reversed.

Indeed, the PosSi counter has recorded asymmetries in the positron (electron) flux which are correlated with the magnet polarity. These asymmetries

I_{spec} [A]	run mode	PosSi Asymmetry $\delta_{PosSi} \pm \Delta\delta_{PosSi}$
100	e ⁺	-0.00115 ± 0.00017
120	e ⁺	-0.00066 ± 0.00020
140	e ⁺ (1)	-0.00107 ± 0.00110
140	e ⁺ (2)	-0.00055 ± 0.00019
150	e ⁺	-0.00095 ± 0.00034
160	e ⁺	-0.00035 ± 0.00023
160	e ⁻	0.00382 ± 0.00022
180	e ⁺	-0.00108 ± 0.00063
180	e ⁺ (ff)	-0.00081 ± 0.00055

Table 5.2: Asymmetries recorded by the PosSi counter for different setting points [W. Bugg(2007)]. (1) and (2) stands for the first and second set of data taken at 140 A setting point. (ff) stands for the 160 A setting point where in the cooling system of the undulator the ferro fluid was used [A.Mikhailichenko(2004)].

are listed in table 5.2 [W. Bugg(2007)]. Hence, the measured asymmetries in the CsI(Tl) have to be corrected. The correction can be derived analytically from Eq. 5.5 and it is given by:

$$\delta_{pol} = \frac{\delta_m - \delta_{PosSi}}{1 - \delta_m \delta_{PosSi}} \quad (5.7)$$

δ_{pol} is the asymmetry due to polarization effects, δ_m is the measured asymmetry given by Eq. 5.5 and δ_{PosSi} the (fake) asymmetry measured by the PosSi counter:

$$\delta_{PosSi} = \frac{N_0^{(-)} - N_0^{(+)}}{N_0^{(-)} + N_0^{(+)}} \quad (5.8)$$

$N_0^{(+)}$ and $N_0^{(-)}$ are the positron (electron) fluxes for positive and negative magnet polarity, respectively.

5.3.2 Extrinsic Background

Background in E-166 can be a source of systematic errors and may affect the asymmetries. The sources of possible background seen by the CsI(Tl) can be sorted in two categories: extrinsic and intrinsic background sources. The extrinsic background is generated outside the positron table mainly by the

46.6 GeV electron beam and the intrinsic background is from the positron diagnostic table.

Bremsstrahlung photons from the undulator table: It is believed that the dominant background source are bremsstrahlung photons generated when a fraction of the electron beam scrapes the tungsten collimator at the entrance of the undulator. This was established by comparing the background level when the electron beam was sent through the bypass pipe and through the unpowered undulator. It was clear that a considerable background was recorded by several detectors including the CsI calorimeter only when the electron beam passed the undulator (collimator). If this background is stable over two consecutive events it is properly subtracted by the procedure discussed in section 5.2.3.

When pulsing the undulator, it turned out that the electron beam was systematically kicked by the undulator's magnetic field. A Beam Position Monitor (BPM) located far downstream of the undulator table recorded a double peak structure in X and in Y corresponding to two different beam positions correlated with undulator ON and OFF. This kick of the electron beam may occur either at the entrance of the undulator, at the exit or in both locations. If the electron beam is affected at the entrance region this may have consequences. The background is not stable and changes from the undulator OFF to undulator ON. Hence is not properly subtracted. However, it is believed that this kick is very small and the change in background can be neglected.

Bremsstrahlung photons from electron beam pipe: This type of background may be generated if electrons from the main beam scrape the beam pipe in a region close to the positron table. It was monitored by the CsI prototype crystal positioned on the positron table underneath the lead shielding. It recorded photons coming from the beam pipe below the table. When the electron beam was in the bypass mode no background was present.

Neutrons from the beam dump: When the electron beam is stopped in the dump, nuclear reactions might be induced, which create free neutrons. These are thermalized and might escape the dump over some time. In addition to lead shielding deployed around the CsI calorimeter, a layer of polyethylene bricks was constructed to shield the CsI from neutrons. It was checked by looking for delayed signals for the CsI(Tl) with an oscilloscope. No indication of neutron background was found.

5.3.3 Intrinsic Background

The intrinsic background is the soft background generated on the positron table. The source of this background can either be the conversion target itself and/or photons generated when electrons/positrons are stopped in the vacuum chamber. A proper shielding configuration for the CsI crystals was derived from a simulation study in [Pöschl(2004)]. As a result of this optimization no background from this source should reach the CsI.

An important and critical background that one can not shield against are the bremsstrahlung photons generated when positrons (electrons) are stopped in the vacuum pipe at the exit of the spectrometer's vacuum chamber. The simulation study shows that the ratio between the number of positrons reaching the reconversion target and the number of positrons stopped in the vacuum pipe is about $\frac{1}{8}$. A fraction of these background photons are in the acceptance of the CsI calorimeter and may have different polarization than those generated at the reconversion target. The simulation study of the positron polarimeter didn't take into account this background yet. Further investigations are needed to understand this background and its effect on the analyzing power and the polarization.

Effect of residual background for two adjacent events: As shown in section 5.2.4 the asymmetry calculation is based on the mean energy deposited in the CsI(Tl) crystals. The background subtraction methods discussed in section 5.2.3 can be applied only if identical background for undulator OFF and ON is assumed.

Now let's assume that the background in the undulator ON is higher than the background in the undulator OFF configuration. This scenario is not impossible since in the undulator ON configuration additional particles are created like undulator photons, positrons and electrons which may generate additional background in the CsI(Tl) crystals.

Consider a similar residual background ϵ_b for both magnet polarities. Then: $E_i'^- = E_i^- + \epsilon_b$ and $E_i'^+ = E_i^+ + \epsilon_b$

One can clearly see that in such a scenario the residual background will induce an underestimation of the calculated asymmetry,

$$\delta_i = \frac{E_i^- - E_i^+}{E_i^- + E_i^+ + 2\epsilon_b} \quad (5.9)$$

Change of background with magnet polarity: The fringe field of the analyzing magnet might affect the background reaching the CsI(Tl) calorimeter. If the background level is different for two adjacent cycles with opposite

magnet polarity, the asymmetry calculation can be considerably affected. In this situation even the sign of the asymmetries might change. This effect is believed to be small but more simulation work is necessary.

5.3.4 Knowledge of the iron polarization

The saturation of the iron core is believed to be non-uniform along the iron length. The maximum saturation may be present in the center. However at the surface the saturation may differ. This is an important information which is missing and a quantitative study has to be done to evaluate the homogeneity of the magnetization in the iron core.

5.4 Results

5.4.1 Asymmetries

The asymmetries extracted for all pairs of cycles and for different spectrometer settings using method A are shown in Fig. 5.9 and the values are listed in Table 5.3. The value for the asymmetry δ is determined by fitting a constant to all single asymmetries δ_i taking the errors into account. The scatter of the individual pairs of cycles is roughly consistent with pure statistical fluctuations. The obtained asymmetries are compared to the asymmetries from method C and D.

The results for all spectrometer settings are summarized in Table 5.3 and 5.4 and Fig. 5.10 and 5.11. All methods are consistent with each other.

A detailed analysis with method D [R. Dollan(2005)] has shown that the asymmetries for the central crystal (number 5) are most significant. The asymmetries are listed in Table 5.4. The asymmetries of all crystals are consistent with the expectations from simulation. The combination of the asymmetries of all crystals would give a slight improvement of the statistical significance.

5.4.2 Positron and electron polarization

With the analyzing power $A_{e^+}(E)$ which has been determined for different positron energies by simulation (see sect. 4.6.2) and the effective polarization of the core of the analyzing magnet $P_{e^-} = 0.069 \pm 0.0010$, the longitudinal polarization of the positrons is determined by:

$$P_{e^+} = \frac{\delta}{A_{e^+} P_{e^-}}. \quad (5.10)$$

I_S	E(e^\pm) [MeV]	Method A $\delta \pm \Delta\delta$	Method B $\delta \pm \Delta\delta$
100	4.59	0.0060 ± 0.0023	0.0048 ± 0.0024
120	5.36	0.0074 ± 0.0010	0.0090 ± 0.0011
140	6.07	0.0102 ± 0.0008	0.0087 ± 0.0009
160	6.72	0.0070 ± 0.0012	0.0098 ± 0.0013
160 (e^-)	6.72	0.0132 ± 0.0006	0.0143 ± 0.0006
180	7.35	0.0087 ± 0.0014	0.0087 ± 0.0015

Table 5.3: Measured asymmetries in the central crystal for different spectrometer settings using method A and B.

I_S	E(e^\pm) [MeV]	Method C $\delta \pm \Delta\delta$	Method D $\delta \pm \Delta\delta$
100	4.59	0.0044 ± 0.0016	0.00575 ± 0.00164
120	5.36	0.0085 ± 0.0017	0.00895 ± 0.00081
140	6.07	0.0082 ± 0.0012	0.01037 ± 0.00580
160	6.72	0.0121 ± 0.0019	0.00889 ± 0.00096
160 (e^-)	6.72	0.0147 ± 0.0020	0.01320 ± 0.00049
180	7.35	0.0101 ± 0.0019	0.00883 ± 0.00124

Table 5.4: Measured asymmetries in the central crystal for different spectrometer settings using method C and D.

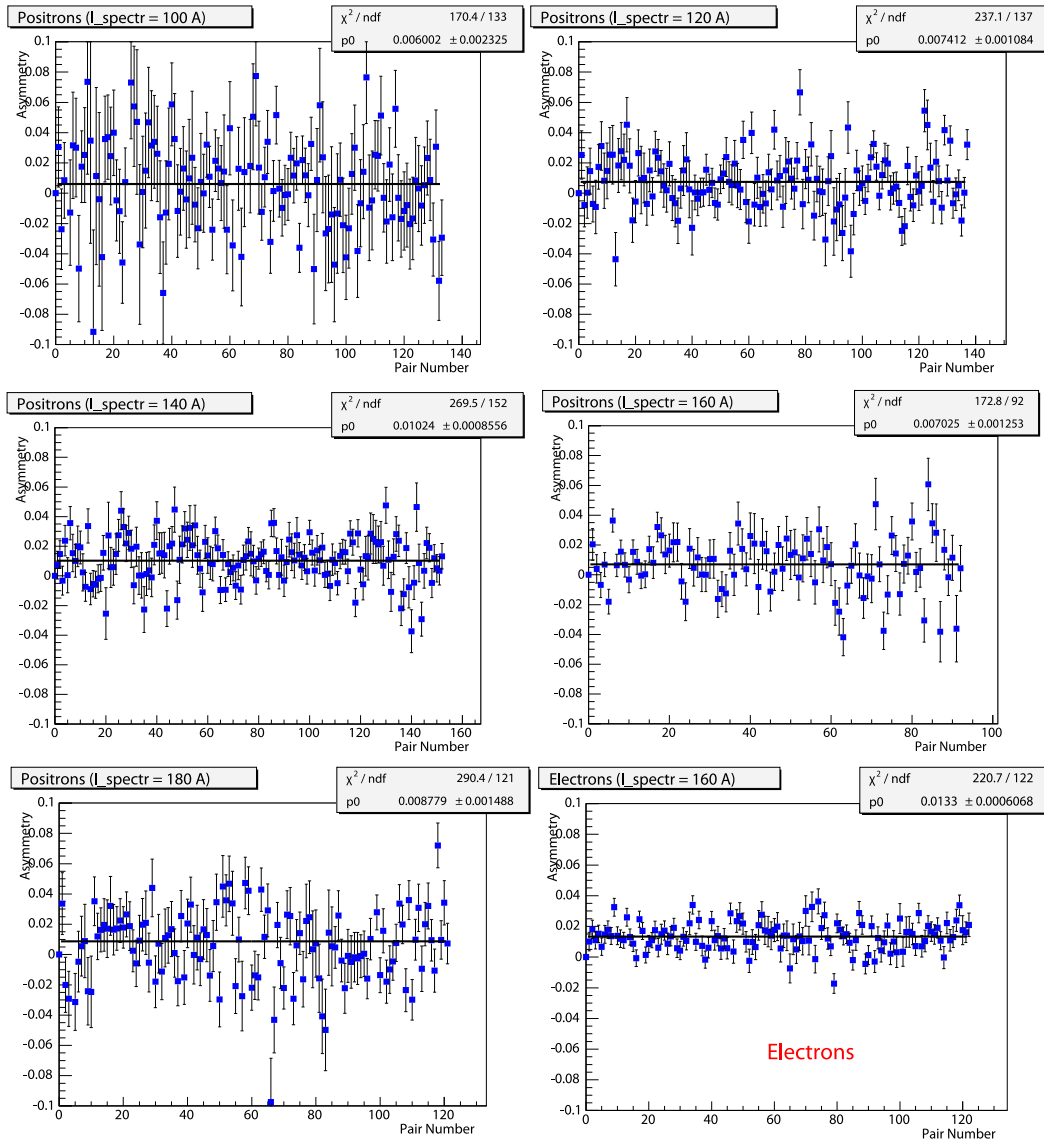


Figure 5.9: Positron (electron) asymmetries for pairs of cycles for the all setting points of the spectrometer.

The results are listed in table 5.5 for the central crystal. For each energy point the polarization measurements from each crystal are consistent with each other within the errors.

The measured polarizations as a function of the energy is compared to the simulation in Fig. 5.12 and Fig. 5.13. They demonstrate good agreement with the expectation.

The one measured point for electron polarization also agrees with ex-

E [MeV]	$P \pm \Delta P$ Method A	$P \pm \Delta P$ Method B
4.59	0.6916 ± 0.2414	0.5821 ± 0.2514
5.36	0.7483 ± 0.1192	0.9030 ± 0.1225
6.07	1.0134 ± 0.1755	0.8814 ± 0.1804
6.72	0.6472 ± 0.1302	0.8918 ± 0.1383
6.72 (e^-)	$0,9228 \pm 0,0507$	$0,8937 \pm 0,0491$
7.35	0.8472 ± 0.1821	0.8407 ± 0.1914

Table 5.5: Degree of longitudinal polarization derived from the measured asymmetries in the central crystal for different $e^+(e^-)$ energy using method A and B. The measured asymmetries are corrected for the flux asymmetries recorded by the posSi counter using Eq. 5.7.

Detector	Asymmetry	Error
Ag1SiC	0.03883	0.00062
Ag1	0.03307	0.00123
Gcal	0.03665	0.00071

Table 5.6: The measured asymmetry of the polarized undulator photon beam.

pectations and confirms that systematic effects which could be different for electrons and positrons are well under control. The experiment has succeeded to produce polarized positrons with the expected degree of polarization.

5.5 The Photon Asymmetry and Polarization

The circular polarization of the undulator photons was measured by a similar polarimeter as for positrons. The only difference was that the photon analyzing magnet had a 15 cm thick absorber and also no reversion target was needed. The asymmetry (see table 5.6) was derived using three detectors Ag1SiC, Ag1 and Gcal. The measured asymmetries are in a good agreement with the expectation.

GEANT3 simulations using polarized Compton scattering cross sections averaged over the calculated undulator energy and polarization distribution and convoluted with detector response functions yield to predicted asymmetries from 3.2% to 3.5% for the various detectors.

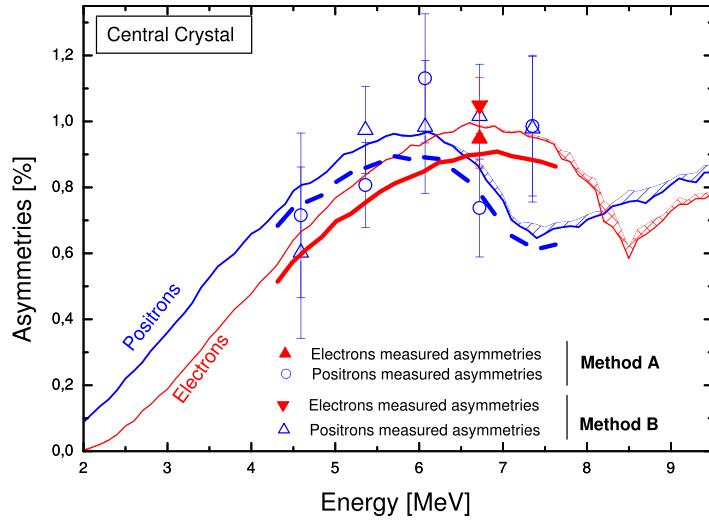


Figure 5.10: Measured asymmetries in the central crystal for different electron and positron energies (method A and B). The asymmetries are corrected for the PosSi asymmetries.

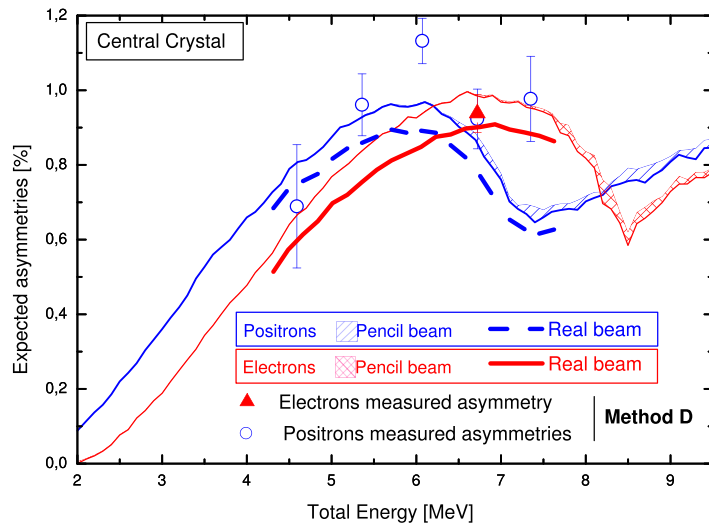


Figure 5.11: Measured asymmetries in the central crystal for different electron and positron energies (method D).

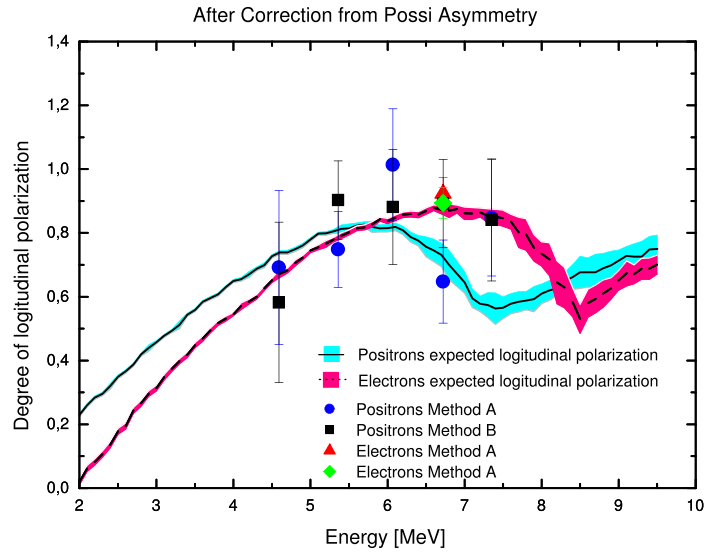


Figure 5.12: Degree of longitudinal polarization for positrons and electrons (method A and B). The polarization is derived from the corrected asymmetries from the PosSi asymmetries. They are compared to the expectations from simulations.

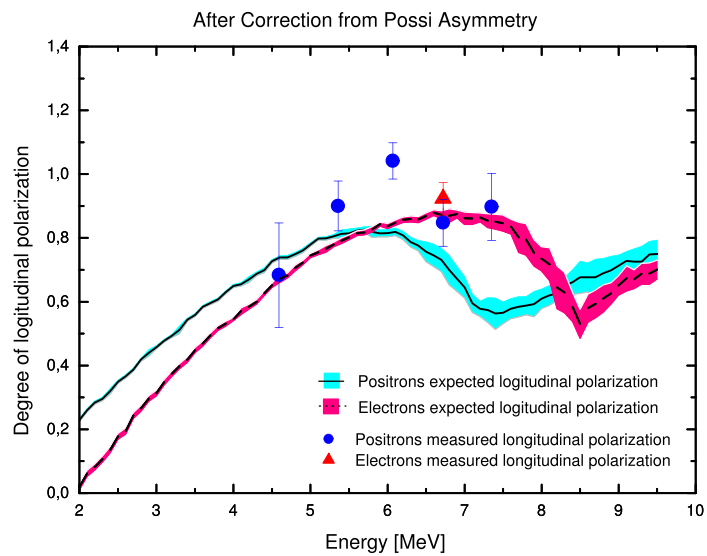


Figure 5.13: Degree of longitudinal polarization for positrons and electrons (method D).

Conclusion

Here the design of the E-166 experiment, the prototyping and construction, the execution of the experiment at the SLAC FFTB beam, and the analysis of the data are described.

The undulator functioned without any problems providing a polarized photon spectrum with an energy cutoff close to the one expected at the international linear collider. Polarized positrons were produced in a thin target and analyzed with respect to their momentum and polarization. The alignment of the different components of the positron diagnostic section turned out to be very critical. Some corrections on miss-alignment and false asymmetries had to be corrected.

But over all the positron yield at the conversion target and polarization agrees with the expected values on the 10 to 20 % level.

Over the period of the preparation and the runs of the experiment we gained valuable experience with the operation of a source of polarized positrons. This is maybe the most important aspect for the development of the ILC's positron source.

During the data analysis the need for a full simulation of the experiment diagnostics sections arose and all relevant polarization processes were implemented in the Geant4 code to the benefit of further experiments on polarized photons, positron, and electrons.

In summary, the positron polarization was measured at 6 different energy settings of the spectrometer. The highest polarization -about 80%- was measured for the 6 MeV positrons with a relative error of about 15%. In addition, an electron polarization measurement was carried out at a single energy setting by reversing the polarity of the spectrometer.

The method used in this experiment can be scaled up to provide polarized positron beams for the next generation of linear colliders. Moreover, the polarization extension to Geant4 provides now a basis for any optimization studies for the ILC positron source, and many polarimeter applications.

The E-166 the experiment was a full success and has demonstrated that the principle of the helical undulator based polarized positron source works.

Acknowledgement

I would like to express my deep gratitude to all those who gave me the possibility to start, to complete and to make this thesis possible.

My first and special gratitude goes to my wife Dalila, my son and daughter Ilyas and Yasmine for their patient love and their patience when sometimes being absorbed by this thesis I was maybe distant from them. Also, many thanks go to my parents encouraging and supporting my studies from the (Maternelle) primary school to the university.

I am deeply indebted and entirely grateful to my first supervisor Prof. Dr. Achim Stahl leader of the (LC) Linear Colider group in December 2003 at DESY-Zeuthen for hosting me in his group with a main task: working on the E-166 experiment. I will never forget his guidance in my first steps to the experiment, his patience, teachings, fruitful physics discussions and mainly his priceless support, encouragement and help in some difficult moments I had when completing this thesis.

I'm extremely thankful to my official supervisor at the Humboldt university Berlin, Prof. Dr. Hermann Kolanoski for his help to accomplish this work. His corrections, critics, discussions, suggestions and guidance during the formating and the writing period made this thesis possible.

I am extremely grateful to Dr. Andreas Schälike for his priceless assistance in pushing, encouraging and supervising the simulation part related to the polarization dependent of some EM processes in Geant4. Many thanks to the E-166 group at DESY-Zeuthen mainly Prof. Dr. Thomas Lohse for the fruitful physics discussions, Dr. Sabine Riemann and Ralph Dollan for the priceless support during my three years at DESY-Zeuthen.

Many thanks to Dr. Jürgen Schreiber and all my colleagues and friends at the DESY-LC group for their endless support providing a wonderful working atmosphere. I will never forget the wonderful and exiting moments at SLAC during the run period of the E-166 experiment. I want to express my gratitude towards the E-166 collaboration mainly towards Dr. John Sheppard and Prof. Dr. William (Bill) bugg in providong a wonderful support to this work summarized in this thesis.

Bibliography

- [A. A.Sokolov(1964)] I. M. Ternov A. A.Sokolov. On polarization and spin effects in synchrotron radiation theory. *Sov.Phys.Doklady*, 8:1203, 1964.
- [A. Schälicke(2006)] et al A. Schälicke. Study on low energy positron polarimetry. *Proceedings of EPAC06, WEPLS045*, 1:2475, 2006.
- [A. Schälicke(2005)] H. Kolanoski A. Schälicke, S. Riemann. June run data analysis of the positron asymmetry: E-166 internal note. Technical report, DEDY Zeuthen, 2005. URL [http://www.slac.stanford.edu/exp/e166/internal/doc/2005/2005-09-09-dreas-posi\\$_\\$june.pdf](http://www.slac.stanford.edu/exp/e166/internal/doc/2005/2005-09-09-dreas-posi$_$june.pdf).
- [A. Ushakov(2006)] et al A. Ushakov. Radiation levels and activation at the ilc positron source. *EPAC 06*, page 2478, 2006.
- [Alexander and Reinherz-Aronis(2005)] G. Alexander and E. Reinherz-Aronis. Positron asymmetry and polarisation extracted from the e166 september 2005 run. Technical report, Tel-aviv university, 2005. URL <http://www.slac.stanford.edu/exp/e166/internal/doc/2005/2005-12-19-alex-memo.pdf>.
- [A.Mikhailichenko(2004)] A.Mikhailichenko. Usage of ferrofluid for improvement parameters of micro-magnet. Technical report, Corenl university, 2004.
- [B. Ananthanarayan and Bartl(2004)] Ritesh K. Singh B. Ananthanarayan, Saurabh D. Rindani and A. Bartl. Transverse beam polarization and cp-violating triple gauge-boson couplings. *Phys. Lett. B*, 593:95–104, 2004.
- [Balakin and Mikhailichenko(1979)] V. E. Balakin and A. A. Mikhailichenko. The conversion system for obtaining high polarized electrons and positrons. *Nuclear Physics, Preprint BINP*, pages 79–85, 1979.

- [Bugg(2006)] W. Bugg. Spectrometer test experimentent (spectrometer calibration with beta source): E-166 internal note. Technical report, SLAC, 2006.
- [collaboration(2006a)] ILC collaboration. The ilc baseline configuration document (bcd). Technical report, ILC, 2006a. URL <http://www.linearcollider.org/cms/pid=1000104>.
- [collaboration(2006b)] ILC collaboration. The ilc beam parameters. Technical report, ILC, 2006b. URL <http://www-project.slac.stanford.edu/ilc/discussion/Default.htm>.
- [Depaola(2003)] G. Depaola. New monte carlo method for compton and rayleigh scattering by polarized gamma rays. *Nucl Inst Meth A*, 512, 2003.
- [Desch(1999)] K. Desch. Calculated rates with program pythia. Technical report, ECFA, 1999. URL <http://ireswww.in2p3.fr/ires/ecfadesy/>.
- [D.P. Barber(2002a)] G. Ripken D.P. Barber. *Handbook of Accelerator Physics and Engineering*. Eds. A.W. Chao, M. Tigner, World Scientific, 2 edition, 2002a.
- [D.P. Barber(2002b)] W. Decking D.P. Barber. Polarization preservation in the nlc and tesla damping rings. Technical report, DESY, 2002b.
- [F. W. Lipps(1954)] H. A. Tolhoek F. W. Lipps. Polarization phenomena of electrons and photons i and ii. *Physica*, 20:85 and 395, 1954.
- [Flöttmann(1993)] K. Flöttmann. *Investigations toward the development of polarized and unpolarized high intensity positron sources for linear colliders*. PhD thesis, DESY Hamburg, 1993. See also DESY-93-161.
- [Flöttmann(2005)] Klaus Flöttmann. Preparing the decision: Conventional versus undulator based positron source. Technical Report EUROTEV-Report-2005-015-1, DESY, 2005.
- [G. Alexander(2003)] et al. G. Alexander. Undulator-based production of polarized positrons: A proposal for the 50-gev beam in the fftb. *SLAC-TN-04-018*, 2003. SLAC-PROPOSAL-E-166.
- [G. Moortgat-Pick(2006)] et al G. Moortgat-Pick. The role of polarized positrons and electrons in revealing fundamental interactions at the linear collider. *hep-ph/0507011*, 2006.

- [G. W. Ford(1957)] C. J. Mullin G. W. Ford. Scattering of polarized dirac particles on electrons. *Phys. Rev*, 108:477, 1957.
- [GEANT4(2003)] Collaboration GEANT4. Geant4 simulation toolkit. *IEEE Transactions*, 506:250–303, 2003.
- [GEANT4(2006)] Collaboration GEANT4. Geant4 developments and applications, nuclear science. *IEEE Transactions*, 53:270–278, 2006.
- [GEANT4(2007)] Collaboration GEANT4. Geant4 physics reference manual. Technical report, CERN, 2007. URL <http://geant4.web.cern.ch/geant4/UserDocumentation/UsersGuides/PhysicsReferenceManual/html/index.html>.
- [Gunst and Page(1953)] S. B. Gunst and L. A. Page. Compton scattering of 2.62 mev gamma rays by polarized electrons. *Phys. Rev.*, 92:970–973, 1953.
- [H. Davies(1954)] L. C. Maximon. H. Davies, H. A. Bethe. Theory of bremsstrahlung and pair production. ii. integral cross section for pair production. *Phys. Rev.*, 93(4):788–795, 1954.
- [H. W. Koch(1959)] J. W. Motz. H. W. Koch. Bremsstrahlung cross-section formulas and related data. *Rev. Mod. Phys.*, 31(4):920–955, 1959.
- [Hoogduin(1997)] J. Hoogduin. *Electron, positron and photon polarimetry*. PhD thesis, Rijksuniversiteit Groningen, 1997.
- [I. M. Ternov(1982)] V. A. Bordovitsyn I. M. Ternov. Synchrotron radiation of a magnetic moment in classical electrodynamics. *Russian Physics Journal*, 25:83–87, 1982.
- [ICFA(2006)] ICFA. Parameters for the linear collider. Technical report, ILC, 2006. URL <http://www.interactions.org/linearcollider/documents/index.htm>.
- [J. P. Blewett(1977)] R. Chasman J. P. Blewett. Orbits and fields in the helical wiggler. *J. Appl. Phys.*, 48:2962, 1977.
- [J.D.Jackson(1982)] J.D.Jackson. *Klassische Elektrodynamik*. W. de Gruyter, 1982.
- [K. Yokoya(1988)] P. Chen K. Yokoya. Disruption effects from the interaction of round e+e- beams. *Phys. Rev. D*, 38, 1988.

- [Kincaid(1977)] B. M. Kincaid. A short-period helical wiggler as an important source of synchrotron radiation. *J. Appl. Phys.*, 48:2684, 1977.
- [Kovermann(2006)] J. W. Kovermann. *Die polarisierte Positronenquelle E166 Kalibration des Kalorimeters*. PhD thesis, RWTH Aachen university, 2006.
- [Laihem(2006a)] K. Laihem. The x-y distribution at the reconversion target: E-166 internal note. Technical report, DESY Zeuthen, 2006a. URL <http://www-zeuthen.desy.de/~klaihem/FieldMap/E166JawsImage.pdf>.
- [Laihem(2006b)] K. Laihem. Positron kinematics in e166 experiment: E-166 internal note. Technical report, DESY Zeuthen, 2006b. URL [http://www.slac.stanford.edu/exp/e166/internal/doc/2006/2006-02-28-kl-E166G4SIM\\$_\\$Part1/index.htm](http://www.slac.stanford.edu/exp/e166/internal/doc/2006/2006-02-28-kl-E166G4SIM$_$Part1/index.htm).
- [Laihem(2006c)] K. Laihem. Positron tracks visualization under mermaid field map:e-166 internal note. Technical report, DESY Zeuthen, 2006c. URL <http://www.slac.stanford.edu/exp/e166/internal/doc/2006/2006-06-20-kl-TrackWeb/>.
- [McMaster.(1954)] W. H. McMaster. Polarization and the stokes parameters. *American Journal of Physics*, 22(6):351–362, 1954.
- [McMaster.(1961)] W. H. McMaster. Matrix representation of polarization. *Rev. Mod. Phys.*, 33(1):8–29, 1961.
- [McMaster(1961)] W. H. McMaster. Matrix representation of polarization. *Rev. Mod. Phys.*, 33:8, 1961. G. Stokes, *Trans. Cambridge Phil. Soc.* 9 (1852) 399.
- [Mikhailichenko(2002)] A. A. Mikhailichenko. Pulsed helical undulator for test at slac. the polarized production scheme. Technical report, Cornell university, 2002. URL <http://www-project.slac.stanford.edu/lc/ilc/TechNotes/LCCNotes/PDF/LCC-0106>.
- [Mikhailichenko(2005)] A. A. Mikhailichenko. Mermaid field map for the e-166 spectrometer: E-166 internal note. Technical report, Cornell university, 2005.
- [Moortgat-Pick and Steiner(2001)] G. Moortgat-Pick and H. M. Steiner. Physics opportunities with polarized e- and e+ beams at tesla. *Eur.Phys.J.directC*, 3:6, 2001.

- [Olsen and Maximon(1959)] H. Olsen and L.C. Maximon. Photon and electron polarization in high-energy bremsstrahlung and pair production with screening. *Phys.Rev.*, 114:887, 1959.
- [P. Starovoitov(2007a)] et al P. Starovoitov. Polarized annihilation process in geant4 (in preparation). Technical report, DESY Zeuthen, 2007a.
- [P. Starovoitov(2007b)] et al P. Starovoitov. Polarized ionization process in geant4 (in preparation). Technical report, DESY Zeuthen, 2007b.
- [Page(1957)] L. A. Page. Polarization effects in the two-quantum annihilation of positrons. *Phys. Rev.*, 106:394–398, 1957.
- [Pöchel(2004)] R. Pöchel. Status of the spectrometer simulation:e-166 internal note. Technical report, DESY, 2004. URL [http://www.slac.stanford.edu/exp/e166/internal/doc/2004/2004-05-06-spectr\\$_\\$rp\\$_\\$070504.ps](http://www.slac.stanford.edu/exp/e166/internal/doc/2004/2004-05-06-spectr$_$rp$_$070504.ps).
- [Pöschl(2004)] R. Pöschl. Status report of the spectrometer simulation.(background studies): E-166 internal note. Technical report, DESY, 2004.
- [Pratt(1961)] R. H. Pratt. Transfer of helicity in radiation and absorption of high-energy photons. *Phys. Rev.*, 123, 1961.
- [P.Starovoitov(2007)] et al P.Starovoitov. Polarized compton scattering in geant4 (in preparation). Technical report, DESY Zeuthen, 2007.
- [R. Alley(1995)] et al R. Alley. The stanford linear accelerator polarized electron source. *SLAC-PUB-95-6489*, 1995.
- [R. Brun(1985)] et al R. Brun. The geant3 electromagnetic shower program and a comparison with the egs3 code. Technical report, CERN, 1985.
- [R. Dollan(2005)] et al R. Dollan. Analysis of positron asymmetries using september data. e-166 internal note. sep 2005. Technical report, DESY Zeuthen, 2005. URL [http://www.slac.stanford.edu/exp/e166/internal/doc/2006/2006-02-28-sr-e166\\$_\\$note.ps](http://www.slac.stanford.edu/exp/e166/internal/doc/2006/2006-02-28-sr-e166$_$note.ps).
- [R. Dollan and Schälicke(2006)] K. Laihem R. Dollan and A. Schälicke. Monte-carlo-based studies of polarized positron source for the ilc. *Nucl.Inst.Meth A*, 559:185–189, 2006.
- [R.W. Assmann(2001)] F. Zimmermann R.W. Assmann. Clic note 501. Technical report, CERN, 2001.

- [Schälicke(2006)] A. Schälicke. Implementation of polarization in geant4. Technical report, DESY Zeuthen, 2006. URL <http://www-zeuthen.desy.de/dreas/geant4/>.
- [Sheppard(2003)] J. Sheppard. Conventional positron target for a tesla formatted beam. Technical Report LCC-133, SLAC-TN-03-072, SLAC, 2003.
- [Stehle(1958)] P. Stehle. Calculation of electron-electron scattering. *Phys. Rev.*, 110:1458, 1958.
- [T. Omori(2006)] et al T. Omori. Efficient propagation of polarization from laser photons to positrons through compton scattering and electron-positron pair creation. *Phys. Rev. Lett*, 96:114801, 2006.
- [T. Omori(2003)] et al T. Omori. Design of a polarized positron source for linear colliders. *Nucl. Instrum. Methods Phys. Rev. A*, 500:232, 2003.
- [Thompson(2001)] K. A. Thompson. Spin depolarization due to beam-beam interaction in nlc. Technical report, SLAC, 2001.
- [V. Bargmann(1959)] V. L. Telegdi V. Bargmann, L. Michel. Precession of the polarization of particles moving in a homogeneous electromagnetic field. *Phys. Rev. Lett*, 2:435, 1959.
- [V. Gharibian(2003)] K. P. Shuler V. Gharibian. Hera transvers polarimeter absolute scale and error by rise-time calibration. *arXiv:hep-x 0310045v1*, DESY, 2003.
- [W. Bugg(2007)] R. Dollan W. Bugg. The flux asymmetry recorded by the possi counter: E-166 internal note. Technical report, SLAC, DESY, 2007.
- [W. R. Nelson(1985)] D. W. O. Rogers W. R. Nelson, H. Hirayama. The egs4 code system. Technical report, SLAC, 1985. URL <http://rcwww.kek.jp/research/egs/epub.html>.

List of Figures

1.1	Schematic of the International Linear Collider (ILC) machine	2
1.2	Schematic of the polarized electron source at the SLC.	4
1.3	Schematic of the conventional positron source	5
1.4	Scheme of the Laser based polarized positron source at KEK .	6
1.5	Schematic of the undulator (planar/helical) positron source. .	7
1.6	Scheme of the undulator based positron source at the ILC . .	7
1.7	Possible spin configurations in e^+e^- annihilation	12
1.8	Polarization configurations in s -channel diagrams	13
1.9	Polarization configurations in crossed channels	13
1.10	Single W production	14
1.11	Higgs production	15
1.12	Feynman graphs for WW production	16
1.13	Feynman graphs for single W production	16
1.14	Selectron production	17
2.1	Aerial view of SLAC and the FFTB	22
2.2	Synoptic scheme of the E166 experimental	24
2.3	Synoptic scheme of the undulator table	26
2.4	The E-166 helical undulator	26
2.5	Schematic of the multiple-target system	27
2.6	Multiple-target system at E166	27
2.7	Principle of the photon and positron polarimeter	30
2.8	Perspective view of the polarimeter	31
2.9	Top view of the positron transport system	32
2.10	Picture of the positron transport system	33
2.11	The measured spectrometer's transverse magnetic field	34
2.12	Scheme of the PosSi counter	35
2.13	Scheme of the readout electronic chain	38
2.14	Energy spectrum of ^{60}Co measured by the CsI(Tl) crystal . . .	39
2.15	Calibrated spectrum of the ^{241}Am source	39
2.16	Photoelectron yield PY for the nine CsI(Tl) crystals	40

2.17	Back view of a single CsI(Tl) crystal	41
2.18	The CsI(Tl) calorimeter for E166	43
2.19	Front and back view of the CsI(Tl) calorimeter	44
2.20	Perspective view of the CsI(Tl) calorimeter	45
2.21	Cosmic spectra recorded in the CsI(Tl) calorimeter	46
2.22	Cosmic muons spectrum recorded in crystal 7	47
2.23	^{228}Th source spectrum recorded in crystal number 8.	47
2.24	Scheme and components on the gamma table	48
2.25	Picture of the aero-gel counters	49
2.26	Position of the background detectors	49
2.27	Photon signal and the electron beam steering	50
2.28	Recorded undulator photon signal in AG1SiC and AG2SiC	50
2.29	Recorded positron signal in the CsI(Tl) calorimeter	51
3.1	Trajectory drawn by the electric field vector in the X-Y plan.	55
3.2	Diagrams of gamma conversion and bremsstrahlung processes	62
3.3	Bremsstrahlung energy distribution and circular polarization	66
3.4	Positron longitudinal polarization after Bremsstrahlung	67
3.5	$e^+(e^-)$ longitudinal polarization in gamma conversion	69
3.6	Polarization transfer to δ -electrons in the Møller scattering	74
3.7	Polarization transfer to δ -electrons in the Bhabha scattering	75
3.8	Depolarization effect in the Bhabha scattering	76
3.9	Polarization transfer in the annihilation process	77
3.10	Polarization transfer in Compton scattering (photons)	79
3.11	Polarization transfer in Compton scattering (electrons)	79
4.1	Undulator photon spectrum for the first three harmonics	85
4.2	Electron and positron energy distribution at the target	88
4.3	Electron energy distribution from different processes	89
4.4	Contributions of different processes to the electron production	89
4.5	Positron and electron expected longitudinal polarization	90
4.6	Measured solenoid magnetic field for different x position	93
4.7	Positron transport at the spectrometer	94
4.8	Target-Lens-spectrometer system	95
4.9	Spectrometer field map comparison	97
4.10	Spectrometer field map (MERMAID) for $y=0$	97
4.11	Scheme of one segment for the 3D interpolation	98
4.12	Schematic of the E-166 transport system	99
4.13	Yield at the PosSi counter vs. solenoid current	101
4.14	The e^+ yield at the PosSi counter vs. spectrometer current	102
4.15	Positron energy distribution at the PosSi and reconversion target	104

4.16	Positron energy at the reconversion target.	105
4.17	Spectrometer energy calibration	105
4.18	The positron spatial distributions	107
4.19	The positron X and Y distributions	108
4.20	Side view of the E166 positron polarimeter	109
4.21	The positron signal in the CsI(Tl) calorimeter (simulation) . .	112
4.22	Positron and electron analyzing powers (pencil beam)	113
4.23	Analyzing power for positrons: Ideal and realistic beam	114
4.24	Positron and electron analyzing power in the realistic beam . .	115
4.25	The expected e^+e^- analyzing power	118
4.26	Predicted asymmetries for positron and electrons	119
5.1	Data structure of a super-runs	122
5.2	Direction of magnetization of the iron core	123
5.3	The toroid signal recorded in ten cycles of a super-run.	125
5.4	Example of a good background conditions	127
5.5	Example of unstable background conditions	128
5.6	Background and positron signal events recorded in the CsI(Tl)	129
5.7	Background subtracted positron signal distribution	131
5.8	Scheme describing the background subtraction	132
5.9	Positron (electron) asymmetries for pairs of cycles	139
5.10	Measured asymmetries in the central crystal method A and B	141
5.11	Measured asymmetries in the central crystal method D	141
5.12	Degree of longitudinal polarization (method A and B)	142
5.13	Degree of longitudinal polarization (method D)	142

List of Tables

1.1	ILC beam parameters at the IP	3
1.2	Undulator-based positron system parameters	8
1.3	SM Higgs production scaling factors	15
1.4	Scaling factors for WW and ZZ production	16
2.1	The electron beam parameter for the E-166 experiment	25
2.2	Material and thickness of the multiple-target system	28
2.3	Position momentum as a function of the spectrometer current	34
2.4	Recorded Signal (counts) in the PosSi counter	35
2.5	Most relevant parameters of the CsI(Tl) crystals	42
2.6	Calibration constants for the CsI(tl) calorimeter	42
2.7	Statistics on the E-166 data	51
3.1	Class name of the polarized processes in GEANT4	61
3.2	Stokes parameters for photons, electrons and positrons	61
3.3	$\mathcal{F}(\hat{\xi}/\delta)$ for intermediate values of the screening factor [H. W. Koch(1959)]	64
4.1	Undulator radiation parameters in E-166	86
4.2	Contribution of the first, second and third harmonic	86
4.3	Positron and electron yield for $K=0.19$ and $E_e = 46.6$ GeV	87
4.4	Different contributions to the electron production for $K=0.19$	88
4.5	Target and beam parameters used for the simulation	91
4.6	Expected e^+ yield at the PosSi counter	103
4.7	Position momentum as a function of the spectrometer current	103
4.8	Particle and beam parameters used in the simulation	110
4.9	The analyzing power in the central crystal	111
4.10	The analyzing power in the central crystal for different setting points	111
4.11	The analyzing power for the positron signal in the calorimeter	116
4.12	The analyzing power for the electron signal in the calorimeter	117

5.1	Event samples used for the different spectrometer settings . . .	126
5.2	Asymmetries recorded by the PosSi counter for different setting points	134
5.3	Measured asymmetries in the central crystal (method A and B)	138
5.4	Measured asymmetries in the central crystal (method C and D)	138
5.5	Degree of longitudinal polarization	140
5.6	The measured asymmetry of the polarized undulator photon beam	140

Selbständigkeitserklärung

Hiermit erkläre ich, die Dissertation selbständig und ohne unerlaubte Hilfe angefertigt zu haben. Ich habe mich anderwärts nicht um einen Doktorgrad beworben und besitze einen entsprechenden Doktorgrad nicht. Ich erkläre die Kenntnisnahme der dem Verfahren zugrunde liegenden Promotionsordnung der Mathematisch-Naturwissenschaftlichen Fakultät I der Humboldt-Universität zu Berlin.

Karim Laihem